Giant Spin Hall Effect and Anomalous Hall Effect in Solids with Strong Spin-Orbit Coupling

by

Qiang Hao

B.S., University of Science and Technology of China, 2009

A Dissertation submitted in partial fulfillment of the

requirements for the degree of Doctor of Philosophy

in the Department of Physics at Brown University

Providence, Rhode Island

May 2016

This Dissertation by Qiang Hao is accepted in its present form by

the Department of Physics as satisfying the dissertation requirement for

the Degree of Doctor of Philosophy

Date……. ……
Professor Gang Xiao, Advisor

Recommended to the Graduate Council

Date……. ……
Professor Vesna Mitrovic, Reader

Date……. ……
Professor Antal Jevicki, Reader

Approved by the Graduate Council

Date……. ……
Peter Weber, Dean of the Graduate School

The Vita of Qiang Hao

Qiang Hao was born on February 7, 1987 in Qinhuangdao, China. He received his B.S. in Physics from University of Science and Technology of China in Hefei, China in 2009. The research for this thesis started in November 2010. His scientific publications include:

Publications:

1. Qiang Hao and Gang Xiao "Giant spin Hall effect and switching induced by spin-transfer-torque in a W/$Co_{40}Fe_{40}B_{20}$/MgO structure with perpendicular magnetic anisotropy", *Physical Review Applied*, **3**, 034009 (2015)

2. Qiang Hao, Wenzhe Chen, and Gang Xiao "β-tungsten thin films: structure, electron transport, and giant spin Hall effect", *Applied Physics Letters* **106**, 182403 (2015).

3. Qiang Hao and Gang Xiao "Giant spin Hall effect and magnetotransport in a Ta/ $Co_{40}Fe_{40}B_{20}$/MgO layered structure: a temperature dependence study", submitted to *Physical Review B* (2015).

4. Yuanjun Yang, Z. L. Luo, Meng Meng Yang, Haoliang Huang, Haibo Wang, J. Bao, Guoqiang Pan, C. Gao, Qiang Hao, Shutong Wang, Michael Jokubaitis, Wenzhe Zhang, Gang Xiao, Yiping Yao, Yukuai Liu, and X. G. Li "Piezo-strain induced non-volatile resistance states in (011)-$La_{2/3}Sr_{1/3}MnO_3$/0.7$Pb(Mg_{2/3}Nb_{1/3})O_3$-0.3$PbTiO_3$ epitaxial heterostructures", *Applied Physics Letters*, **102**, 033501 (2013).

5. Wenzhe Zhang, Qiang Hao, and Gang Xiao "Low-frequency noise in serial arrays of MgO-based magnetic tunnel junctions", *Physical Review B* **84**, 094446, (2011).

6. Xiao-Pu Han, Qiang Hao, Bing-Hong Wang, and Tao Zhou "Origin of the scaling law in human mobility: hierarchy of traffic systems", Physical Review E **83**, 036117, (2011).

7. Qiang Hao, Shutong Wang, and Gang Xiao "Anomalous Hall effect in Fe/Pt alloys", *Physical Review B*. (in preparation, to be submitted in May, 2015).

8. Qiang Hao, Shutong Wang, Wenzhe Chen, and Gang Xiao "Low frequency noise in Fe/Pt magnetic sensors based on Anomalous Hall effect", *Applied Physics Letters* (in preparation, to be submitted in May 2015).

Presentations:

1. Qiang Hao and Gang Xiao "Giant spin Hall effect in perpendicularly magnetized Ta/CoFeB/MgO structure and temperature dependence", *March Meeting of the American Physical Society*, March 2-6, 2015, San Antonio, Texas.

2. Qiang Hao, Shutong Wang, and Gang Xiao "Giant spin Hall effect in β-Ta and IrMn", *Nanoelectronics Research Initiative (NRI) and The Institute for Nanoelectronics Discovery and Exploration (INDEX) Annual Onsite Review*, Poster Session, August 5-6, 2014, College of Nanoscale Science and Engineering, Albany, NY.

Awards:

1. 2nd Place of 2014 INDEX Review Poster Award.

2. Outstanding Undergraduate Research Project from University of Science and Technology of China (2009).

Acknowledgements

First of all, I wish to thank my advisor, Professor Gang Xiao who has been extremely helpful during the past six years in my research and life at Brown University. He always stimulates me to strive to become a leader in my research effort and in my future career. I have been very fortunate to work with him on various spintronics projects and make our impacts to this field. I also wish to thank Professor Vesna Mitrovic and Professor Antal Jevicki, for reading this thesis and offering their valuable insight.

Next, I would like to thank the colleagues in my group, Xiaojing Zou, Wenzhe Zhang, and Shutong Wang for their assistance and advices in the lab. Specially, I would like to thank Dr. Wenzhe Zhang for guiding me through the experimental instrument setup and data analysis in the beginning years of my research.

Also, I would like to thank Michael Jibitsky, manager of the Micro-electronics facilities for help in using lithography and other processing equipment in the clean room. I appreciate Kenneth Silva for his support and help when I was the teaching assistant for fundamental Physics experiments.

I would like to thank my fellow students at Brown, Dongfang Li, Xi Yang, Guang Yang, Cong Cao, Yuzhen Guan, Sirui Tan, Wanchun Wei, Hao Tu, Yiming Yang and the rest of the Brown "Dragon" soccer team who have made my journey at Brown much more enjoyable.

Last but not least, my parents have always been wonderfully supportive and loving. My wife, Na Wei, has always been there for me, providing her love, support, understanding and inspiration for me. I thank them and dedicate this thesis to them.

To Mom, Dad and Na

Contents

List of Figures

Chapter 1

Motivation and Outline

1.1 Motivation

Spintronics is one of the emerging research fields that has been growing rapidly and showing great potentials in applications of novel magnetic sensors, memories and spin logic devices, which possess outperforming features including ultrafast response, low-power-consumption, non-volatility, superior low-noise performance and etc. Since 1988 when the giant magnetoresistance (GMR) was discovered, spintronics has not only exhibited rich new physics, but has been widely used in hard drives, storage media and etc. for the past two decades. The following discovery of tunneling magnetoresistance (TMR) made Magnetic Tunnel Junction (MTJ) presently the leading and most mature candidates for applications in the next-generation read heads and high density magnetic random access memories (MRAMs).

However, traditional MTJ-based memory unit requires switching the external magnetic field during the read/write procedure. An applied magnetic field is normally introduced by a current through a coil, which consumes considerably more power than the ideal scenario where a memory bit can be switched directly by a charge current or voltage using spin-transfer-torque or voltage-controlled-magnetic-anisotropy mechanism. Studies have been developed by many groups, including the most Giant Spin Hall Effect (GSHE) in a β-Ta thin film [1] which was introduced by the Cornell group in 2012 (Fig. 1.1). In this structure, an applied charge current in the GSHE solid (Ta layer) will exert a

spin-transfer-torque to the adjacent ferromagnetic layer (FM), and introduce a current-induced magnetization switching (procedure of writing information) in the presence of constant magnetic field. A low critical switching current will consume much less power than conventional memory devices. High-Z [2] and highly resistive transition metals [3-6] have been demonstrated to have great potential to be the promising candidate as the GSHE solids, such as β-Ta, β-W, Pt and related alloys. These solids are perfect examples of large spin-orbit coupling systems that could be used to study Giant Spin Hall Effect and be integrated in a layered structure as a foundation for low-power consumption memory devices. For instance, it has been shown that the critical current density that introduces magnetization switching is as low as 10^6 A/cm^2 in β-W/$Co_{40}Fe_{40}B_{20}$/MgO structure with perpendicular magnetic anisotropy (PMA) [6]. It is also advantageous for such structure because it does not require charge current flow directly through the junction layer like the traditional MTJ does and hence prevents the junction being "killed" by large current.

In general, MTJ-based magnetic sensors may require large output signal in terms of sensitivity, but it is the signal-to-noise ratio (SNR) that should be the measure for sensing performance. Diminishing the noise is equally important as enhancing the TMR signal outputs. For MTJ devices that operate at high frequencies, the white noise with a frequency-independent power distribution dominates. At low frequency region, the presence of significant 1/f noise limits the reliable and ultra-sensitive magnetometry applications. Since this noise is mostly caused by the tunneling mechanism, an alternative solution will be the anomalous Hall effect (AHE) sensor based on ferromagnetic metallic thin films. The strong spin-orbit coupling leading to large AHE gives rise to a high

sensitivity while the metallic nature of the sensor significantly reduce the while noise and 1/f noise. A systematic study in the AHE in a strong spin-orbit coupling system will introduce more insights in seeking for ideal candidates in the application of magnetic field sensing.

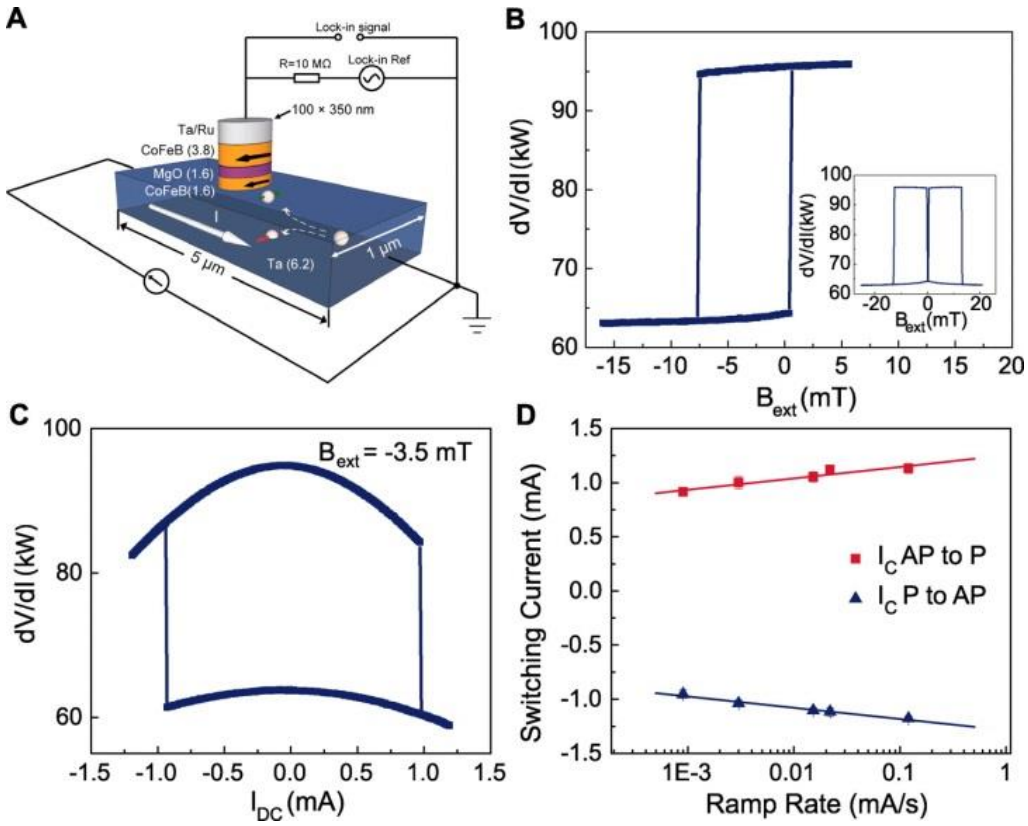

Fig. 1.1 Magnetic Tunnel Junction switched by applied charge current in giant spin Hall effect solid.

1.2 Outline

This thesis is divided into four parts. The first part (chapters 2-3) presents the experimental techniques and facilities as well as the theoretical background used for the fabrication and characterization of MgO-based MTJ and spin/anomalous Hall effect devices. The second part (chapter 4-6) focuses on the giant spin Hall effect (GSHE) and

techniques that we developed to achieve high quality multilayer sample as well as the methodology for characterizing the effect. We pay special attention to the beta-tungsten thin film, which exhibits outstanding properties and potentials as a GSHE solid. In the third part (chapter 7-8), we investigate the anomalous Hall effect and low-frequency noise performance in Fe-Pt alloy, another high-spin-orbit-coupling system. Finally, in chapter 9, we look into the characterization of MTJ devices and introduce the magneto-transport measurements that we developed. An emphasis is placed on the all-round characterization methods and a series of magneto-transfer curves. Details are enumerated below:

Chapter 2 describes the fabrication techniques of making MgO-based MTJ and Hall bar sample, including substrate oxidation, magnetron sputtering deposition, photo-lithography, ion beam etching, magnetic thermal annealing and etc. We emphasize on the experimental techniques to achieve beta-Ta and beta-W. Finally, we include the well-developed Quantum Design PPMS and low-frequency noise measurement system for various measurements.

In Chapter 3, we introduce the theoretical background which is useful for understanding and characterizing the GSHE, AHE and MTJ. The macrospin model is a simple model derived from the Landau-Lifshitz-Gilbert equation, and is helpful in characterizing spin-transfer-torque and spin Hall angle.

Chapter 4 focuses on the fabrication of beta-W thin films based on magnetron sputtering process. We analyze the structure and grain size of W thin films using x-ray diffraction. Also, electron transport in terms of resistivity and normal Hall effect is studied over a broad temperature range of 10 K to 300 K on all samples. These basic

properties reveal useful behaviors in the β-W thin films, and make them technologically promising for future spintronic magnetic random access memories (MRAMs) and spin-logic devices.

In Chapter 5, we have obtained robust perpendicular magnetic anisotropy in β-W/CoFeB/MgO structure without the need of any insertion layer between W and CoFeB. This was achieved within a broad range of W thickness (3.0-9.0 nm) using a simple fabrication technique. We have determined the spin Hall angle (-0.40 in the bulk limit) and spin diffusion length (3.5 nm) for β-W with a large spin-orbit coupling at room temperature. The elemental β-W is a superior candidate for magnetic memory and spin-logic applications.

Chapter 6 further studies the electron transport, magnetotransport and magnetic properties of β-Ta/CoFeB/MgO structure over a wide temperature range of 5K to 300K. β-Ta exhibits a large spin Hall angle of -0.14 and shows evidence of scaling with resistivity quadratically. This system is optimized and displays the lowest switching current density among similar systems and this comprehensive study may benefit applications of GSHE in spintronics.

In Chapter 7, we conduct a systematic study on the properties and the AHE in Fe-Pt alloy with various concentrations and thicknesses. By examining the temperature dependence on the longitudinal resistivity and Hall resistivity, we find out the intrinsic mechanism and side-jump mechanism may both contribute to the AHE effect.

Chapter 8 focuses on both the sensing capability and the noise performance of our fabricated Fe-Pt thin films. This AHE sensor indicates large Hall slope (16.6 $\mu\Omega \cdot cm/T$ at room temperature) and better low-frequency-noise performance than some

semiconductor Hall sensors. The results imply an ultrathin Fe-Pt alloy based Hall sensor could be a superior candidate for magnetic field sensing application.

In Chapter 9, a series of novel magneto-transport measurements are developed to determine a plethora of the magnetic parameters of spintronic devices by manipulating external magnetic fields. Different magneto-transfer curves measured on MgO-based MTJs are presented and analyzed to extract various magnetic parameters. Theoretical simulations based on the Stoner-Wohlfarth model are exhibited to elucidate the magnetoresistive transfer curve behaviors.

References

1. R. Coehoorn, J. C. S. Kools, T. G. S. M. Rijks, and K. M. H. Lenssen, Philips J. Res. 51, 93 (1998)
2. H. L. Wang, C. H. Du, Y. Pu, R. Adur, P. C. Hammel, and F. Y. Yang, Phys. Rev. Lett. **112**, 197201 (2014)
3. L. Liu, O. J. Lee, T. J. Gudmundsen, D. C. Ralph, and R. A. Buhrman, Phys. Rev. Lett. **109**, 096602 (2012)
4. C.-F. Pai, L. Liu, Y. Li, H. W. Tseng, D. C. Ralph, and R. A. Buhrman, Appl. Phys. Lett. **101**, 122404 (2012)
5. C.-F. Pai, M.-H. Nguyen, C. Belvin, L. H. Vilela-Leão, D. C. Ralph, and R. A. Buhrman, Appl. Phys. Lett. **104**, 082407 (2014)
6. Q. Hao and G. Xiao, Phys. Rev. Appl. **3**, 034009 (2015)

Chapter 2

Experimental Methods

2.1 Introduction

The principle experimental methods and techniques used during the fabrication of Magnetic Tunnel Junctions (MTJs) and Hall bar devices are introduced in this chapter, roughly in the order of the processing sequence, including substrate preparation, multilayer deposition, photolithography patterning, ion beam etching, SiO_2 layer deposition, gold layer deposition, and magnetic thermal annealing process. Then, we introduce the measurement electrodes setup as well as a short-loop process developed that enables quick measurements of magnetoresistance (MR) ratios of MTJ wafers. Besides, we discussed some unique fabrication processes, including beta-phase thin-film deposition and making composite target. Measurement systems, such as the Physical Property Measurement System (PPMS) and the low-frequency noise measurement are also introduced.

2.2 MTJ/Hall bar fabrication-involved experimental methods

2.2.1 Standard Hall Bar fabrication process

The fabrication process for Hall bar (Fig. 2.1) is a shorter version of MTJ fabrication. The two key procedures are etching down to the substrate layer to define Hall bar and deposit gold contact using lift-off procedure. The optimal (adhesive for wire bond) gold contact

has been experimentally determined to be (40 nm)Cr/(10 nm)Au with deposition power of gold (30 w) being twice larger than that of Cr (15w) using magnetron sputtering

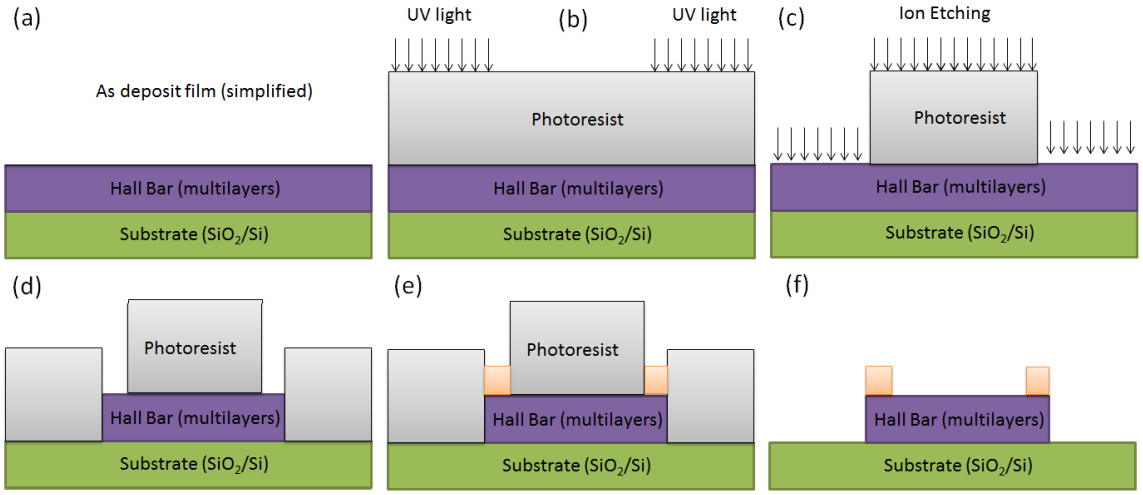

Fig. 2.1 Schematic diagrams of the Hall bar fabrication process: (a) As-deposited simplified film; (b-d) bottom contact layer defined after 1st patterning and etching steps; (e) gold contact deposited after 2nd patterning; (f) Hall bar with gold contact after lift-off procedure.

deposition. Gold contact is not critical for experimental results but important for successful wire bonding procedure.

Simplified procedure includes: a) oxidize silicon wafers to grow 2-μm-thick SiO_2 layer; b) deposit Hall sample multilayers using magnetron sputtering system; c) 1st photolithography patterning and ion milling etch define Hall bar shape; d) 2nd photolithography patterning, gold contact deposition and lift-off procedure define the Hall bar contact; e) magnetic thermal annealing (perpendicular to sample plane) is conducted to achieve perpendicular magnetic anisotropy (PMA) in the giant spin Hall effect samples.

2.2.2 Standard MTJ fabrication process

The standard semiconductor fabrication process is used to make MgO-based magnetic tunnel junctions. The complete sequence of steps is described as following, and illustrated in Figure 2.2. Here, MTJ multilayer stack is simplified, which contains only the free layer, the tunnel barrier and the pinned layer.

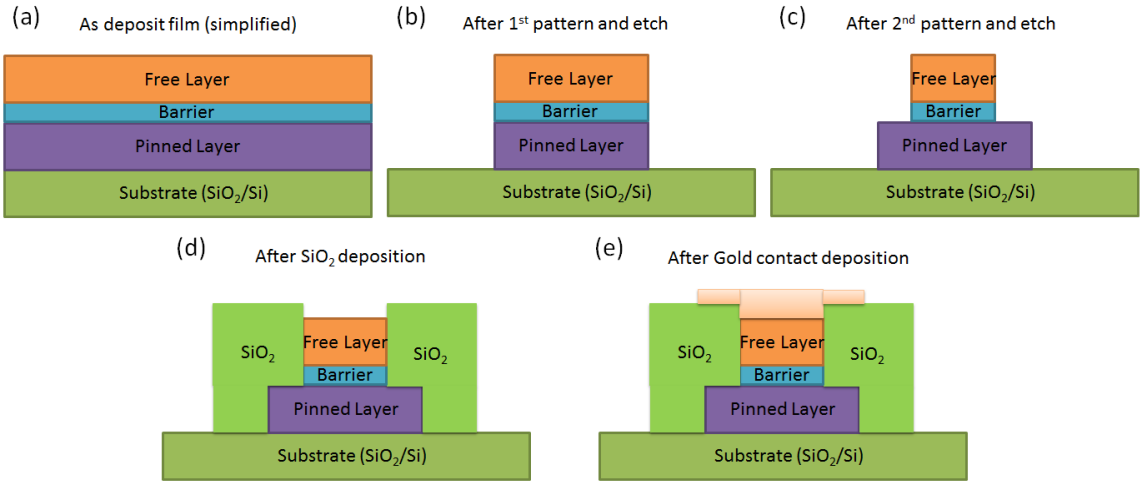

Figure 2.2 Schematic diagrams of the MTJ fabrication process: (a) as-deposited simplified film; (b) structure after the 1st patterning and 1st etching step; (c) after the 2nd patterning and 2nd etching process; (d) SiO_2 layer is deposited for isolation; (e) gold contact is deposited for probing top lead.

The complete process includes: a) oxidize silicon wafers to grow 2-μm-thick SiO_2 layer; b) magnetron sputtering deposition of MTJ multilayer stacks; c) 1st photolithography patterning and ion beam etching to define the bottom contact layer; d) 2nd photolithography patterning and ion beam etching to define the tunnel junction layer; e) SiO_2 layer deposition after 2nd ion beam etching to insulate the top and bottom electrodes; f) 3rd photolithography patterning and Cr/Au deposition to define the contact pads; g) thermal magnetic annealing procedure to define the pinning direction.

2.2.3 Oxygen Furnace

Our substrates are 2-inch diameter, <100>-oriented prime silicon wafers purchased from Silicon Quest International, Inc. (SQI). These wafers are polished on one side and have a thickness of 0.29 mm. The wafers are first treated with standard cleaning

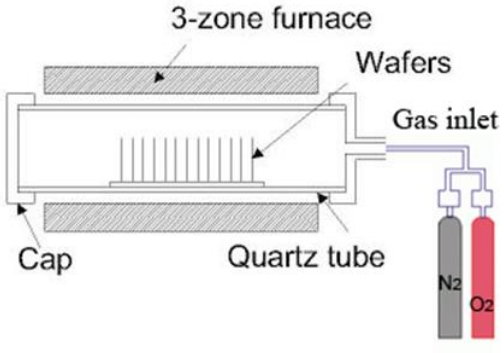

Fig. 2.3 Schematic drawing of a high-temperature oxidation furnace system

process to remove organic residues, and then loaded into a high-temperature oxidation furnace for the growth of SiO_2 insulating layers. In an oxygen-rich atmosphere, the growth rate for silicon dioxide is about 18 Å/min or 2.6 μm/24 hours at 1100 ºC. The schematic drawing of an oxidation furnace is illustrated in Figure 2.3, and the process sequence is described below:

a. Fully open the dry Oxygen purge knob (using Nitrogen).

b. Set dry Oxygen flow rate to 0.2 (reading).

c. Set temperature using the Temp Controller from 500 ºC to 1200 ºC (for three zones and the actual reading will be typically 1150 ºC).

d. Insert the sample wafers into the middle zone of the furnace after the temperature reaches 1150 ºC.

e. Turn off the dry Oxygen purge by closing knob in the first step.

f. Set channel 2 parameters as M = 0.51 pm and A = actual reading; push the button on Channel 2.

g. After overnight, turn off Oxygen, reduce the temperature to 500 ºC and open the dry Oxygen purge knob before removing the substrates out of the furnace.

2.2.4 Magnetron Sputtering: New Sputtering System (B)

Magnetron sputtering is a physical vapor deposition (PVD) process, which is widely used in industry-level production of high quality films. This technique has been used for depositing metals, alloys and oxides. The system requires high vacuum 10^{-7}~10^{-8} Torr as base pressure in order to achieve minimized defects in deposited materials. During operation, an inert gas, like Argon, is introduced to the chamber, (or both Argon and Oxygen when depositing oxides), and the magnetron target is negatively bias (DC) so that the electric field between the target and substrate ionizes the Argon molecule within the area. Positive ions bombard the target and sputter the target atoms onto the substrates, while negative electrons are trapped in small loops due to their smaller mass. A typical sputtering pressure is 4 mTorr, and the sputtering rate is about 0.1 nm/s. When depositing beta-Ta or beta-W, the growth rate might be even lower. Besides, an 8 minute pre-sputtering procedure is typically needed before deposition to clean up target surface and stabilize the deposition rate.

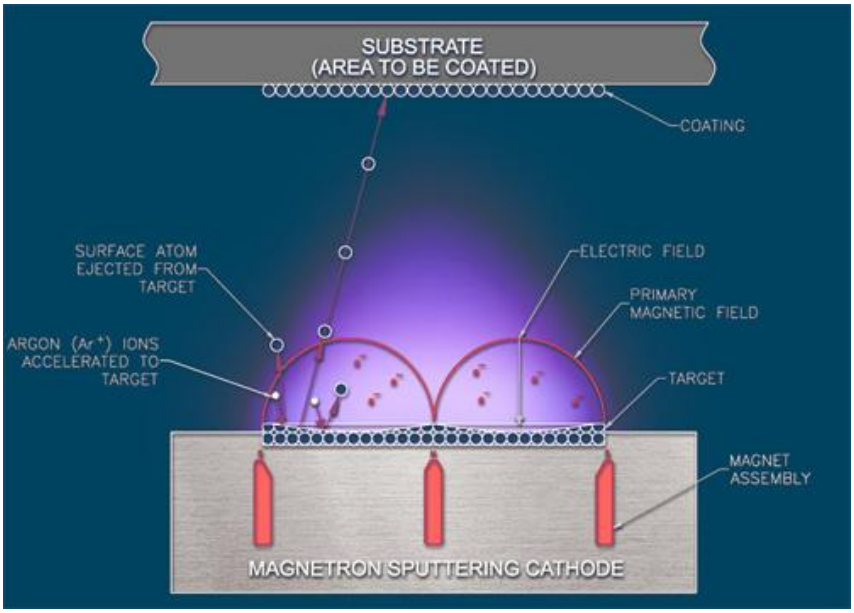

Fig. 2.4 Schematic drawing of the magnetron sputtering process (DC) (image from Wikipedia)

We deposited MTJ multilayer films on thermally oxidized silicon wafers using a homemade multi target high-vacuum magnetron sputtering system (base pressure of 2 $\times 10^{-8}$ Torr). During the sputtering process, the substrates rotate at a constant speed to maximize uniformity throughout each wafer. The new sputtering system provides better stability and lower base pressure, so MTJ stacks are mainly sputtered in the new system. The old sputtering system is mainly responsible for depositing SiO2, gold contact, Fe-Pt alloy or other customized materials. Detailed operations for the new sputtering system (B) are described below:

a. Adjust the Baratron Gauge. (The Gauge should be turned on first by the Labview control panel P5.6). Open the NI Measurement & Automation software and find the Dev2. Click on the Dev 2 and open the test panel. In the test panel, choose Dev2/AI2, and click start. The readings will be shown on the chart continuously. Adjust the screw on the top of the Baratron Gauge and at the same time monitor the readings. Make sure the

reading is around 0 (i.e. -0.01). Adjusting the Baratron Gauge is necessary especially after the system has been idle for a long time or after power shut-down event.

b. Run the "system initialization" vi to communicate with the step motor. Problematic communication with the step motor may cause the motor malfunction, like abnormal common relation speed, clockwise and counter-clockwise rotates randomly and etc.

c. Prepare for the pre-sputtering: 1) turn on the Nitrogen supply valve on the wall; 2) turn on the Nitrogen valve for the "gate valve", for the MFC (mass flow controller), for the solenoid; 3) turn on the Argon gas and turn on the Nitrogen valve for controlling the shutters (around 10 psi).

d. Pre-sputtering: 1) open the "pre-sputtering" vi; 2) set each pre-sputtering time to be 8 minutes (Total should be about 34 minutes); 3) run the program ("Zero Valve" means adjust the valve to 20 degree); 4) make sure readings of the ion gauge are consistent and shutters can be opened/closed freely.

e. If the MgO plasma fails during pre-sputtering: 1) use "Plasma off" vi to turn off all plasma; 2) use "pressure" vi to increase the system pressure to 8 mTorr; 3) turn on the plasma Gun 5 (IrMn) using "plasma on" vi; 4) turn on the plasma of MgO (Gun 8) using "plasma on" vi; 5) if the MgO plasma is on, then turn off IrMn plasma, and pre-sputter MgO target for about 2 minutes, stop the step motor (by entering "ST\r\n") and run the "pre-sputtering" vi again, with each pre-sputtering time shortened to 2 minutes except the MgO target. 6) If the MgO target is still not on, try open shutter and close the shutter quickly using the "smart switch" vi and increase the sputtering pressure more (i.e. 10 mTorr).

f. Open the “Step Motor” vi, and read the current revolution steps (run “EG\r\n”). The EG value should be 24000. If not, (i.e. 20000), enter “EG24000\r\n” and run the vi again to set the EG to 24000.

g. Calculate the recipe of the deposition and fill in the “Deposition-Test-MgO-Thickness.vi”. The rule of selecting depositing substrates (total of 12) is defined by three numbers: if the substrate is going to be deposited, it is denoted as “1” otherwise “0”; so each of the three numbers ranging from 0-7 is converted by 4 indicators correspondingly. The commonly used substrates are 6, 8, 10, and 12 which means the number should be 055. Notice that the deposition sequence always starts from the substrate with the lowest number and ends at the largest number. If arbitrary deposition sequence is needed, Labview software “Deposition-Test-MgO-Thickness-copy 1.vi” can be used.

h. Run the “Deposition-Test-MgO-Thickness.vi” with the “recipe” button un-pressed (on) to double check the deposition recipe.

i. Run the “Deposition-Test-MgO-Thickness.vi” with the “recipe” button pressed (off). All deposition sequence should be completed smoothly.

j. After the deposition, run the “Venting.vi” and turn off everything. “Open Valve” means adjusting the buffer valve to 100 degree.

k. In previous step the gate valve is closed. Open the gate valve using the control panel. l. Turn off the Nitrogen valve for the MFC (mass flow controller), for the solenoid, for the shutter. Turn off the Argon gas.

m. Wait for the system to cool down at least 1 hour.

n. Check the system pressure again right after deposition is done using the “High Vacuum Pressure Indicator Iron Gauge.vi”. This value should be recorded in the log file.

o. Close gate valve, vent the chamber using Nitrogen and open the chamber. Take out wafers and load the new batch of wafers. Clean the wafers surface using air gun and close the chamber properly.

p. Rough pump the chamber using mechanical pump.

q. After the chamber pressure is below 100mTorr, turn the mechanical pump and close the rough valve. Open the Gate Valve and wait for the system to pump down for at least 1 and half days and reach the base pressure.

2.2.5 Photolithography patterning

Photolithography is utilized to transfer a two-dimensional pattern from a physical mask plate to the sample surface. The photoresist used is AZ 5214 from Clariant Inc., which is simply a photosensitive polymer. It could be considered as either positive photoresist or negative photoresist if different recipes are used. For positive photoresist, after exposure of ultra-violet light, the exposed areas of the photoresist become soluble in developer solutions, and vice versa. To achieve high-quality patterns (with sharp edges), contact mode is used and the wafer-to-mask distance is minimized. Positive patterning is normally used to define MTJ or Hall bar structure followed by an ion mill etching procedure. The sequence is described below:

a. Clean the surface of the wafer using air gun. If the wafer surface is noticeably dirty, acetone cleaning is recommended. After acetone rinse, make sure to blow all residue acetone away from the sample side of the wafer as acetone dissolves photoresist. Usually, there should be a couple of minutes after acetone cleaning and before applying photoresist.

b. Turn on the thermal heater to 105 ºC. For the positive patterning, only one heater is needed. Put the metal substrate holder on top of the hot surface and measure the surface temperature using a thermometer. Typically it will take about 10 minutes for the temperature to rise to 105 ºC from room temperature.

c. Prepare the timer and set the timer as 2 minutes while waiting. Open the gas line for the spinner and set the spinning parameter accordingly. Double check the vacuum is good for holding the wafer by several test runs.

d. Carefully put the wafer onto the spinner and adjust it to the center. Check the centering and vacuum holder by test runs. Clean the transfer pipe using air gun to remove dust, and then evenly apply photoresist onto the wafer. After coating, bake the wafer for 2 minutes on the heater station. Clean up the mask while waiting.

e. All wafers should be kept in the tool box, away from light, after spin coating is finished.

f. Turn on the photolithography aligner and change to the right settings: timing (22 s), 365 nm filter, and constant power mode. Put on the mask and make sure the mask is centered and tightened.

g. Carefully align the wafer with the mask by trials (using the microscope if necessary).

h. After exposure for 22 seconds, dip the whole wafer in the developer (AZ 917) while timing. This is a critical step to achieve good quality sample. Although the developing time is relatively constant from sample to sample, i.e. 15 seconds, the surface pattern of the wafer while developing should be closely observed. Wafer should be removed from the developer immediately once the color of the patterned surface does not change in the developer to avoid over-developing.

i. Rinse the wafer using DI water and dry the wafer with air gun. If the patterns are colorful on the surface, the wafer is under-developed. Further developing is needed by carefully monitoring the changing patterns of the wafer surface developed in short periods (i.e. 2 seconds).

Slightly complicated than the positive photolithography patterning, negative patterning requires two baking processes—first soft baking at lower temperature (90 ºC) and second hard baking at higher temperature (125 ºC), as further detailed description listed below:

a. Clean wafer surface using same method.

b. Turn on the first thermal heater to 90 ºC, and the second heater to 125 ºC. (It is possible that the display is 140 ºC while the real temperature of the heater surface is 125 ºC). Temperature should be monitored by the thermometer.

c. Spin coating the photoresist first soft bake for 2 minutes.

d. After alignment on the photolithography aligner and 6-second exposure, bake the wafer again at 125 ºC for 1 minute. This second baking temperature (125 ºC) is critical to achieve high-quality sample, so it should be carefully measured by the thermometer.

e. After one minute exposure without mask, develop the wafer and rinse.

It is possible that the thickness of the photoresist after negative patterning is different from positive patterning, but both should be within the range of 1.2~1.4 μm. If the thickness in out of the range, i.e. 0.9 μm, it is possible the wafer is under-developed, or over-developed, which could be double checked under microscope. In this case, the patterning process needs to be done all over again after completely removing the

photoresist by acetone (and sonicating). Otherwise, a following ion beam etching process will be affected and the etching depth might be incorrect.

2.2.6 Ion beam etching

To define MTJ patterns after photolithography patterning, ion beam etching is used for its high directionality and low material selectivity. In the process chamber of an ion beam etcher, electrons boil off the hot filament and are accelerated towards the anode grid. Electrons then impact the neutral gas atoms (usually Ar), so the working gas breaks into ions and electrons after a critical threshold voltage (40 V) is reached. The positively charged Ar^+ ions move quickly under the influence of 500-1000 V accelerating potentials. The energetic ions then arrive at the wafer surface and knock the target atoms out of the sample. The ion beam etcher has the direct and independent control over both the ion flux and ion bombardment energy. Typically, the etching rates depend linearly on the ion current density but non-linearly with the ion bombardment energy. A magnetic field about 100 Gauss is often used to trap the electrons, so the ionization rate is increased. To prevent the positively charged ions from building up on the wafer plate, a neutralizer filament is placed after the alignment grid to avoid the charging effects. A schematic drawing of an ion beam etcher is shown in Figure 2.5.

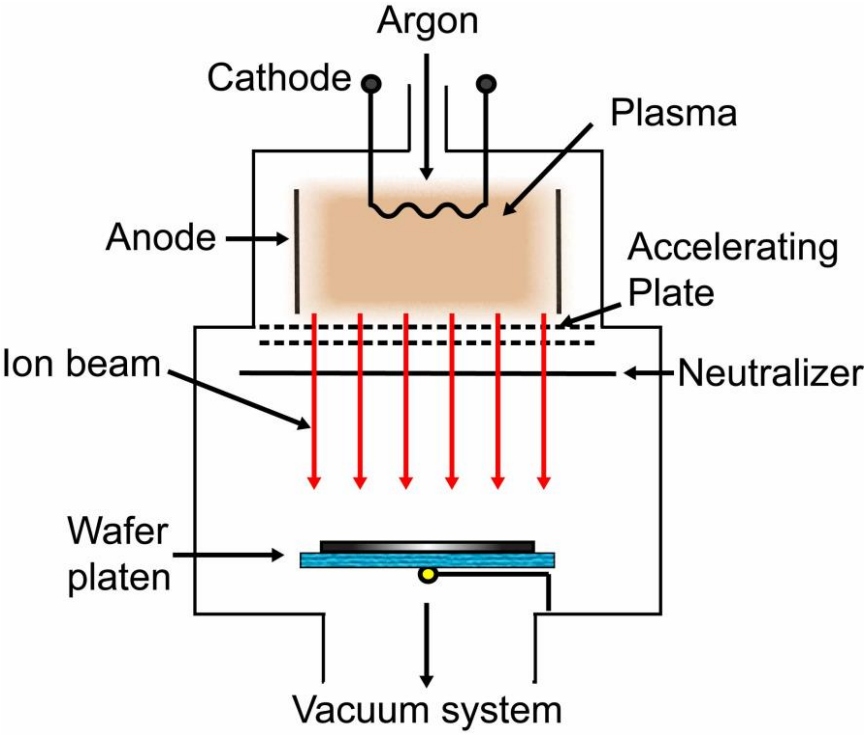

Fig. 2.5: Illustration of an ion beam etching system.

Normally there will be two slightly different etching procedures, i.e. when defining MTJ array structures. The first ion etching process is widely used to define isolated areas, either MTJ or Hall Bar shapes, so that the etching is down to the substrate layer. In this situation, the incident angle of the ion beam during etching is 80 degree, which means the ion beam is almost perpendicular to the wafer surface. This process is fast but ignores the sidewall effects. This etching method is only used when the required etching has to be deep and the sidewall contamination is not a concern. A different ion beam etching procedure is used to define thinner structure and to eliminate the sidewall effect. During ion beam etching, non-volatile material tends to re-deposit on nearby surfaces, for example, the sidewalls. If the etched material accumulates on the sidewalls of a junction in the MTJ structure, the junction will be shorted. In order to remove the accumulated materials on the sidewalls, the incident angle of the ion beam is adjusted

during the etching procedure. Meanwhile, the rate of sidewall re-deposition can be made to exactly match the rate of etching.

The only difference between operating the two etching processes is the incident angle. The first etching method fixes the incident angle at 80 degree while the second etching method varies the incident angle at 45 degree and 10 degrees, back and forth. When the incident angle is 45 degree, the surface of the sample is being etched and the sidewall accumulation rate is faster than the etch rate. When the incident angle is 10 degree, the surface of the sample is still being etched at a slower rate and the sidewall accumulation rate is now slower than the etch rate. Careful control of the ion beam etching procedure can help to completely remove the sidewall effect and achieve optimal sample quality. The operation procedure is described as below:

a. Vent the chamber for a few minutes.

b. Close the vent line and open the chamber gate.

c. Clean the ceramic rings and load the samples using sand paper. Make sure there is no copper exposed when placing the wafers and the rings.

d. Clean the sample surface by the air gun.

e. Close the chamber and turn on the rough pump. When the chamber pressure is low (lower than the red line), turn off rough pump and switch to HI VAC mode.

f. After 50 minutes pumping, the chamber pressure should be below 2×10^{-6} Torr.

g. Turn on water and Argon gas.

h. Wait until the Argon gas flow rate reading is stable.

i. Turn the flow controller switch to manual mode first to see the pressure change from the gauge then immediately switch to auto mode. Wait until the flow rate reading is stable (5 minutes).

j. Turn on power supply for the spinner motor and set to 22V.

k. Turn on the ion milling main power switch and wait about one and a half minute. If there is no reading, turn off and on again.

l. Adjust the reading to 142 and neutralizer to 0, back and forth.

m. When everything is ready, write down the recipe.

n. Open the valve and start the timing.

o. Follow the recipe and record readings. Make sure the ion current reading is always about 0.017 (A).

p. When the recipe is finished, turn off the main power switch of ion milling station, move the plate back to original position and close the valve.

q. Turn off the spinner power supply. Turn off the flow controller, the Ar gas line, the cooling water and the vacuum gauge.

r. Wait for 1 hour and 20 minutes for the filament to cool down before venting the system and taking the wafers.

As an example, the first etching recipe (constant incident angle at 80 degree) is often used in the first ion mill etching procedure while defining MTJ structure because the total thickness of the whole MTJ stack has to be etched through. In other cases, the second etching method is more desirable in order to eliminate sidewall effect and prevent electric shorts in the sample. Because the etching depth has to be carefully controlled, a calibration of the relationship between ion milling time and the etching depth is required.

As shown in Figure 2.6, the calibration is done for both etching methods: 80 degree continuous etching and 45/10 degree angle-varying etching, on different samples with different ion milling time lengths. According this calibration results, the etching rate for 80 degree continuous etching method is about 2.15A/s (faster) while for the 45/10 angle-varying etching the rate is 1.76A/s (slower).

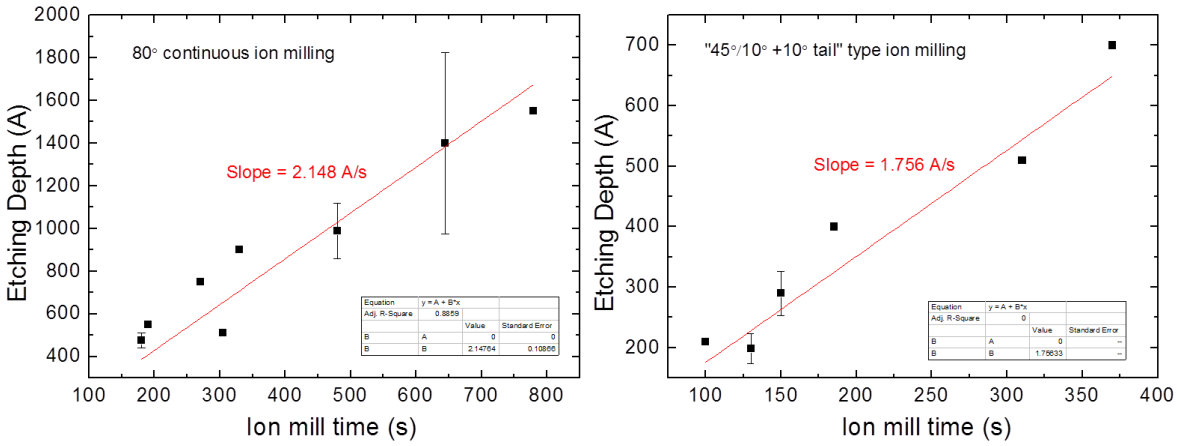

Fig. 2.6: Etching depth as a function of ion milling time for the two different etching methods

It is noteworthy that the etching rate is around 2Å/s for both methods, which is slow enough for delicate etching depth control. For instance, the second etching procedure in defining MTJ structure requires the etching is down to the IrMn layer in order to isolate the pinned layer (but not the pinning layer). The acceptable etching depth variance is about 180 Å and both the etching time and ion beam current should be carefully controlled. As shown in Figure 2.6, three repeats (45 seconds for each repeat) of 45/10 degree etching give an etched depth of 710 Å. An addition of 30 seconds of 10 degree etching is expected to further remove the side-wall re-deposition, and the total etched depth is around 750 Å. The etching procedure stops in IrMn, which is 100 Å above the highly conductive bottom electrode of the MTJ and 100 Å below the MgO tunnel barrier. The TMR ratio and wafer uniformity are found to be optimal with these

etching parameters. However, it might be more difficult to define a Hall bar structure on a conducting Hall material strip for GSHE device, which has a typical thickness of 40 Å (as this will be the etching depth tolerance). Careful calibrations and timing are essential to fabricate high-quality multilayer structures.

2.2.7 Magnetron Sputtering: Old Sputtering System (A)

The old sputtering system has similar functions to the new sputtering system and it is only used for simple or customized sputtering deposition, such as the SiO_2 deposition, gold contact deposition or the Fe-Pt co-sputtering deposition (common rotation method). An example is the SiO_2 deposition during the MTJ fabrication, after the second ion beam etching, for separating the bottom and top electrodes. The base pressure of this system is about 1×10^{-7} Torr, and the SiO_2 deposition is done via RF sputtering in a mixed argon-oxygen environment with a pressure of 8.5 mTorr and an Ar/O_2 ratio of 3:1. A forward RF power of 150 W is used throughout the deposition, and the growth rate is about 1 Å /sec. The detailed process sequence below is for SiO_2 (RF) deposition:

a) Load the sample wafers (up to 6). Use air gun to clean the sample surface.
b) Close the top lid of the system carefully by adjusting the lid position and the bottom rotator. Turn on and off the bottom rotator to make sure self-rotation is smooth.
c) Connect the power strip of the mechanical pump and open the rough valve to rough the chamber down to 150 mTorr (typically takes about 10 to 15 minutes).
d) Close the rough valve and disconnect the power of the mechanical pump. Open the nitrogen tank for gate valve/shutter switch and adjust the regulator to 50 psi. Switch to gate valve control and open the gate valve. Close the nitrogen tank valve.

e) Check the pressure of the chamber and it should go down to 1×10^{-4} Torr quickly (within a minute).

f) Wait for the system to pump down for at least overnight before reaching 1×10^{-7} Torr.

g) Check the flux rate reading is around zero, at least to the hundredth.

h) Turn on the cooling water for the corresponding guns (it is suggested to turn on all cooling water in case of making any mistake)

i) Open the nitrogen tanks for controlling solenoid and shutters.

j) Open the Argon and Oxygen gas tanks valves and turn on the solenoid control for the two gas lines.

k) Turn on the MKS and wait for the actual readings to decrease to zero, set (or double check) the MKS reading to 65 for channel 1 and 26 for channel 2.

l) While waiting for the MKS reading to be stable, double check the correct power cable is connected to the corresponding guns, and double check the switch box (controlling DC power) is switched to the correct gun. Connect the step motor power (connect the wire then the power cable). Also turn on the switch box on the desk to setup the step motor communication.

m) Turn the buffer valve to about 30 degree. Then the reading of the flux rate should be around 8. This is the preferred flux rate for pre-sputtering procedure, and could be changed by adjusting the buffer valve.

n) Double check the gas pressure for shutter control is not too high or too low for the corresponding shutters (around 30 psi). Then test the shutter so that it can be opened or closed freely. This shutter open/close testing is necessary before sputtering because

the shutter opens very slowly at the 1st time and hence will affect the sputtering time significantly.

o) Run the system initialization vi and carefully align the wafer with the mark on the chamber window and with axis of the rotator in the center of the chamber. Click set variable to record the parameters.

p) Turn on the plasma using RF power supply at a power of 150W. The pre-sputtering procedure will take about 8 minutes for each target.

q) While waiting for the pre-sputtering process to complete, fill in the deposition information in the deposition vi and double check thickness and the loaded wafer positions.

r) Run the deposition vi. And the desired material will be sputtered in the defined time.

s) After deposition is done, turn off the RF power supply, disconnect the power of the step motor, and turn off all the gases, the self-rotation, and the cooling water. Change the buffer valve to 90 degree (fully open) and wait for at least 1 hour for the system to cool down.

t) Before venting the chamber, turn on the nitrogen tank for gate valve control. Switch the gate valve/shutter switch to control gate valve and close the gate valve.

u) After making sure the gate valve is fully closed, open the nitrogen tank for venting the system and switch on the vent valve. Wait until the pressure reaches atmosphere. Turn off the vent valve and close the gas tank valve.

v) Open the chamber and carefully transfer the top lid to the lid holder cart and unload the wafers. Normally, a lift-off procedure is followed.

It should be noted that the RF sputtering is sometimes hard when igniting the plasma and the tricks to start the plasma is similar to the process described in the new sputtering system section. The keys to ignite plasma for the first time include increasing the Ar sputtering pressure (to the maximum) by closing the buffer valve, increasing the RF power, i.e. from 120 W to 150 W, generating plasma on another target close to the RF powered target using DC power, turning on and off the shutter and etc.

2.2.8 E-beam Evaporation: Gold contact deposition

E-beam evaporation is another PVD different from magnetron sputtering deposition. It carries a piece of the target material in a crucible and uses electron beam to heat up to its melting point in a vacuum chamber (as shown in Fig. 2.7) typically 1×10^{-6} Torr in the system at the clean room. Operations should be following the provided manual in the clean room.

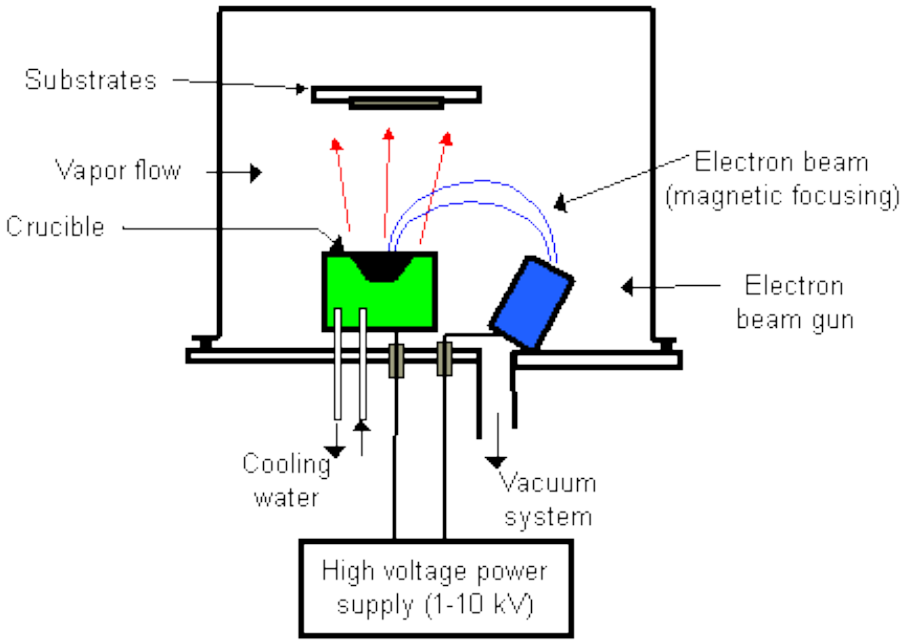

Fig. 2.7 Schematic drawing of the e-beam evaporation setup

E-beam evaporation is used to deposit 100 Å Ti and 1000 Å gold on the exposed area of the patterned wafers, and it is the old method we used to deposit gold contact on MTJ samples. The materials to be deposited are located in two source crucibles (with a rotator to switch). High density electron beam is bombarded on the source materials. The sublimed materials will travel across the vacuum chamber then deposit on the wafer substrates. A thin film of Ti (100 Å) is deposited prior to gold evaporation to improve the adhesion of the gold film. A thickness monitor made of quartz crystal is used to detect the deposition rate and total thickness. A typical deposition rate is 1 Å/s, and the timing is easily controlled by opening/closing the shutter.

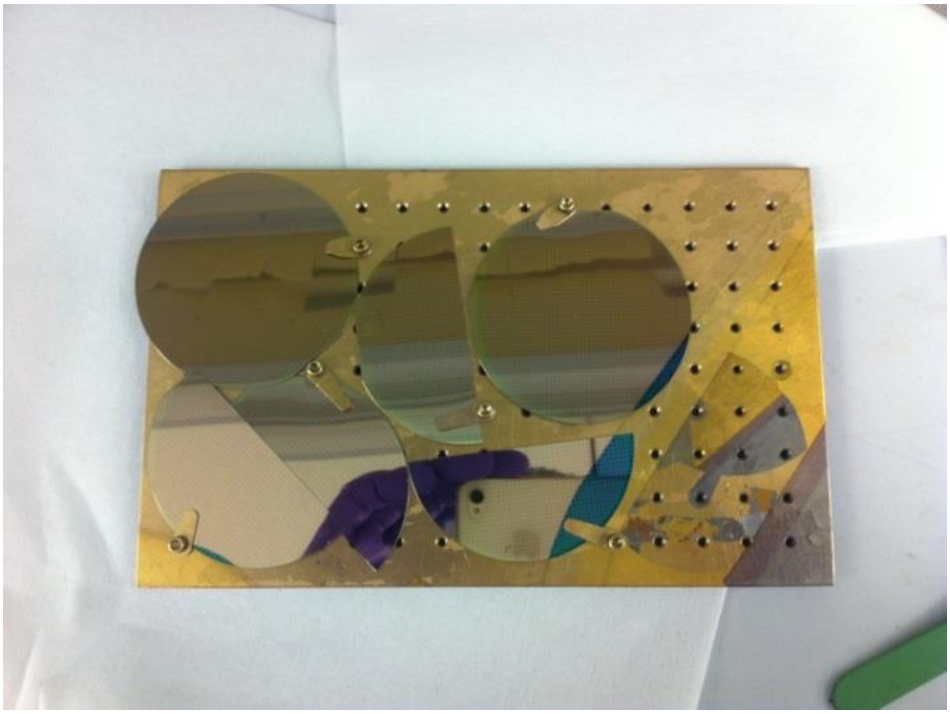

Fig. 2.8: Example of wafer arrangement for E-beam evaporation deposition

One of the difficulties related to using the e-beam deposition system is the arrangement of the wafers on the provided substrate holder. Since the shutter should be able to cover all wafers on the holder when it is closed while uncover all of them after being opened, there might be only three whole wafers possibly placed on the holder due

to the limited area of the substrate holder and the shutter orientation. However, if wafers can be cut into halves, then a typical arrangement of four wafers on the substrate holder is shown in Figure 2.8. In this setup however, it is important to label all the wafer pieces accordingly.

2.2.9 Lift-Off procedure

The lift-off procedure is to remove the gold or the SiO_2 deposited on top of the photoresist area. Sonicating time in acetone might be longer than 2 minutes, depending on the material (SiO_2 or Gold) and deposit methods (E-beam evaporation or magnetron sputtering deposition). We have noticed that the lift-off time is longer after E-beam evaporation compared to that after sputtering deposition. Also, lifting-off SiO_2 deposits sometimes might be hard and may require sonicating in a heated up environment (45 ºC) or even manually (gently) wiping the wafer using cotton stick. After the lift-off process, the pattern on the wafer should be checked again under microscope to ensure complete lift-off.

2.2.10 Magnetic thermal annealing

Magnetic thermal annealing is also a critical procedure to achieve high quality samples. It is done in a high vacuum below 10^{-6} Torr under the magnetic field of 0.45 Tesla. According to different configurations, the magnetic field could be arranged perpendicular or in-plane to the sample surface. In MTJ fabrication, this is the final step in order to set up the magnetization easy axis and exchange bias in the SAF trilayer structure. Note that the magnetic thermal annealing will also help remove the lattice disorder and crystallize the CoFeB layer using MgO (001) layer as a template. In the development of Giant Spin Hall Effect device, this step has been proved critical to

achieve the perpendicular magnetic anisotropy in a ferromagnetic layer adjacent to the GSHE solid. A small variance in annealing temperature (+/-20 ºC) may lead to failure in achieving perpendicular magnetic anisotropy in a certain layered structure. Therefore, for our study purpose, the wafer should be cut into pieces and being annealed piece by piece in order to find the optimal annealing conditions. The detailed magnetic thermal annealing process is described below:

a) Close the gate valve and turn off the power of the turbo pump. (The mechanical pump should be turned off after about 20 minutes) Vent the chamber by turning the vent valve, stop if strong whistling sound can be heard. After chamber reaches the atmosphere, close the vent valve and open the chamber door.

b) Prepare the wafers on the substrate holder. If it is for in-plane magnetic thermal annealing, there will be 4~5 slots to plug in the substrate holders for 2-inch wafers; if perpendicular magnetic thermal annealing process is required, only one substrate holder (in perpendicular configuration) will fit into the metal box. This holder may hold up to 4 smaller pieces of the 2-inch wafer.

c) Carefully put the holder into the copper box and center it. Avoid any magnetic tool near the box because of the strong magnetic field!!

d) Close the chamber door, open the rough valve and pump down the system using mechanical pump.

e) After the chamber pressure drops below 100 mTorr, close the rough valve and turn on the turbo pump power. Double-check the cooling water is on before opening the gate valve.

f) Wait for about 30 minutes till the chamber reaches high vacuum (10^{-6} Torr). While waiting for the pump down, edit the thermal controller profile if necessary.

g) Turn on the thermal heater. Wait the temperature profile to complete and natural cooling down, which may take over night.

The high vacuum and temperature profile are most important in the thermal annealing process. A desirable high vacuum could be achieved after one hour of pumping down procedure. In order to achieve the optimal thermal annealing condition, a temperature profile consisting of multi-step heating temperatures is applied to achieve smooth temperature control and avoid overheating, which is bad for MTJ and also for the perpendicular magnetic anisotropy in GSHE devices. A typical temperature profile could be written as: $160_{20}^{20} + 210_{15}^{20} + 240_{15}^{15} + 260_{10}^{10} + 270_{5}^{10} + 280_{60}^{5}$. Here, for instance, the 2nd step is rising the temperature from 160 °C to 210 °C in 20 minutes plus waiting for 15 minutes. When studying the annealing temperature effect, only the changes of the final temperature is needed and the temperature ramping profiles are kept as unchanged as possible. Such detailed study will be presented in the chapter 6 when studying the relationship between magnetic thermal annealing procedure and achieving perpendicular magnetic anisotropy in the Ta/$Co_{40}Fe_{40}B_{20}$/MgO structure.

2.3 Quick-test method and electrodes setup

2.3.1 Quick-test method

To improve the magnetic and electric properties of magnetic tunnel junctions (i.e. the tunneling magnetoresistance), the layered structure of MTJ needs to be improved

gradually. A standard fabrication process contains seven steps, including 3 steps of photolithography patterning, 2 steps of ion beam etching, 1 step of SiO_2 deposition, and 1 step of gold deposition (before magnetic thermal annealing). In order to verify the properties between different batches during the troubleshooting process in a relatively short time, we developed a short-loop fabrication process, which uses only 2 steps instead of 7 and allows for quick measurement of MR ratios (1 step of photolithograph patterning and 1 step of ion beam etching). The short-loop process can accelerate the MTJ development cycle by a factor of 3, and hence greatly shorten the period of improving the TMR ratios. This procedure is similar to that of developing Hall bar structure. However, it should be noted that the quick-test method may introduce lower MR ratios compared to the same-quality MTJ under standard fabrication process. According to empirical results, when the TMR ratios is higher than 50% in quick test method, it is highly possible that a standard fabrication process will generate high quality MTJ with MR ratio higher than 100% assuming other parameters being unchanged.

The basic idea of the short-loop process is to define two neighboring MTJ junctions, where electrons can travel from the top electrode of the first MTJ unit, and tunnel through the MgO insulating layer of the first unit to the shared bottom electrode. From there, electrons tunnel through the MgO insulating layer to the top electrode of the second MTJ unit. The short-loop process can be achieved by defining two neighboring MTJ units with one photolithography patterning, followed by an ion beam etching. The etching depth is carefully controlled so that the etching stops just below the MgO barrier. The MR ratio can be obtained by measuring the resistance change of two MTJ elements

connected in series (as they share the same bottom electrode) with a micromanipulator (probe) station. A schematic drawing of the short-loop pattern is shown in Figure 2.9.

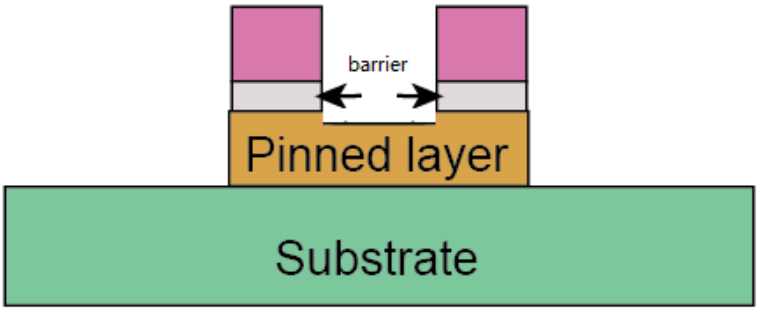

Fig. 2.9: Schematic of short-loop pattern.

One outstanding issue with the short-loop process is carefully controlling the etching rate of the ion beam etching system. First, this process must etch through the MgO tunnel barrier, otherwise top electrodes of the MTJ elements would be connected and electrons would bypass the tunneling barriers. On the other hand, the lack of control on the etching depth, i.e. over-etching in the pinning layer, may diminish the effective TMR ratio. Besides, in order to reduce the side-wall re-deposition during the ion beam etching procedure, we alternate the incident angle of the ion beam between 45 and 10 degree (the second ion milling etching method). To calibrate the etching rate at different ion milling conditions, we measure the etching depths at different combinations of etching time and incident angles. This calibration results are shown in Fig. 2.6 and are used for controlling the etching depth during ion milling process. Accordingly, the ion milling time has to be precisely controlled with all other parameters (i.e. the ion beam current) unchanged. Another potential issue with the quick-test method is the lack of the

gold contacts, making the following electron transport measurement quite difficult. A probe station is often used for the transport measurement, such as the transfer curve measurement, after the quick-test sample wafer is ready (after magnetic thermal annealing). It is inevitable to have direct mechanical contact on the top of the MTJ stack during measurement that may damage the tunneling junction, so the following measurement operation has to be done carefully and gently.

2.3.2 Probe Station

The probe station used for transport measurement on the sample wafer mainly includes a microscope and four probes on a well-leveled table with cushions to reduce vibration. The probes are held on top of the table tightly through magnets, and they are connected through wires to measurement equipment, i.e. a current source and a voltage-meter. The probes can be smoothly moved in three directions, and the movement of the tip of the needle should be timely monitored in the microscope. Once the needle touches the surface of the wafer while moving downward the probe, it will be bended to some extent that can be observed in the microscope. The touch of the probe onto the sample surface cannot be too harsh in case of mechanically damaging the sample, especially the quick-test MTJ sample because of the thin tunneling barrier and the lack of gold contact layer.

Besides the electrical setup, there are two types of magnetic field setup, one with external magnetic field applied perpendicular to the wafer surface and the other one with two-dimensional external magnetic field applied in the surface plane. The variable parameters in the transport measurement are the magnetic field (direction and magnitude), current and bias voltage. It is commonly a circle transfer curve, liner transfer

curve, or a Hall voltage measurement which will be presented in following chapters. Once the measurement is being taken, any environmental vibration should be avoided since the probe contact is really sensitive to mechanical vibration.

2.3.3 Wire bonding

The wire bonder is another solution to make solid contact between sample leads, i.e. the Hall bar, and the pads on a wired sample holder. Such as solid electrical connection makes the method performs much better in the most cases than the probe station which cause damage to the layered structure on a wafer. If the sample has gold contact deposited, it will be much easier to bond due to larger bonding area and the more adhesive gold layer. But before gold deposition, there will be a thinner layer of Cr (magnetron sputtering) or Ti (E-beam evaporation) deposited to improve the adhesiveness between the gold layer and the sample stack. Without this adhesive layer, gold contact might be easily peeled off during wire bond.

The wire bonder has two different types, wedge bond or ball bond. For a wedge bond, a wire (Al or Gold) will need to be placed through a pinhole on a wedge needle, and the ultrasonic vibration will cause the wire to melt while making contact to the sample surface and establish the connection. It should be noticed that bonding parameters are different between Aluminum wire and gold wire because of their different melting point and stiffness. The tail left after the first bonding step is adjustable and would be as short as possible to keep close traveling distance between two bonding spots. It takes two steps to make a successful bond. The first step bonds the wire with the first spot (lead on a thin film sample or pads on a sample holder). After moving the wedge above the second spot, make another bond then the wire will be cut automatically. The traveling distance

between two connections cannot be too far, i.e. 1 cm. Otherwise, it will be easy to drag the wire off the first bonding spot; or, the wire might touch the sample surface or other wire due to weight, leading to a possible short circuit.

The ball bond process only differs in the first bonding step compared to the wedge bond. A gold wire is used in this bonding type, and a high voltage bias is applied on the tip of the wire which makes the gold wire melt on the tip and forms a ball. Because of the much larger diameter of this golden ball than that of the wire itself, it makes the contact area much larger during wire bonding and thus much easier to make successful bonding. Therefore, for those thin film samples which are hard to make wire bond, a ball bonding may be a better solution.

2.4 Other Experimental Methods

As introduced in the previous section, most of the fabrication procedures are related to the MTJ fabrication. This section will be discussing other experimental methods that have not been covered in Section 2.3.

2.4.1 Common Rotation Method: making Fe-Pt alloy thin film

The common rotation method is only used to deposit alloy (Fe-Pt) in the old sputtering system. Because of the lack of co-sputtering targets in the system (all targets facing straight up and all substrates facing straight down, alloy has been made by turning on the plasmas on two targets together (with shutter constantly open) and rotating the substrate plate. The wafers with self-rotation will also have common rotation and travel

through the top of both targets consecutively. A demonstration is shown below (Fig. 2.10).

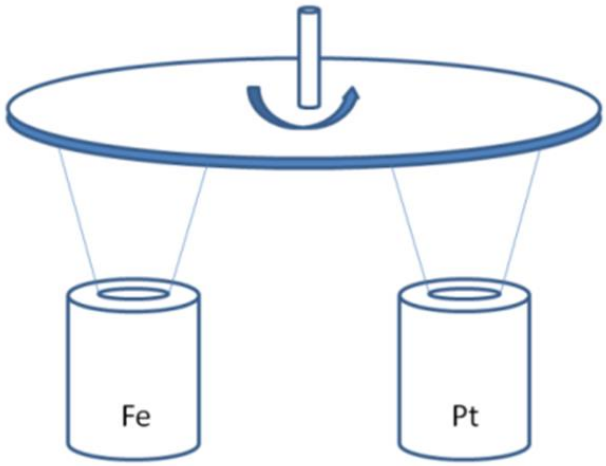

Fig. 2.10 Schematic drawing of common rotation method

Before the common rotation method was invented in making alloy, we move the substrate holder back and forth between the two targets with both shutters open (because mechanically opening and closing the shutters takes time and then will affect the deposition time). However, this old method always results in inaccurate concentration of the alloy because of the mechanical pause (the step motor going back to the home position every time when travelling between the two target positions) during the movement of the substrate plate. To solve this problem, we invented the common rotation method which turned out to be an effective solution to make alloys in the old sputtering system. This method succeeds in making thin alloy samples with great uniformity and variable concentration by adjusting the deposition power of one material while keeping the other one unchanged. A calibration of the deposition rate (thickness per rotation) of both materials is necessary before making the alloy. The linearly fitted slope in the

correlation between deposition thickness and deposition power (DC) as shown in Figure 2.11 determines the deposition power of Pt based on a desired concentration of the Fe-Pt alloy. The deposition rate of Fe is kept constant by fixing the deposition power.

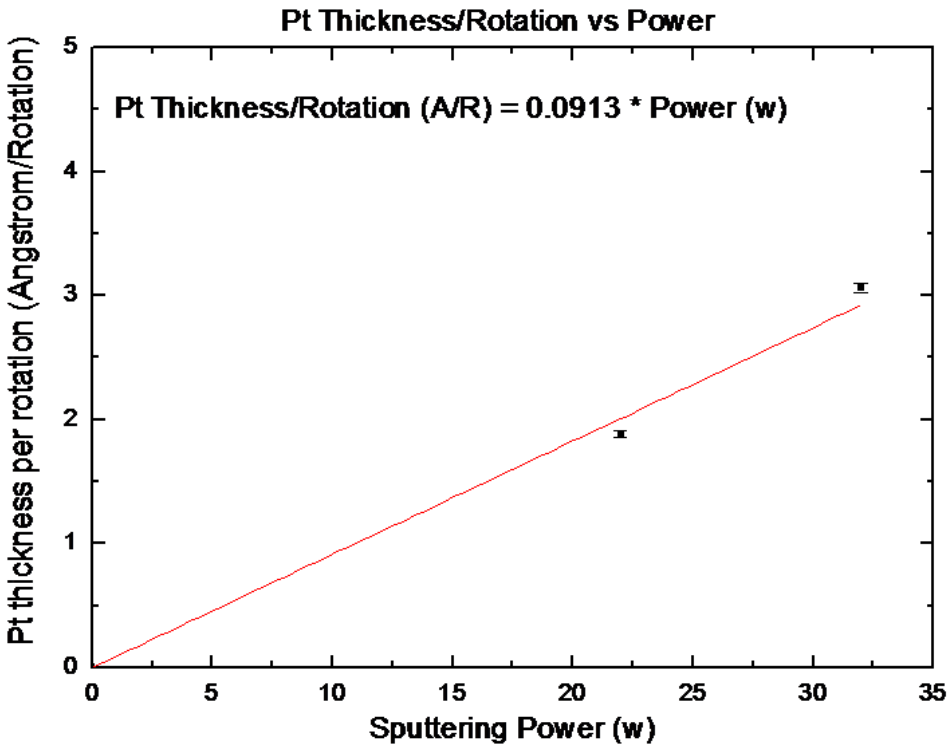

Fig. 2.11: Calibration curve of sputtering power vs. Pt thickness per rotation

For the Fe-Pt alloy with a given thickness and concentration, the required deposition thicknesses for both materials can be calculated. Since we fix the deposition rate of Fe, the total deposition time is known, which determines the total number of the rotations. Due to the fact of common rotation, the number of rotation for Fe and Pt are the same, which implies the Pt deposition rate is known as well. Given the linear relationship between the Pt thickness per rotation and the deposition power (Fig. 2.11), the required deposition power of Pt can be derived.

2.4.2 Low Power Deposition: beta-Ta and beta-W

The deposition of beta-Ta and beta-W is completed in the new sputtering system with different deposition conditions. The key difference is to minimize the growth rate as low as possible, since eliminating the deposit heating has been demonstrated to be essential to achieve beta-Ta and beta-W thin film.

(a) β-Ta thin film deposition:

The beta-Ta thin film, or the beta-Ta/CoFeB/MgO layered structure is deposited on thermally oxidized Si wafers in a homemade high vacuum magnetron sputtering system with a base pressure less than 2×10^{-8} Torr and Ar sputtering pressure ~2 mTorr. The face-up sputtering guns have a diameter of 5 cm and use an NdFeB permanent magnet ring. The target-substrate distance is 9 cm. The face-down substrates are thermally oxidized single crystal Si wafers (5-cm diameter), which rotate at about 50 rpm during deposition for achieving thickness uniformity. The off-center distance is 3 cm between the center of a substrate and that of a target. (A capping layer of Ta was deposited on top of the layered structure to prevent oxidation of the metal layers from atmosphere). The growth rate of Ta was about 0.5Å/s under a DC sputtering power of 10W, and the substrates were kept at ambient temperature. In this way, the deposition heating on the substrates is minimized and the beta-Ta is obtained.

(b) β-W thin film deposition:

The substrate is 2-inch Si wafer with thermally oxidized layer of about 2 um. Before deposition, 4 Si/SiO_2 substrates are loaded on the position of 6, 8, 10, 12 so that each of them is well separated with least possibility of contamination between each other. The chamber is then pumped over at least 2 days so that base pressure is at least 2×10^{-8} Torr. (One day pumping may have the system with a base pressure of 3×10^{-8} Torr but the beta

phase of W thin film was also obtained). Before W deposition, we used to run a 2-minute-long quick pre-sputtering procedure, which pre-sputters CoFe and CoFeB together for 4 times (DC power is 15W), each time being half a minute. Later, we found out that pre-sputtering tends to introduce the ferromagnetic contamination even with the shutters closed, so I conducted W thin film deposition without CoFe/CoFeB pre-sputtering and the beta phase was achieved. It is also worth noting that pre-sputtering W for long time (8 minutes with shutter closed) before the real deposition procedure resulted in the alpha phase W thin film deposited (all other conditions remaining the same), probably due to the consumption of the small amounts of oxygen left in the chamber due to the long time pre-sputtering procedure (which used to be 15W DC power and caused faster oxygen consumption). Therefore, the ideal sputtering condition is to skip the entire pre-sputtering procedure and always conduct W deposition directly after system reaching a proper base pressure to obtain the beta phase.

During W sputtering procedure, the Ar pressure is about 2.2 mTorr. The DC sputtering power of W is kept to be 3w, which was well calibrated to ensure the deposition rate of W is below 0.02 nm/s (i.e. 0.018 nm/s). The deposition procedure is done by multiple "runs": for each run, the deposition thickness is 0.5 nm on each wafer position, i.e. 6, 8, 10, 12 and 3 which has no substrate. On each run, W deposition started from position 3 (no substrate) so that we have enough time to change the DC power from the initially set 15W to 3W, and to monitor the plasma and carefully adjust the power. In this way, the deposition heating on the substrates can be minimized to get consistent β-W up to 27 nm. If the desired thicknesses of W on each substrate are different, we can just control the corresponding times of runs for each substrate. Between each run, the

deposition sequence always starts at position 3 (no substrate position), so that deposition on previous run has sufficient time of at least 27.8s (0.5/0.018) to prevent substrate heating. When the W deposition is finished on all substrates, DC power is manually brought back to 10w for the deposition of CoFeB on each wafer, if layered structure is needed, using normal magnetron sputtering procedures.

2.4.3 Making Composite Target

In this section, the brief procedure of making composite target will be discussed. The target will then be used in the magnetron sputtering system for thin film deposition. Detailed procedure is listed as following:

a) Calculate carefully the mass of the original materials (powders) needed to make the composite, by using their mole mass, density, and the size of the final target (i.e. 2 inch diameter and 1/8 inch thick). For example, La_2O_3, $SrCO_3$, CuO are used to make $La_{1.9}Sr_{0.1}Cu_1O_4$. The residue Carbon and Oxygen will be released during annealing process.

b) Weigh the mass of all powders according to the calculation by the balance. The paper used to hold the powder should be big enough to prevent drop of powers during transferring.

c) (All the tools have to be cleaned by acetone, sandpaper and wipes) Mix all the powders in a mortar. Pour in the largest amount of powder first, the next, and finally the least amount of powder. This is to avoid the smallest amount of powdered being adhered on the walls of the mortar, which affects the composite the most. The mortar should be large enough.

d) Smoothly and carefully grind the powders in the mortar by the corresponding set of pestle. This procedure should be longer than half an hour. If the powders are mixed uniformly, the color of the mixture should appear uniform. It is recommended to anneal the powders (for instance, at 900 ºC) before pressing to shrink the volume.

e) Carefully transfer the powder in the pressing tools, and make sure the surface of the powder is even. Try to transfer the powders on the mortar wall as much as possible.

f) Use the pressing tool to make the target well pressed (above 45 ton). Make sure the alignment is good. Leave the powders being pressed for 1 and half minutes.

g) Release the presser, and take out the pressed target. The pressing tool can be used to squeeze out the target in the opposite direction that used to press the target. The process should be smooth without any squeezing sound (which means abrupt friction between target edge and the holder cavity). During this procedure, it should be relatively easy to press out the target, and the pressure indicator should not increase too much.

h) After removing the target out of the cavity, transfer the target on a crucible plate for following annealing procedure. At this step, it is possible that the volume (thickness) of the target is much different from predicted if the powders are not pre-annealed in step 4. The volume may shrink by 30% if it was not pre-annealed.

i) High quality target should not have cracks on the surface or the edge before annealing, so that after annealing the target will not break in to pieces. (Some of the powder should be saved for XRD or other examination.)

j) Anneal the target at a desired temperature. The ramping temperature should not be too fast. After annealing, natural cooling down of the furnace will take over night.

The quality of the target after annealing could be verified by the color (darker means annealing temperature is sufficient). Otherwise, higher annealing temperature should be applied but carefully controlled.

2.5 Quantum Design® Physical Property Measurement System (PPMS)

2.5.1 PPMS Introduction

The Quantum Design PPMS represents a unique concept in laboratory equipment: an open architecture, variable temperature-field system, designed to perform a variety of automated measurements. It enables the measurement within magnetic field up to ±9 tesla and temperature range of 2-400 K, including VSM Option (VSM), AC Susceptibility &DC Magnetization Option (ACMS), Ultra Low Field Option (ULF), Electrical Transport Option (ETO), and Thermal Transport Option (TTO).

Overall, the PPMS consists of 4 main parts: sample chamber, controller, compressor and cooling system. For transport measurement, samples could be mounted onto a 12 pins sample puck and installed in the 12 leads built into the cryostat insert. For magnetic property measurement, samples (thin film, powder or liquid) can be mounted onto a well-designed sample holder. Helium cooling system is sealed which minimizes the consumption of helium gas (constantly used for years). Only consumption of helium gas would be venting/flooding the chamber which may require replacement of helium gas tank every 1~2 months depending on the usage frequency.

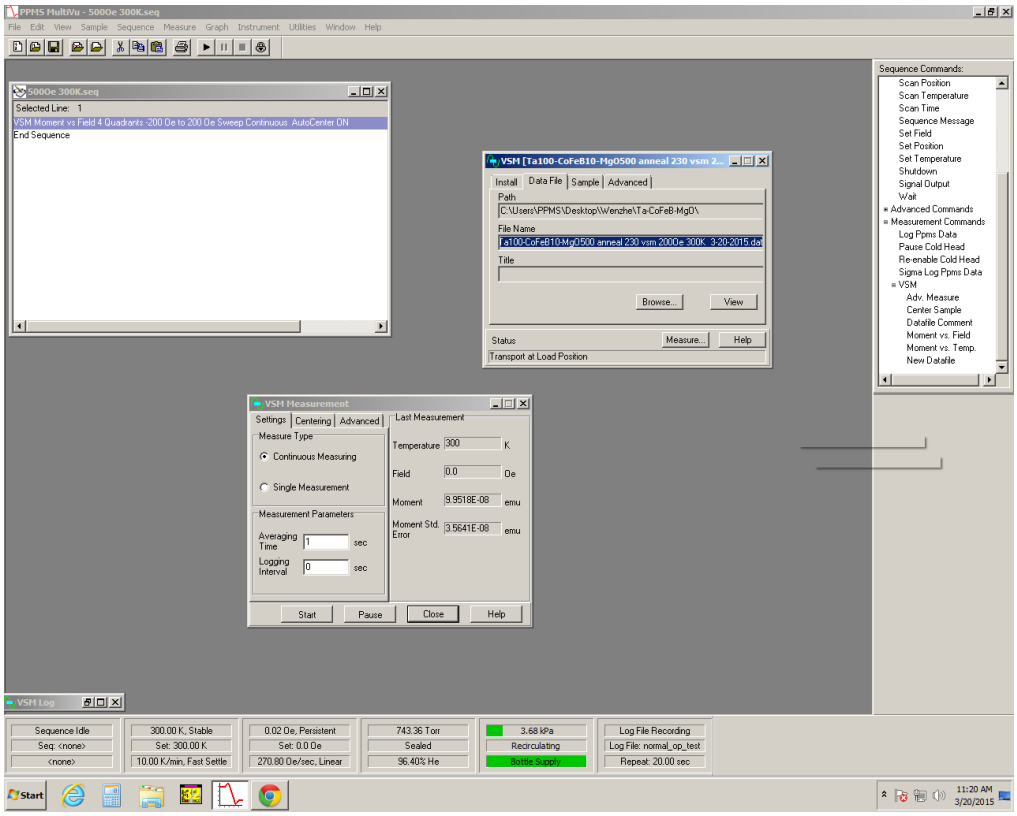

Fig. 2.12 The outlook of the PPMS control software

Selectable measurement modules are connected to the module tower that is then connected to the computer, making it more convenient to switch between different measurements. The controlling system can be controlled and monitor by computer through the ever-cool software (Fig 2.12).

At the bottom of the software, it displays the current status of the system, including pressure, temperature, magnetic field, Helium bottle supply, and sequence status. Double clicking any of the section will pop up dialog for further control. The unique feature of the software is the ability of building up customized sequence that takes actions in step according to the program. An example will be scanning temperature from 300K to 5K for every 50K while measuring the magnetic moment of a sample versus magnetic field from ±2T. The software will also display the current measurement data

and the system status in a log file. A log file is important for error (even quench) diagnoses and the file should be updated at least every other day.

2.5.2 Vibrating Sample Measurement

The vibrating sample measurement could be able to measure the magnetization of samples, in thin film, bulk, powder and liquids, under the magnetic field up to ±9 Tesla and in the temperature range of 2 K to 400 K.

The right part of Fig. 2.13 consists the major components to realize sample vibration and measurement. A sample is held in the sample tube and loaded to the coil position by the sample rod. The motion of the sample rod is driven by the linear motor transport that realizes the sample movement and vibration. The two cables connected between the control center and the measurement components are for controlling linear motor and data collection. The tower on the left of Fig. 2.13 is then connected to the computer for data process and control.

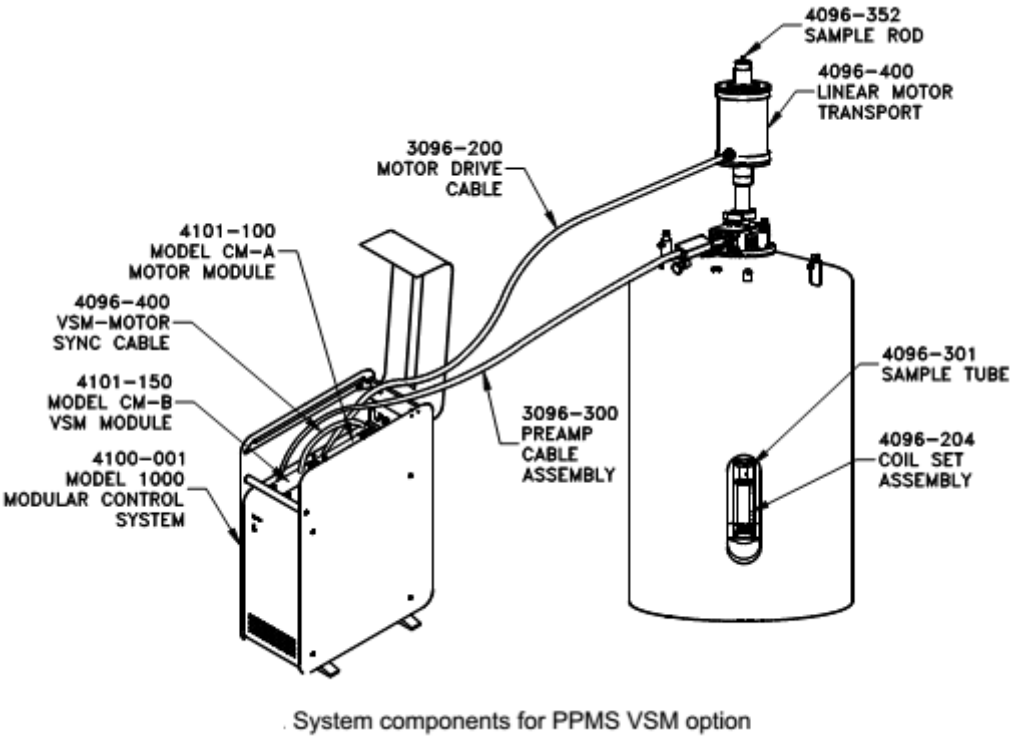

Fig. 2.13 Components for the VSM option

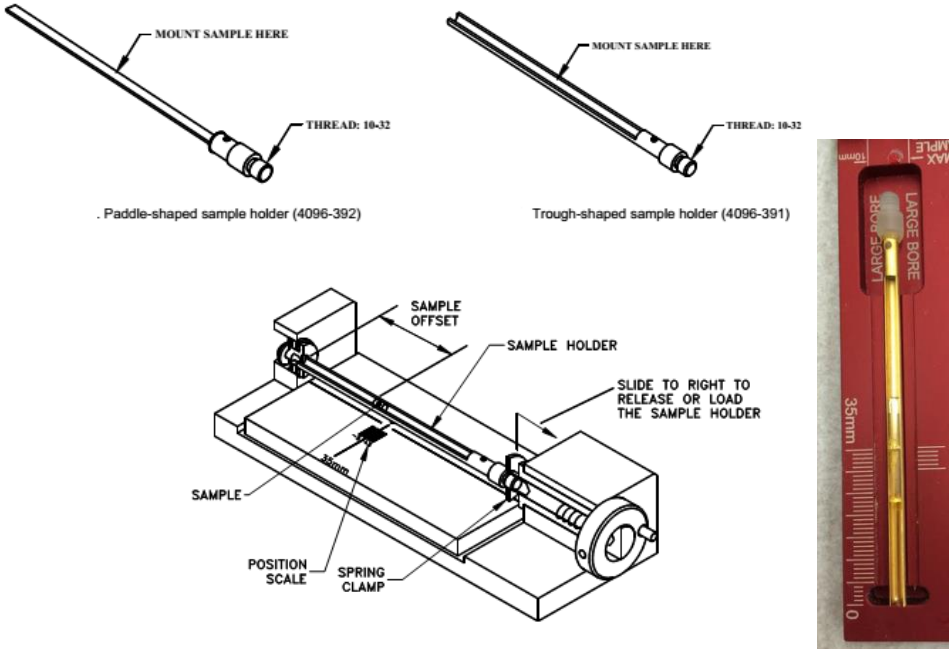

Fig. 2.14 VSM sample holder

For powder and liquid samples, the trough-shaped sample holder will be used. The sample will should be sealed in a capsule and locked in the holder by two cylindrical

quartzes. It will be slightly different for thin film sample, which has two orientations while taking the magnetic measurement, in the sample plane and perpendicular to the sample plane. For the in-plane measurement, the paddle-shaped sample holder should be used; for the perpendicular-to-plane orientation, the trough-shaped holder should be used with two quartzes holding the sample (Fig. 2.14). The center position of the sample should be as close as possible to the 35mm position scale. This is to ensure the sample to be placed in the middle of the magnetic field during measurement. A further position calibration will be done later after sample is loaded.

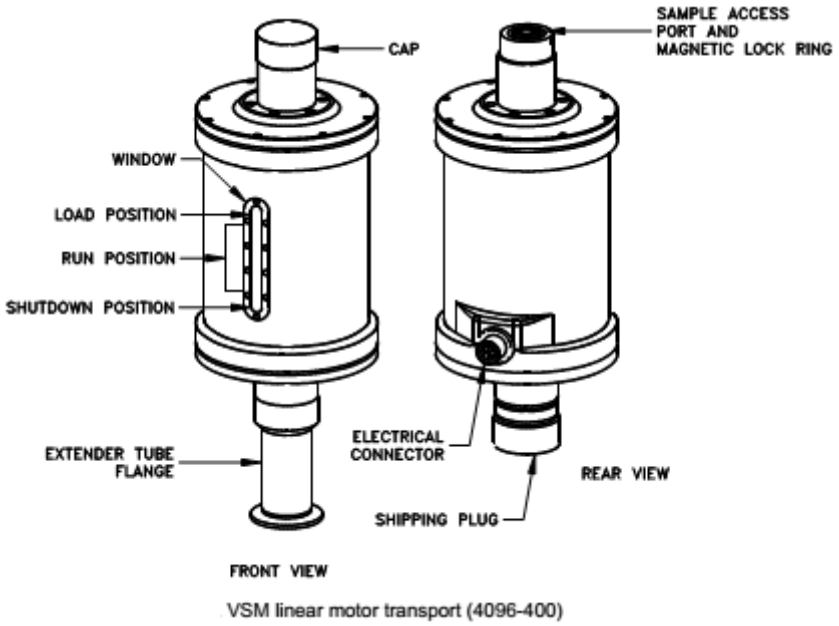

Fig. 2.15 Linear motor transport component

Before loading the sample, the VSM linear motor transport has to be mounted. Sample rod should be transported through the motor after opening the cap. Because there is no interlock between the cap and the system, it is important to make sure the chamber pressure is at atmosphere, the temperature is room temperature and the magnetic field is near zero before venting the chamber and loading or unloading samples. After the sample is loaded, the cap has to be put back on to cover the motor in order to isolate the system

(chamber) from atmosphere. If not, during the cooling down procedure, ice ball may form in the chamber and cause damage during sample vibrating.

After loading the sample, a sample position calibration should be conducted before the taking the VSM measurement. The determined position should be close to the preset 35 mm with reasonable offset. The position calibration procedure is taken by scanning the position of the sample in the full range while measurement the magnetic moment under a constant magnetic field, i.e. 0.5 Tesla. The position dependent signal is typically like the shown Fig 2.16.

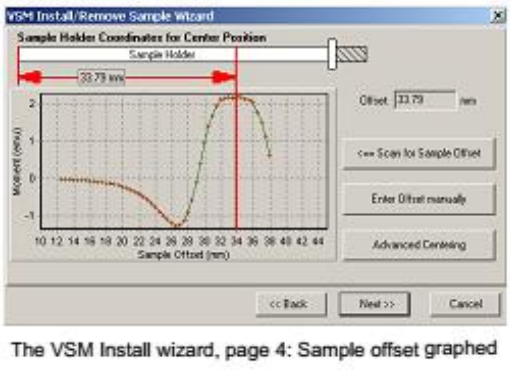

Fig. 2.16 Example of sample position calibration

Before a VSM measurement is taken, a calibration should be done using the provided cylindrical Pd material. For the calibration sample, the magnetic moment as a function the applied magnetic field should be similar to the curve in the following Figure 2.17. If a thin film ferromagnetic material is measured in the in-plane orientation, the magnetic moment signal might be very small (Fig. 2.18). It is recommended to measure the un-patterned thin film sample since the patterned structure often contained significantly reduced ferromagnetic materials, which may lead to small signal and large error. In order to extract the ferromagnetism signal (CoFeB in this example) from the raw

data, the tilted background, which is from the Si/SiO_2 substrate, should be subtracted (Fig. 2.19).

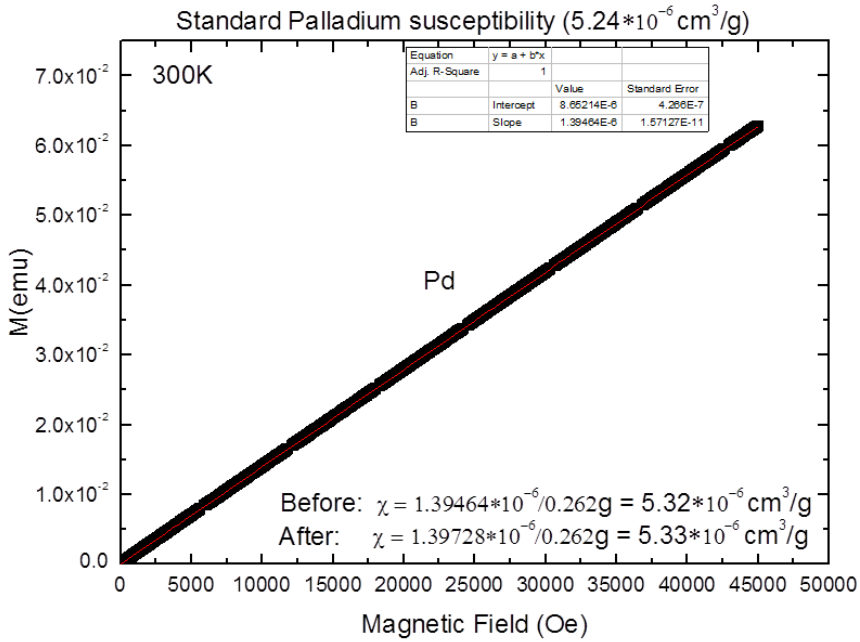

Fig. 2.17 VSM calibration using Pd

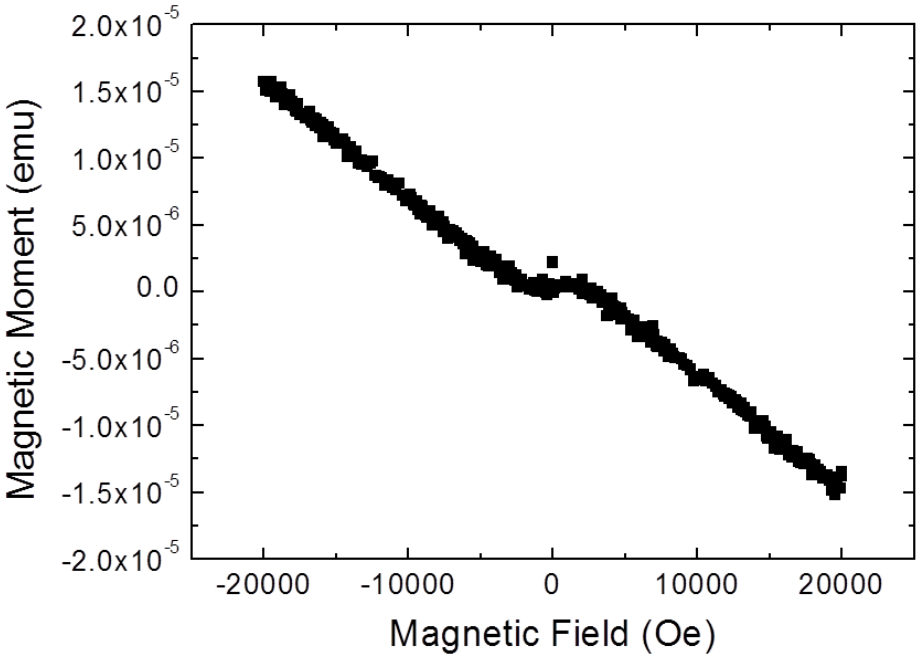

Fig. 2.18 The VSM result of Si/SiO2/Ta/CoFeB(1nm)/MgO multilayer

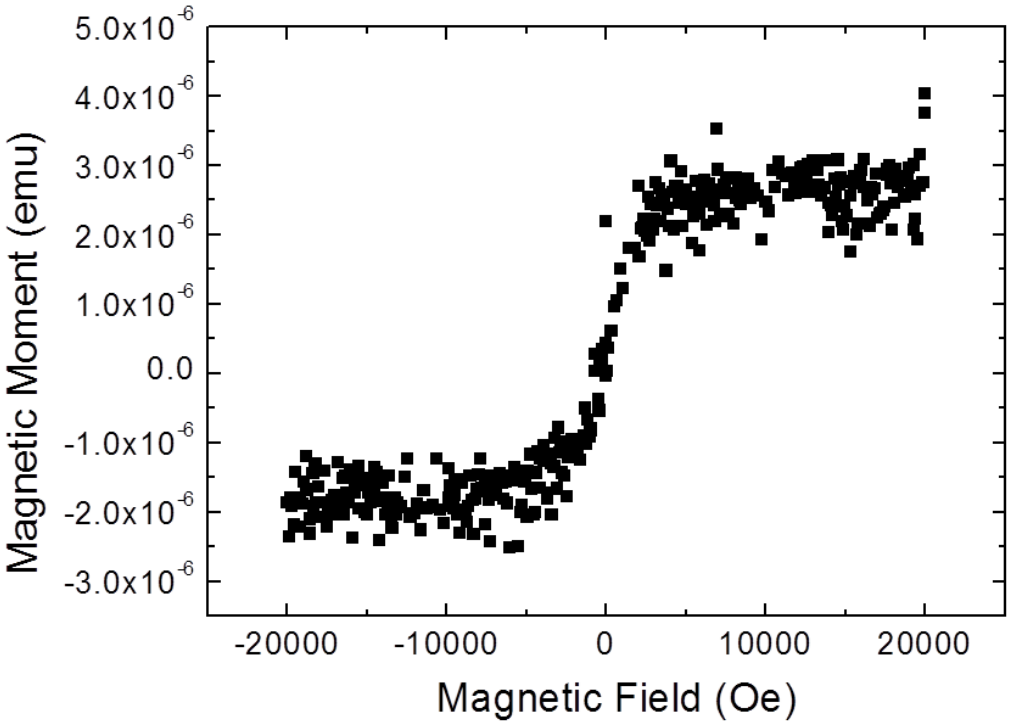

Fig. 2.19 The VSM result of Si/SiO2/Ta/CoFeB(1nm)/MgO multilayer after subtracting background.

The magnetic moment of the thin film divided by the volume of the ferromagnetic layer gives the corresponding magnetization verses magnetic field curve (Fig. 2.20). Because the thickness of the layer is determined by sputtering process, the measurement of the sample area becomes essential to derive the correct magnetization value. If the piece of the wafer has a regular shape, like rectangular, then the width and length can be measured by caliper to calculate the area. Alternatively, the area of the sample can be determined by measuring the weight of the sample and divided by the whole thickness of the stack. Since the Si takes more than 99% in terms of mass and volume, the mass divided by the density of Si is a good estimation of the volume of the wafer piece. Then the sample area can be determined since the thickness of the wafer piece is roughly the thickness of the Si substrate.

In the plots of magnetization versus magnetic field, the spontaneous magnetization could be extrapolated by extending the high field data to zero (y axis). The spontaneous magnetization is the net magnetization that exists inside a uniformly magnetized microscopic volume in the absence of an external magnetic field.

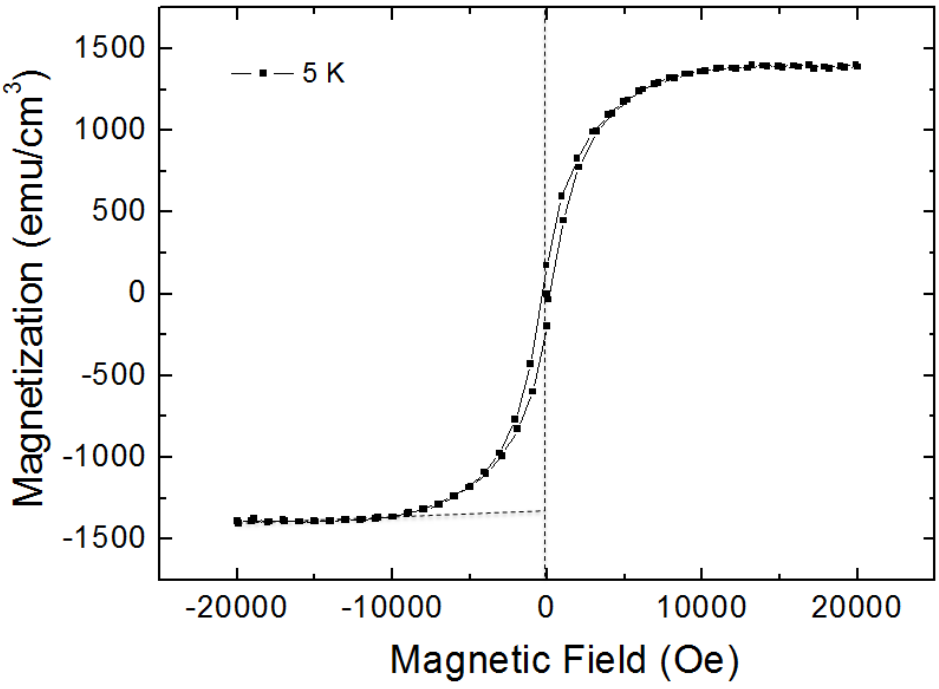

Fig. 2.20: Magnetization vs. magnetic field curve

The VSM technique is important to determine the spontaneous magnetization of the ferromagnetic thin layer in multilayer stack for Giant Spin Hall Effect and Anomalous Hall Effect study, which will be further discussed in details in Chapter 4, 5 and 6.

2.5.3 Magneto-transport measurement

The magneto-transport measurement in PPMS takes advantage of the various combinations between temperature and magnetic field. Besides, the system also has multiple options of measurement.

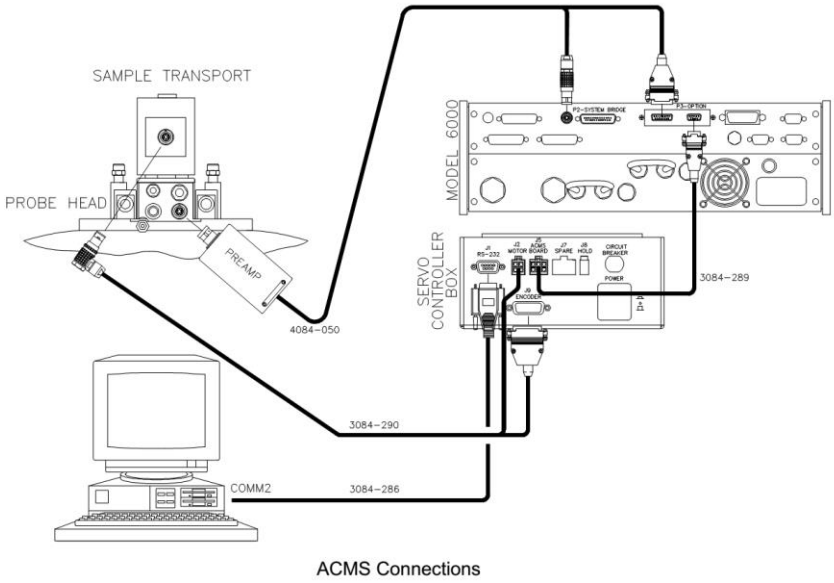

Fig. 2.21 The connection of the components (ACMS option)

If different options are chosen, the connection of the cables will be slightly different (Fig. 2.21, as an example of the cable connection in the ACMS option). However, it is quite convenient to switch between different measuring modules according to the diagram. For the most part of this work, the resistivity option (4 point) is sufficient for both Giant Spin Hall Effect and Anomalous Hall Effect measurements.

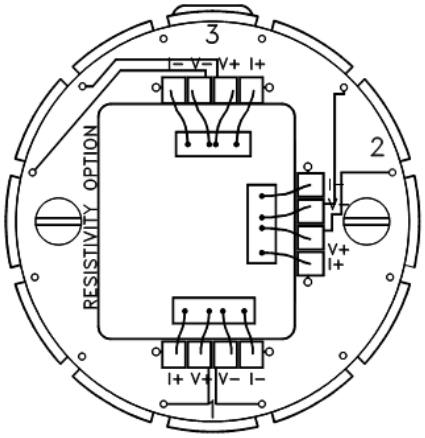

Fig. 2.22 Sample puck for resistivity option

For resistivity option, up to three thin film samples could be measured independently, i.e. Hall and resistivity measurement (Fig. 2.22). It should be noticed that

since the sample will be mounted on the surface of the sample puck and perpendicular to the fixed vertical magnetic field in the chamber, the transport measurement is normally perpendicular to the thin film sample plane using the provided puck. However, after some customized modification, in-plane magnetic field configuration can be done. One possible solution is shown in Fig. 2.23.

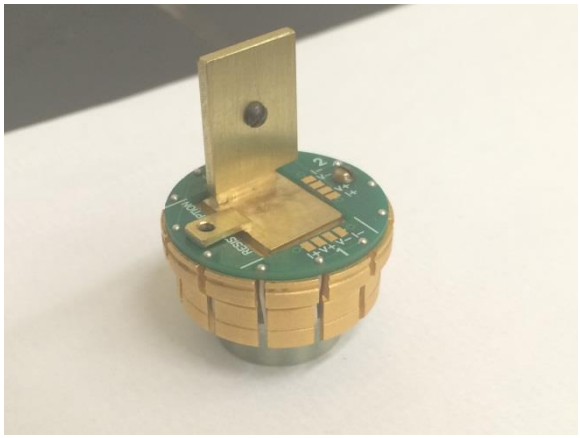

Fig. 2.23 Customized sample holder for in-plane thin film transport measurement

A thin film sample should be adhered to the sample puck surface using vacuum grease (Apiezon) during low temperature measurement. A double-sided tape (Scotch) should be used only for room temperature as it loses the adhesiveness at low temperature and the wires will pull up the wafer piece because of thermal contraction. After wire bonding procedure, connections should be checked on the test station using multi-meter.

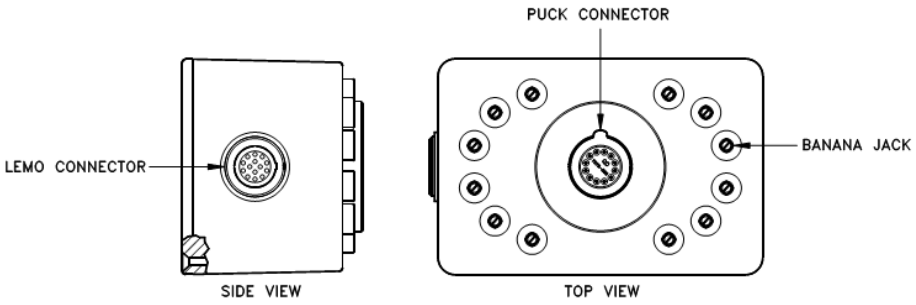

Fig. 2.24 PPMS Puck-wiring test station

The puck-wiring test station (Fig. 2.24) is used to verify the contact between a

sample and the puck. The test station contains three sets of contacts, all wired in series: a Lemo connector identical to the sample-chamber connector on the probe head, a puck connector, and 12 banana jacks. Different templates (for banana jack label) are available for different options.

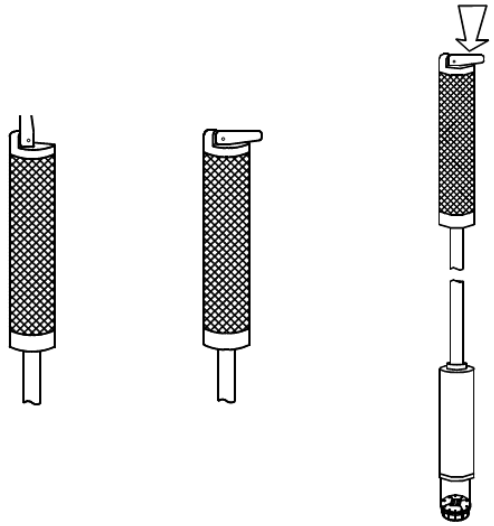

Fig. 2.25 The puck-insertion Tool

The long rod insertion tool (Fig. 2.25) is used to install the sample puck into the chamber, where the bottom has 12 pins for connection. The level of the tool is engaged when it is lying flat across the handle, and the tool grips the puck by a groove in its outer rim.

Before inserting the tool (with sample gripped) into the chamber, it should be double-checked in case the sample accidentally drops into the chamber, which will be extremely hard to get out. After inserting the tool into the chamber, slowly rotate the rod and feel the notch of the sample puck matches with the one in the chamber, which indicates that the sample puck is loaded in the right position. Then, withdraw the puck-insertion tool and close the chamber.

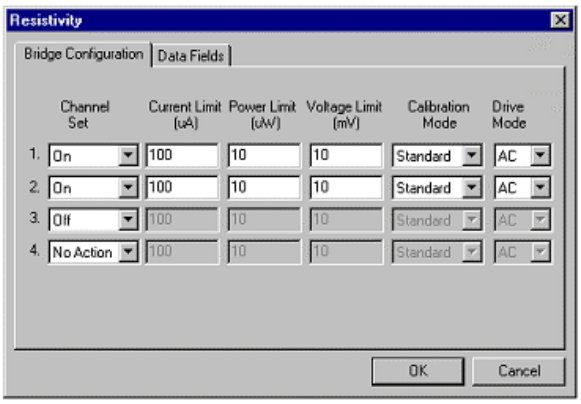

Fig. 2.26 Bridge configuration tab

Before starting a sequence of the transport measurement, there will be several bridge configuration settings that may require changes according to the sample parameters (Fig. 2.26). AC drive mode removes the offset from applying positive and negative currents. But under some circumstances, i.e. the Giant Spin Hall Effect measurement, DC drive mode should be utilized because the difference between positive and negative currents applied is not the offset between Hall bar leads but could be from spin torques in opposite directions (details will be in chapter 5).

Calibration mode could be chosen for coarse, standard or fine measurements. It takes 25 averages (and longer time) for the fine measurements. Sometimes, at different temperature, the resistance of the sample might be significantly different, which means the power/voltage limits should be changed accordingly. Such bridge configuration change is programmable and can be added into the sequence of the measurement.

After raw data is collected, it needs to be transformed into a csv file that can then be opened in Microsoft Excel. It should be mentioned that due to the magnetic remanence, i.e. a previous measurement was taken under a large magnetic field, then the low-field hysteresis loop might be off-centered. In order to remove the remnant magnetic

field before taking the low-field measurement, the magnetic field should be brought to 2~3 Tesla, and then set to 0 in an oscillating mode. However, if ultra-low field measurement is required (~10 Oe), a magnetic field calibration using the fluxgate probe should be conducted so that the remnant field is offset by sending a small current through a parallel coil close to the magnets in the system.

2.6 Low Frequency Noise Measurement

2.6.1 Introduction of Noise

The three types of noise that we are interested in are the Johnson noise, the shot noise and the 1/f noise. The Johnson noise is caused by thermally activated motions of charge carriers in a resistor and hence is temperature dependent. The expression of the noise power is

$$S_{Johnson}^{v} = 4k_B TR,$$

where k_B is the Boltzmann constant, T is the temperature, R is the resistance. Because the Johnson noise is frequency independent, it only contributes a constant background to the noise power spectrum. By using standard resistors, the Johnson noise measurement is also useful for system calibration.

The shot noise is from the stochastic nature of the transport mechanism in the presence of applied current, given by $S_{Shot}^{v} = 2eIR^2$, where e is the electron charge and I is the total charge current. The shot noise is also frequency independent and responses linearly to the amplitude of the applied current.

The 1/f noise is named due to its 1/f dependence of the noise power. Based on Hooge's law, the 1/f noise can be expressed as $S_{1/f}^{v} = \frac{\alpha}{Nf^{\gamma}}V^2$, where α is material-dependent constant, N is the total number of fluctuators, V is the applied voltage and γ is empirically determined to be between 0.9 to 1.4. Because of the small γ constant, the low frequency noise will be dominated by the 1/f noise.

A typical noise spectrum of a standard resistor is illustrated in Figure 2.27. The high-frequency peaks could be some picked up noises from background environment.

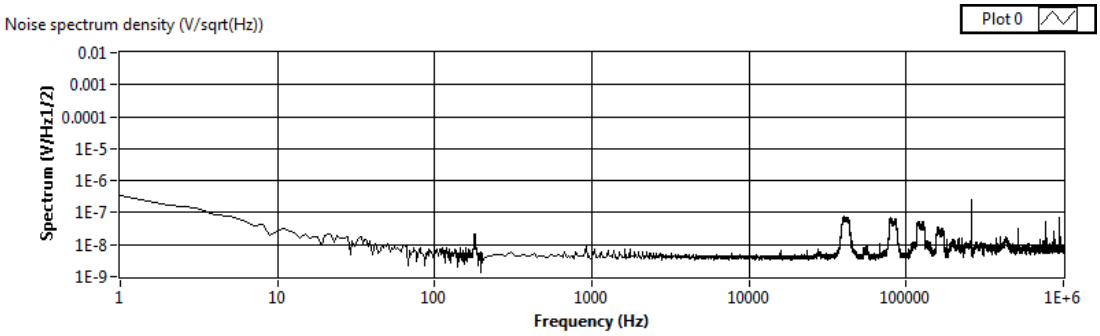

Fig. 2.27 Noise Spectrum Density of a standard resistor

2.6.2 The Schematic of noise measurement system

The noise measurement system is designed to automatically take the low frequency noise on external circuits, i.e. MTJ or Hall bar, and conduct simple analysis on the noise spectrum, i.e. the noise power and noise floor. The core of the system consists of the NI DAQ, the amplifier circuit and the software interface. The features of the system include self-calibration ability, automated bias voltage applied, and automatic battery charging. The schematic of this noise measurement system is shown in Fig. 2.28.

Different from the setup that uses spectrum analyzer (hardware module), this system bases on a data acquisition unit (NI DAQ) and a computer. The data acquisition

unit has a MHz sampling rate and the software deals with the large amount of collected data and performs data analysis and curve fitting.

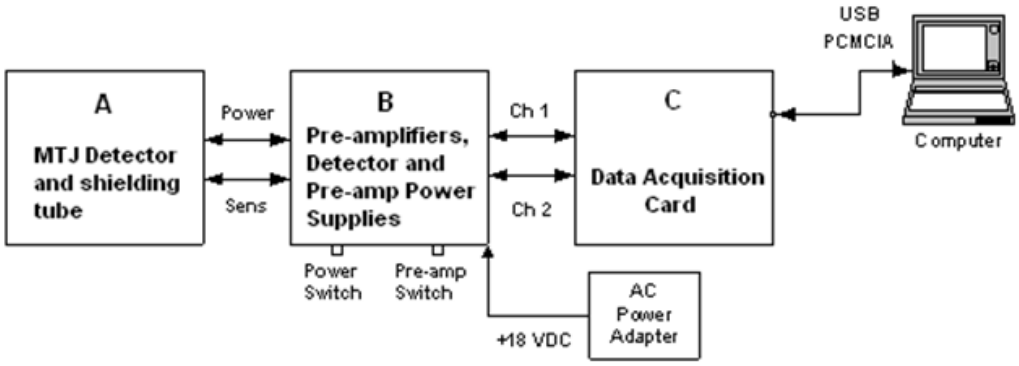

Fig.2.28 The schematic of the Low Frequency Noise Measurement System.

Before taking the measurement, a noise measurement system should be calibrated using a series of standard resistors. From the comparison between the Johnson noise of the standard resistors and the measured values, it can been that only when the load resistance (impedance) is within the range of 200 Ohm and 200,000 Ohm, the difference is within 10% and the measured results would be trustable if the load (measured circuit) is within this range. When the external load is lower than 200 Ohm, the Johnson noise is smaller than the DAQ resolution. If the external load is larger than 200,000 Ohm, the load impedance is comparable to that of the system (Fig. 2.29).

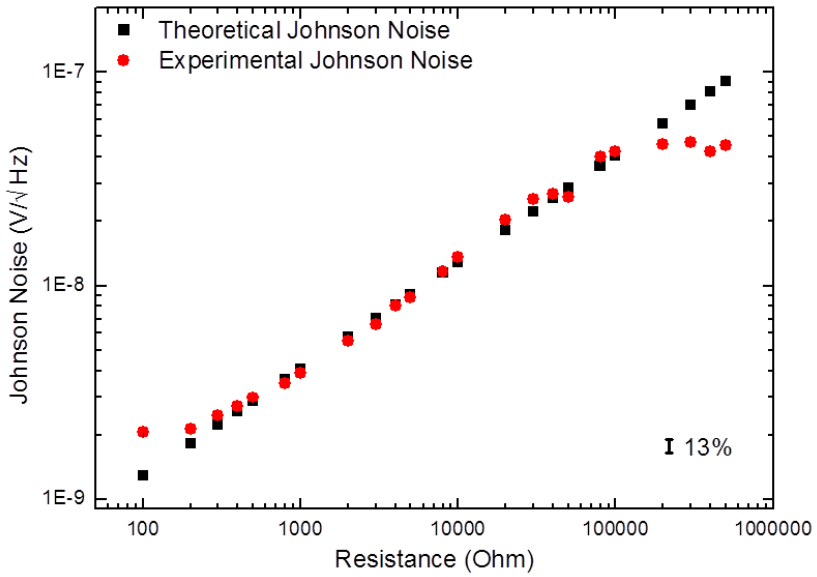

Fig 2.29 Comparison between measurement and standard resistor

It is worth noting that while taking measurement, changes of the circuits, i.e. changing bias voltage, turning on/off switches, will introduce spark signals that will be picked up by the system and will be amplified. This will lead to incorrect noise spectrum with abnormally large noise signal or overwhelming noise peaks. Therefore, it is important to wait for several seconds for the circuits to be stable before starting the noise measurement if the circuit was previously changed. Also, if the battery has low power, the gain of the amplifier will be different from the calibrated values and may lead to incorrect measurement results. Therefore, the low frequency noise measurement should only be taken when the battery are nearly full.

2.7 Summary

In this chapter, we described the experimental methods and techniques used for the fabrication of MTJ, including substrate oxidation, magnetron sputtering,

photolithography, ion beam etching, SiO_2 layer deposition (by sputtering), and gold contact deposition (by e-beam evaporation). We also introduced a short-loop fabrication process, which enables the quick measurement of MR ratios of partially patterned MTJ wafers. This process allows for continuous improvement on MTJ layered structures by reducing the development cycle by a factor of 3. Also, we covered the procedure of making thin-film Hall bar sensors using similar deposition and fabrication processes, and discussed the optimal procedures and conditions that produce high quality of thin-film alloy with different thicknesses and concentrations. In order to achieve beta phase Ta or W, minimizing the deposition heating is found to be critical. Also, it is discovered that the residual oxygen in the sputtering chamber is important for beta phase W deposition. In addition, the PPMS and noise measurement system enables us to conduct systematic measurements on the Giant Spin Hall Effect and Anomalous Hall Effect as further discussed in the following chapters.

Chapter 3

Theoretical Background

3.1 Introduction

This chapter describes the basics of Spin Hall Effect, Anomalous Hall Effect and Magnetic Tunneling Junction, which will be used for further discussion in the following chapters. The macrospin model [1, 2] is introduced for characterizing the Spin Hall Effect in a GSHE solids/Ferromagnetic bilayer structure. It is useful to calculate Spin Hall Angle and understand current-induced magnetization switching.

3.2 Spin Hall Effect and Anomalous Hall Effect

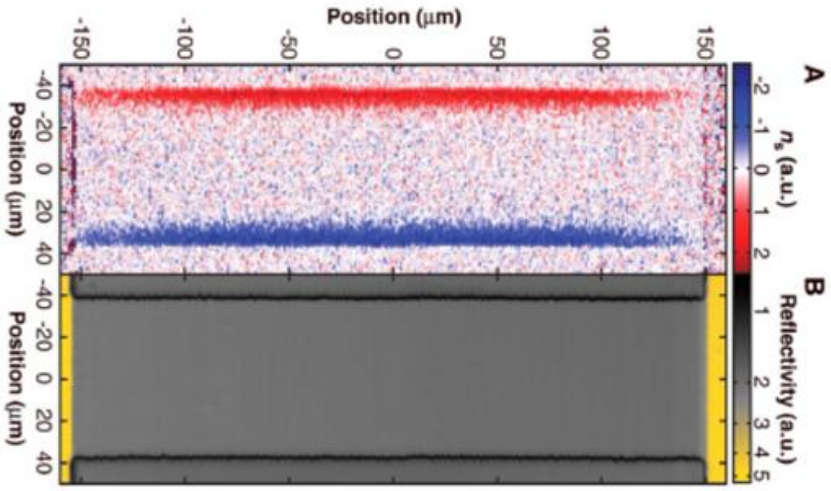

FIG 3.1: Two dimensional images of spin density (A) and reflectivity (B), respectively, in GaAs sample at 30 K. [3]

Spin Hall Effect (SHE) is a transport phenomenon consisting of the appearance of spin accumulation on the lateral surfaces of a sample carrying electric current. The opposing surface boundaries will have spins of opposite sign accumulated, and the flow of spins denotes the spin current. This phenomenon was observed as shown in Fig. 3.1, which illustrates an experimental result of a two-dimensional image showing opposite spin polarization localized at the two edges of the GaAs sample at 30 K [3]. In spite of its analogy to normal Hall Effect, SHE originates from the spin-orbit coupling in the solids. Therefore, no magnetic field is needed for SHE, and the solids can be non-magnetic.

The SHE can be parameterized by a spin Hall angle (SHA) θ_{SH}, which refers to the ratio of spin current density to the charge current density. To detect the SHE is not easy in traditional electric transport measurement though, as the spin separation in the non-magnetic solid does not lead to charge difference on the two sides of sample. Unlike normal Hall Effect, there is no measureable voltage difference in the SHE solid. One possible solution is to combine the SHE solid with a ferromagnetic layer or a magnetic tunnel junction as layered structure, so that the Anomalous Hall Effect or the Tunneling Magnetoresistance is utilized as a detector for SHE. The magnetization of this adjacent ferromagnetic layer can be rotated or switched by the spin torque (ST) from the spin current in the SHE solid, and the efficiency of this ST relates directly to the magnitude of the SHA [4].

Anomalous Hall Effect (AHE) exists in magnetic solids (ferromagnetic materials or paramagnetic materials in a magnetic field) due to spin-orbit interaction. It is analogous to SHE, and the spin separation leads to charge differences on the opposite sides of the sample because of the different densities of states between electrons with

opposite spins. The AHE, which depends directly on the magnetization of the material, is often much larger than the normal Hall effect [5]. Although it is a well-recognized phenomenon, there is still debate about its origins in the various materials. The AHE can be either an extrinsic effect due to spin-dependent scattering of the charge carriers or an intrinsic effect which can be described in terms of the Berry phase effect in the crystal momentum space (Fig. 3.2) [6-7].

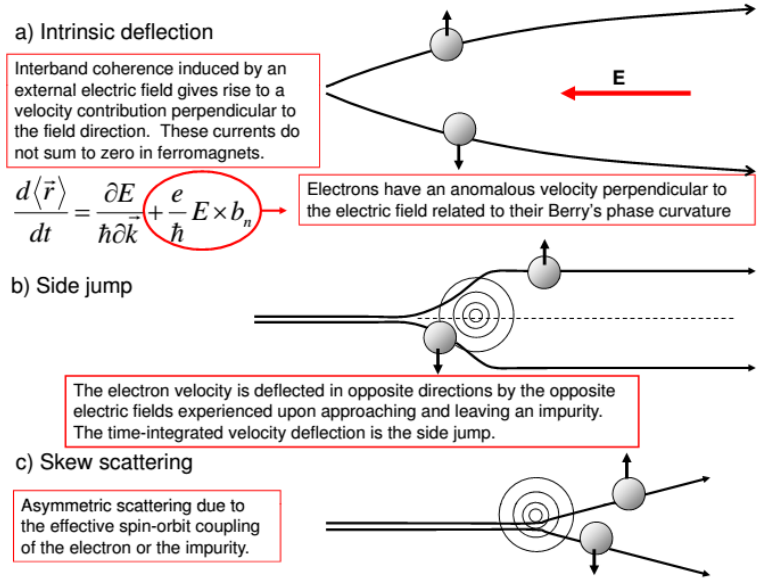

Fig.3.2 Illustration of the three main mechanisms that give rise to AHE [5]

In order to identify the underlying mechanism in a spin-orbit coupling system, a correlation between Hall resistivity (ρ_{xy}) or Hall Coefficient (R_S) and longitudinal resistivity (ρ) is experimentally studied, in a power law form ρ_{xy} $(or\ R_S) \sim \rho^{\beta}$. The skew scatter mechanism, which is asymmetric scattering from the impurities caused by the spin-orbit interaction (SOI), predicts that $\beta = 1$. On the other hand, the side-jump mechanism is independent of the density and strength of the scatters, yielding a relation of $\beta = 2$. In contrast to these two extrinsic mechanisms, the intrinsic mechanism

attributes to the Berry curvature, which can be understood as a magnetic field in the momentum space. The sum of Berry curvatures of all occupied states give rise to a sum of an extra velocity of these states, which then leads to an extra current (Hall current) [8]. Under this mechanism, the relation of $\beta = 2$ is satisfied. Therefore, experiments are conducted, on different systems, to explore this correlation in order to understand the dominating mechanism in the AHE.

3.3 Macrospin Model

In a simplified bilayer structure, the SHE in a non-magnetic solid (i.e. β-W) can be detected by the AHE on its adjacent ferromagnetic layer due to exerted spin-torque (ST). The equilibrium state of the magnetization is determined by the Landau-Lifshitz-Gilbert equation containing the Spin-Torque term and the Oersted field term:

$$\frac{d\hat{m}}{dt} = -\gamma\hat{m} \times \vec{H}_{eff} + \alpha\hat{m} \times \frac{d\hat{m}}{dt} + \gamma \frac{\hbar}{2e\mu_0 M_S t} J_S(\hat{m} \times \hat{\sigma} \times \hat{m}) - \gamma\hat{m} \times \vec{H}_{Oe} , \quad (3.1)$$

where m is the unit magnetic moment, γ is the gyromagnetic ratio, α is the Gilbert damping coefficient, μ_0 is the permeability in vacuum, M_S is the saturation magnetization of the ferromagnetic ($Co_{40}Fe_{40}B_{20}$) thin film, t is the thickness of the ferromagnetic thin film, J_S is the spin current density generated by the SHE solid (Ta), $\hat{\sigma}$ is the direction of the spin momentum, $\vec{H}_{Oe}$ is the Oersted field generated by the charge current, $\vec{H}_{eff}$ is the sum of external magnetic field $\vec{H}_{ext}$ and anisotropy field $\vec{H}_{an}$:

$$\vec{B}_{eff} = \vec{B}_{an} + \vec{B}_{ext} . \quad (3.2)$$

In the equilibrium state, Eq. (3.1) can be simplified to

$$0 = -\hat{m} \times (\vec{B}_{an} + \vec{B}_{ext} + \vec{B}_{Oe}) + \frac{\hbar}{2eM_S t} J_S(\hat{m} \times \hat{\sigma} \times \hat{m}) . \quad (3.3)$$

This equation can be further simplified by only consider the torque in y direction, as shown in Fig. 3.3, by sending the charge current in x direction and constraining external magnetic field $\vec{B}_{ext}$ in the x-z plane. Also, The magnitude of $\vec{B}_{Oe}$ can be estimated in this bilayer structure by

$$\left|\vec{B}_{Oe}\right| = J_C \frac{\mu_0 d}{2} \sim \left(\frac{3.2\times10^{-2} mT}{1\times10^{6}\frac{A}{cm^2}}\right) \times J_C. \tag{3.4}$$

If compared to the spin torque term, which is about $\left(\frac{3\times10^{-1} mT}{1\times10^{6}\frac{A}{cm^2}}\right) \times J_C$, the Oersted field is one order of magnitude smaller than the spin torque term (in the Ta/CoFeB/MgO structure), and hence can also be eliminated for simplicity.

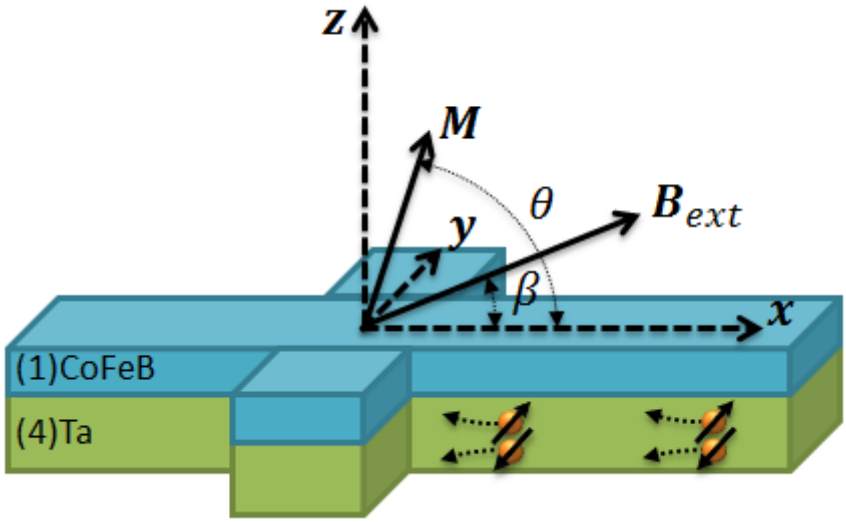

Fig. 3.3 Schematic drawing of the (4 nm)Ta/(1 nm)CoFeB bilayer structure.

Also, in the x-z plane, $\vec{B}_{an}$ can be expressed by

$$\vec{B}_{an} = -B_{an}^{0}(\hat{m} - m_z\hat{z}) = B_{an}^{0} cos\theta \hat{z}\,, \tag{3.5}$$

where B_{an}^{0} is the perpendicular magnetic anisotropy field [1]. Then, Eq (3.3) can be further simplified to

$$0 = \hat{y} \cdot [-\hat{m} \times (B_{an}^{0} cos\theta \hat{z} + \vec{B}_{ext}) + \frac{\hbar}{2eM_{S}t} J_S(\hat{m} \times \hat{\sigma} \times \hat{m})], \qquad (3.6)$$

which is

$$0 = -B_{an}^{0} \sin\theta cos\theta + B_{ext} \sin(\theta - \beta) + \frac{\hbar}{2eM_{S}t} J_S. \qquad (3.7)$$

Eq (3.7) will be used to determine the perpendicular magnetic anisotropy B_{an}^{0} and the current density J_S in chapter 4 and 5. The latter value is used to calculate spin Hall angle by $\theta_{SH} = {J_S}/{J_C}$.

3.4 Tunnel magnetoresistive (TMR) effect

In 1975, the French physicist Julliere [9] discovered the tunneling magnetoresistance (TMR) effect when he measured an MR ratio of 14% at 4.2 K in a Fe/Ge-O/Co MTJ stack. As seen in Figure 3.4, the tunneling resistance of the junction, which consists of two ferromagnetic electrodes separated by a thin insulator, is lower when the magnetizations of the two electrodes are parallel (Fig. 3.4 a) than when the magnetizations are antiparallel (Fig. 3.4 b). The size of resistance change is measured by $MR = \frac{R_{ap} - R_p}{R_p}$, which is called the magnetoresistance (MR) ratio.

In 2004, Parkin et al. at IBM [10] and Yuasa et al. at AIST Japan [11] independently reported giant Tunneling MR (close to 200% at RT) effects in MgO-based MTJs fabricated by sputtering and molecular beam epitaxial (MBE) methods, respectively. This TMR number reaches 600% at room temperature and 1100% at 4.2 K in 2008[12]. The huge TMR effect in MgO-based MTJs has propelled a surge in research of spintronics and MTJs.

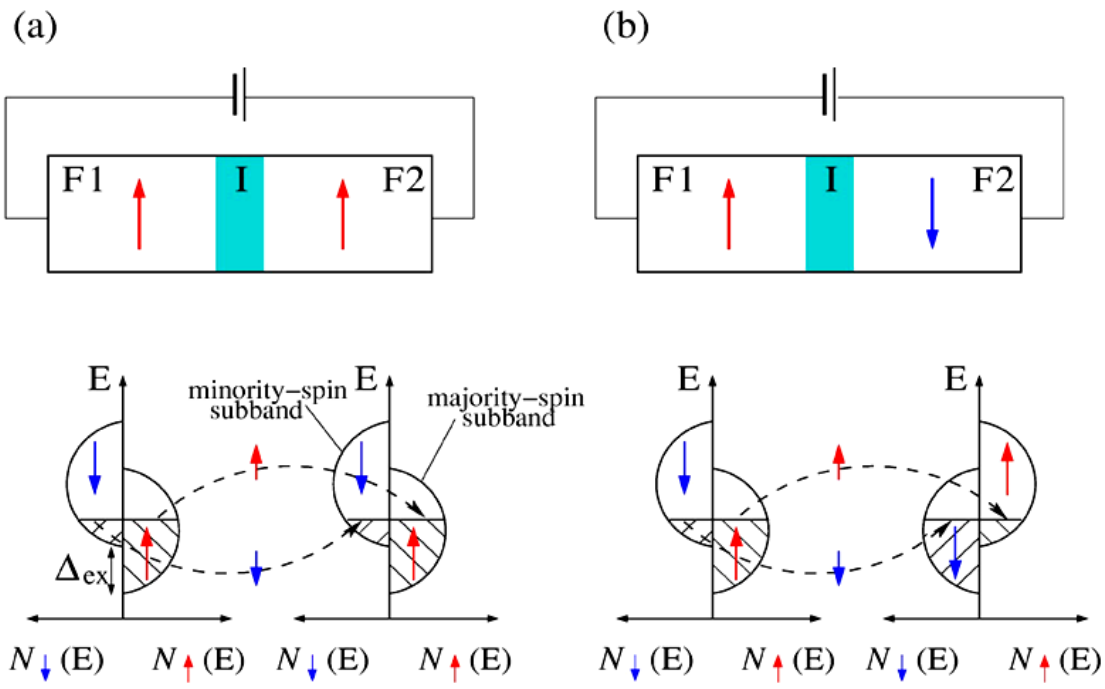

Fig. 3.4 Schematic of Tunneling Magnetoresistance: when the polarizations of two ferromagnetic layers (separated by an insulator) are parallel (a) or antiparallel (b), it exhibits lower or higher resistance.

In a simple model proposed by Julliere, the TMR effect is due to spin-dependent tunneling [9], and the tunneling current of spin-up and spin-down electrons are considered two independent processes. According to this model, the MR ratio can be expressed in terms of the spin polarization P of two ferromagnetic electrodes

$$MR = 2P_1P_2/(1 - P_1P_2)\,, \tag{3.8}$$

where

$$P_\alpha = (D_{\alpha\uparrow} - D_{\alpha\downarrow})/(D_{\alpha\uparrow} + D_{\alpha\downarrow})\ . \tag{3.9}$$

Here P_α is the spin polarization of a ferromagnetic electrode (α=1 or 2), and $D_{\alpha\uparrow}$ and $D_{\alpha\downarrow}$ are the densities of states (DOS) of the electrode at the Fermi energy (EF) for the majority-spin and minority-spin bands, as shown in Figure 3.4. For instance, the spin polarizations of 3d ferromagnetic metals and alloys made of iron (Fe), nickel (Ni), and cobalt (Co) are found to be in the range from 0 and 0.6 below 4.2 K [13-14]. These measured spin polarization values can be substituted into Eq. 3.8 to estimate the

theoretical MR ratios, which agree well with the experimental MR values in the MTJ systems.

According to the Julliere's model, an MR ratio of about 70% at RT is close to the limit for the 3d ferromagnetic-alloy electrodes. Thermal spin fluctuation at finite temperature would reduce the spin polarization, thus the MR values would decrease with rising temperatures according to Eq. 3.8. In order to achieve significantly large MR ratio (greater than 70%) at room temperature, scientists turned their attention to a new class of ferromagnetic materials, also known as half metals. The spin polarization in such metals is close to one, and the ferromagnetic layers fabricated by half metals may produce an infinite MR ratio based on first principle calculations. Such studies have been done in different MTJ systems at low temperature but improvements at room temperature are still needed [15-16].

3.5 Summary

The theories in this chapter will be utilized in the experimental research in the following chapters. The macrospin model is important to quantitatively determine the spin Hall angle and spin transfer torque. Also, since the anomalous Hall effect could be due to different mechanisms, including skew scattering, side-jump and intrinsic mechanism, the experimental study in Fe-Pt alloy will tend to reveal the mechanism and may provide better understanding in the underlying physics in such high spin-orbit-coupling system. The MgO-based Magnetic Tunneling Junction has the promising performance in both magnetic field sensing and memory applications due to the large tunnel magnetoresistance. A combination of the Giant Spin Hall Effect and Magnetic

Tunneling Junction will be even more promising in the application of future STT-MRAM which features much lower switching current density and hence lower power consumption.

References

1. L. Liu, O. J. Lee, T. J. Gudmundsen, D. C. Ralph, and R. A. Buhrman, Phys. Rev. Lett. **109**, 096602 (2012)
2. Q. Hao and G. Xiao, Phys. Rev. Appl. 3, 034009 (2015)
3. Y.K. Kato, R.C. Myers, A.C. Gossard, and D.D. Awschalom, Science **306**, 1910 (2004).
4. L. Liu, T. Moriyama, D. C. Ralph, and R. A. Buhrman, Phys. Rev. Lett. **106**, 036601 (2011).
5. R. Karplus and J. M. Luttinger Phys. Rev. **95**, 1154 (1954)
6. N. Naoto, J. Sinova, S. Onoda, A. H. MacDonald and N. P. Ong., Reviews of Modern Physics **82**, 1539 (2010)
7. M. V.Berry, Proceedings of the Royal Society A **392**, 45 (1984)
8. A. MacDonald and Q. Niu, Phys. World **17,** 18 (2004)
9. M. Julliere, Phys. Lett. **54A**, 225 (1975).
10. S. S. P. Parkin et al., Nat. Mat. **3** (12), 862 (2004)
11. S. Yuasa, T. Nagahama, A. Fukushima, Y. Suzuki, and K. Ando, Nat. Mat. **3**, 868 (2004)
12. S. Ikeda, J. Hayakawa, Y. Ashizawa, Y.M. Lee, K. Miura, H. Hasegawa, M.

Tsunoda, F. Matsukura and H. Ohno, Appl. Phys. Lett. **93**, 082508 (2008)

13. R. Meservey and P. M. Tedrow. Phys. Rep. **238**,173 (1994).
14. S. Parkin, X. Jiang, C. Kaiser, A. Panchula, K. Roche, and M. Samant. Proc. IEEE, **91**, 661 (2003).
15. M. Bowen, M. Bibes, A. Barthelemy, J.-P. Contour, A. Anane, Y. Lemaitre, and A. Fert. Appl. Phys. Lett., **82**, 233 (2003).
16. Y. Sakuraba, M. Hattori, M. Oogane, Y. Ando, H. Kato, A. Sakuma, T. Miyazaki, and H. Kubota, Appl. Phys. Lett., **88**,192508 (2006).

Chapter 4

Beta tungsten thin films- structure, electron transport and giant spin Hall effect

4.1 Introduction

Highly resistive beta (β) tungsten characterized by a large spin-orbit coupling (SOC) exhibits giant spin Hall effect (GSHE) [1-3]. Its spin Hall angle approaches 0.40 [3], the largest among transition elements, and it converts charge current into spin current efficiently [3]. Robust perpendicular magnetic anisotropy (PMA) has been realized in a layer structure combining the elusive, metastable β-W and a $Co_{40}Fe_{40}B_{20}$ thin film [3]. The GSHE yields, after suitable thermal magnetic annealing, a very low critical current density for magnetization switching [3]. However, fabricating β-W films is challenging. Although W metallization process is used for the very-large-scale-integrated (VLSI) circuits, it is the stable and conductive α-W phase that meets the requirement of semiconductor processing [4]. Tomorrow's spintronic MRAM [5] and spin-logic devices [6] could increasingly rely on the newly discovered GSHE in β-W films. It is, therefore, imperative to understand the properties and fabrication of the β-W solid. To date, much effort has been made to stabilize the β-W phase [4, 7-15]. Nevertheless, very little work is available on the β-W solid in the context of GSHE [1-3] and on its basic properties.

4.2 Experimental

In this work, we prepare a series of β-W thin films with a broad range of thickness (3.0-26.7 nm) using a simple magnetron sputtering process. Based on the process, we achieve PMA and a large spin Hall angle (0.40) [3] in the bulk β-W in a structure of β-W/ $Co_{40}Fe_{40}B_{20}$ /MgO. We examine the effect of thermal annealing on the structure of the W films. We find that the metastable β-W and β-W/$Co_{40}Fe_{40}B_{20}$/MgO structures can be easily fabricated, making them technologically promising. We measure the temperature dependence of resistivity and normal Hall effect of the β-W films down to the lowest temperature of 10 K. These basic properties of β-W are elucidating in the understanding of this large SOC solid.

We prepare the W films on thermally oxidized Si wafers under ambient conditions using a homemade high vacuum magnetron sputtering system equipped with a cryopump. The face-up sputtering guns have a diameter of 5 cm and use an NdFeB permanent magnet ring. The target-substrate distance is 9 cm. The face-down substrates are thermally oxidized single crystal Si wafers (5-cm diameter), which rotate at about 50 rpm during deposition for achieving thickness uniformity. The off-center distance is 3 cm between the center of a substrate and that of a target. The base pressure is less than 2×10^{-8} Torr and the Ar sputtering pressure is ~2.2 mTorr. For the formation of β-W, we apply a low dc sputtering power of only 3W intermittently to keep a low deposition rate of 0.02 nm/s. The films are patterned using photolithography into standard Hall bars for both Hall effect and resistivity measurements, with longitudinal dimensions of 20×55 μm^2 in area. In addition to these as-deposited samples, we also prepare a corresponding set of

samples that are annealed at 280°C for 1 min with 2 h of ramping up and 6 h of natural cooling in vacuum (1×10^{-6} Torr) and under a perpendicular magnetic field (0.45 T) to the films. We used the Quantum Design Physical Property Measurement System to measure resistivity and Hall effect as functions of temperature between 10 K and 360 K. The Bruker D8 Discover X-ray Diffraction (XRD) System is used for structural measurement.

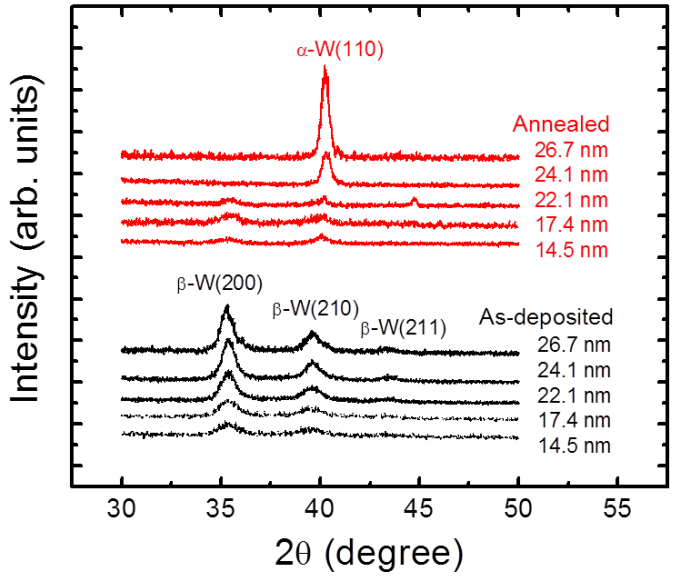

Fig. 4.1. θ - 2θ x-ray diffraction patterns for as-deposited and annealed W thin films with various thicknesses

Figure 4.1 shows the XRD patterns for the as-deposited and the annealed W films with thickness in the range of 14.5 to 26.7 nm. All as-deposited films have single phase β-W, which is an A_3B solid with the $A15$ type crystal strcuture. The annealed films remain in the β-W phase up to a critical thickness (t_c) of 22.1 nm. Above 22.1 nm, films are transformed into the α-W phase, which has the bcc crystal structure. For β-W films, we calculate the average lattice constant based on the (200), (210), and (211) peaks. For α-W films, the lattice constant is obtained from the (110) peak. Figure 4.2(a) shows the lattice constant as a function of film thickness, which reveals clearly the effect of

annealing. Up to the largest thickness of 26.7 nm, the lattice constant of the as-deposited β-W films remains unchanged. However, post-annealing and beyond t_c, the lattice constant becomes that of the α structure. Therefore, if the GSHE of β-W is intended for spintronic devices which typically require magnetic thermal annealing, the actual thickness of the β-W film must be smaller than t_c. We note that the spin diffusion length (λ_{sf}) in β-W film [3] is 3.5 nm, which is much smaller t_c. Therefore the full strength of the GSHE of β-W film can be exploited as long as thickness is less than t_c, but larger than λ_{sf}.

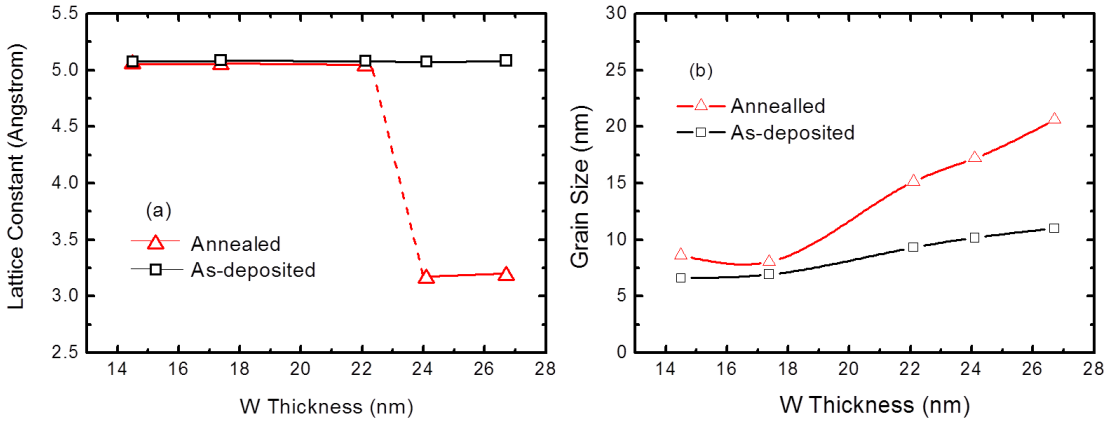

Fig. 4.2. (a) Lattice constant determined from x-ray diffraction as a function of W film thickness for as-deposited and annealed samples; (b) Grain size determined by using the Scherrer equation (see text) as a function of W film thickness.

XRD data provides us with an estimate on the size of crystallites, or grain size. According to the Scherrer equation[16], which relates the grain size to the broadening of a diffraction peak, the average grain size is given by $K\lambda/\beta\cos\theta$, where K is a shape factor (typically about 0.9), λ is the X-ray wavelength, β is the width of a diffraction peak at half maximum intensity, and θ is the Bragg angle. The Scherrer equation remains valid to the extent that the peak broadening is primarily due to the grain size rather than other

inhomogeneities. Based on our XRD data, we obtain the grain size estimated using the Scherrer equation, as shown in Fig. 4.2(b) as a function of W film thickness for the as-deposited and the annealed samples. In both cases, the grain size is smaller than, but increases with, the film thickness. Annealing increases the grain size by about 50 to 70%. It is noted the grain size in all samples is much larger (by a factor of 2 to 4) than the λ_{sf} =3.5 nm in β-W [3]. Therefore, λ_{sf} is not predominantly affected by the gain size, but is more dependent on the local structures within the β-W crystallites (such as atomic and lattice disorders).

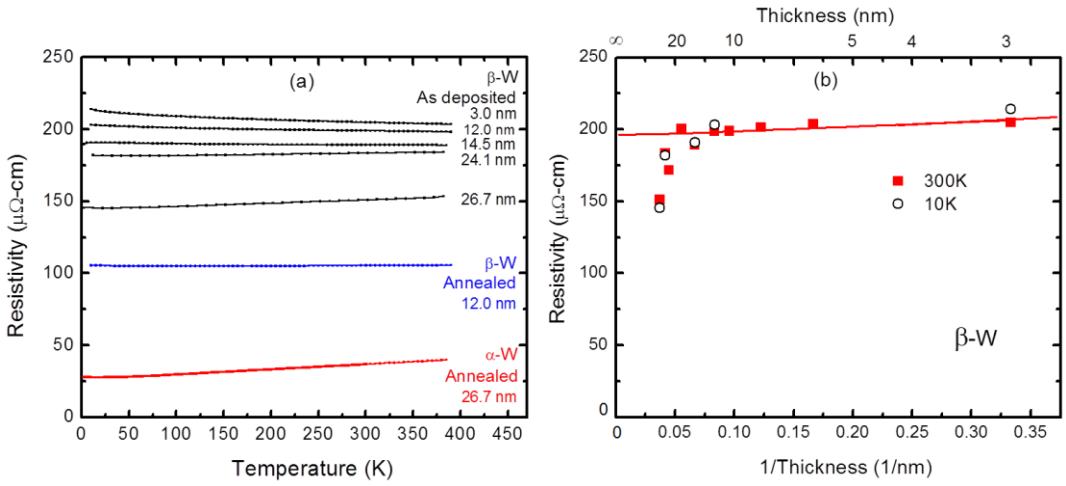

FIG. 4.3. (a) Temperature dependence of resistivity for β-W and α-W thin films between 10 K and 380 K; (b) Resistivities at 300 K and 10 K versus inverse film thickness (1/*t*) for β-W films (3.0 nm – 26.7 nm). The solid straight line is the theoretical fit using Eq. (1) within 3.0 nm and 22.1 nm based on the finite-size effect of thin film resistivity.

Next, we focus on the electron transport properties of the films. Figure 4.3(a) shows the resistivities of the W films as functions of temperature (T = 5 K to 380 K). The as-deposited β-W films (3.0 to 24.1 nm) are characterized by very large resistivities of 183.5 to 204.8 μΩ-cm at 300 K. Also noteworthy is that the temperature coefficient of

resistivity, $(1/\rho)\Delta\rho/\Delta T$, is very small for the β-W films over the whole T range. For example, for the 14.5 nm-thick β-W film, its resistivity remains nearly constant (variation less than 1%) at 190.0 μΩ-cm from 5 K to 380 K. This property is advantageous if β-W is used to generate spin current based on the GSHE. It would mean that the magnetic switching power will not depend on T, hence, providing a wide T range of operation for the spintronic devices.

For a continuous thin film with a thickness t much larger than the effective electron mean free path λ_{eff}, the thin film resistivity can be expressed as [17]

$$\rho(t) = \rho_B + \frac{3}{8}\rho_B\lambda_{eff}/t\,, \tag{4.1}$$

where ρ_B is the bulk resistivity. Figure 4.3(b) shows the resistivities of the β-W thin films versus the inverse thickness ($1/t$). Within the range of 3.0 to 22.1 nm, Eq. (1) can fit the resistivity data marginally. From the fit, we obtain that ρ_B(300 K)≈195±3 μΩ-cm and λ_{eff} (300 K) ≈ 0.45±0.26 nm, ρ_B(10 K) ≈192±8 μΩ-cm and λ_{eff}(10 K) ≈ 0.95±0.52 nm for the bulk β-W film. The thermally induced resistivity, $\Delta\rho = \rho_B(300\text{ K}) - \rho_B(10\text{ K}) < 9$ μΩ-cm, is insignificant, indicating that the electron-phonon inelastic scattering is relatively weak compared with the disordered elastic scattering. We note that the ρ_B(300 K) ≈ 5.33 μΩ-cm for the pure α-W bulk solid [18], which is much smaller than resistivities of any of our β-W thin films. The value λ_{eff} is much smaller than the thickness and the grain size of the film by a factor of 5 to 10. Therefore, the finite-size effect and the grain boundary scattering are not sufficient to account for the large resistivity of the β-W film. It has been suggested that β-W phase is probably stabilized by small amounts of oxygen [4, 15]. Further work, particularly theoretical study, is needed to evaluate whether small

amounts of oxygen is responsible for electron disordered scattering either from charge-dependent impurity scattering or spin-orbit scattering. Judging from the large spin Hall angle observed in β-W films [1-3], we conjecture that the disordered spin-orbit scattering plays a significant role in the resistivity of the β-W films. Above 22.1 nm, as shown in Fig. 4.3(b), the resistivities drop significantly from Eq. (4.1). We believe that these thicker films may have a small mixture of α-W phase, which has a much smaller resistivity than β-W phase. For the annealed films, we observe that resistivity remains large (100-260 μΩ-cm) for films that remain β-W phase.

We note that, when the thickness of β-W is smaller than 14.5 nm, the resistivity of the films is slightly larger at 10 K than at 300 K. This behavior indicates the appearance of a weakly thermally activated electron transport, complicating any analysis on the electron-phonon contribution. Also, in the thin-film limit, e.g., ~3 nm, the thickness is not much larger than the extracted λ_{eff}, and the validity of Eq. (4.1) is weakened. Therefore, the λ_{eff} value is somewhat uncertain in the thin-film limit.

After annealing, the 24.1 nm and 26.7 nm films are transformed into the α-W phase. We found that ρ(300 K) ≈ 36.7 μΩ-cm and ρ(10 K) ≈ 27.7 μΩ-cm for the 26.7 nm-thick α-W thin film. Comparing with β-W, the resistivity of the α-W phase is much more dependent on temperature. For example, in the 26.7 nm-thick α-W film, the thermally induced resistivity, $\Delta\rho = \rho_B(300\text{ K}) - \rho_B(10\text{ K}) \approx 9.0$ μΩ-cm, indicating a significant contribution from the electron-phonon scattering.

We have also measured the Hall effect which is an integral part of the electron transport of a metal. An investigation of both the resistivity and Hall effect and their temperature dependence provides insight into the β-W solid with a strong SOC. Figure

4.4 shows the temperature dependence of the Hall effect of the β-W and α-W thin films. The Hall coefficent for β-W thin film is R_H(300K) = -1.62×10^{-8} Ω-cm/T = -1.62×10^{-10} m^3/C. R_H(T) always carries a negative sign, and is linearly dependent on T between 10 K

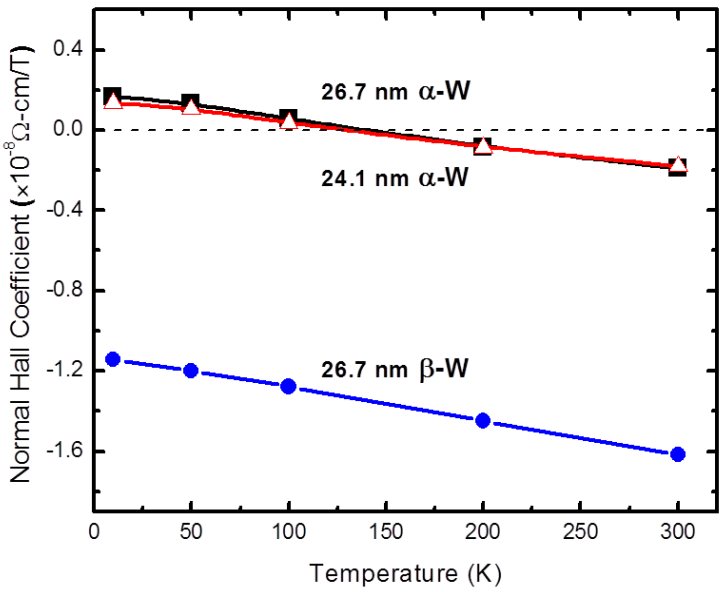

Fig. 4.4 Temperature dependence of normal Hall coefficient of β-W (26.7 nm) and α-W (24.1 nm and 26.7 nm). Normal Hall effect is measured between -5 T and +5 T. Note the sign change at about 130 K for α-W.

and 300K. At 10 K, the magnitude of R_H(10 K) (-1.14×10^{-8} Ω-cm/T) is reduced by 30% from the room temperature value. Overall, the charge carriers are predominantly electrons in the β-W thin film. For α-W thin films, R_H(300K) is -1.91×10^{-9} Ω-cm/T = -1.91×10^{-11} m^3/C, consistent with literature[19]. It carries a negative sign and is about 5 times smaller than the bulk value (R_H(300K) = $+8.6\times10^{-11}$ to $+11.8\times10^{-11}$ m^3/C) [18, 20]. $R_H(T)$ for α-W thin films is also linearly dependent on temperature. However, $R_H(T)$ changes sign from negative to positive as temperature is reduced below 130 K, indicating a competition between electron and hole carriers from multi-bands in α-W thin films. The Hall effect data presented in Fig. 4.4 provide valuable input into any theoretical

effort to understand the effects of band structure, scattering mechanisms, and possibly, surface electronic states of β-W and α-W thin films incorporating the inherently strong SOC. Small amounts of oxygen in β-W or α-W thin films may also have some effect on the Hall effect and its temperature dependence.

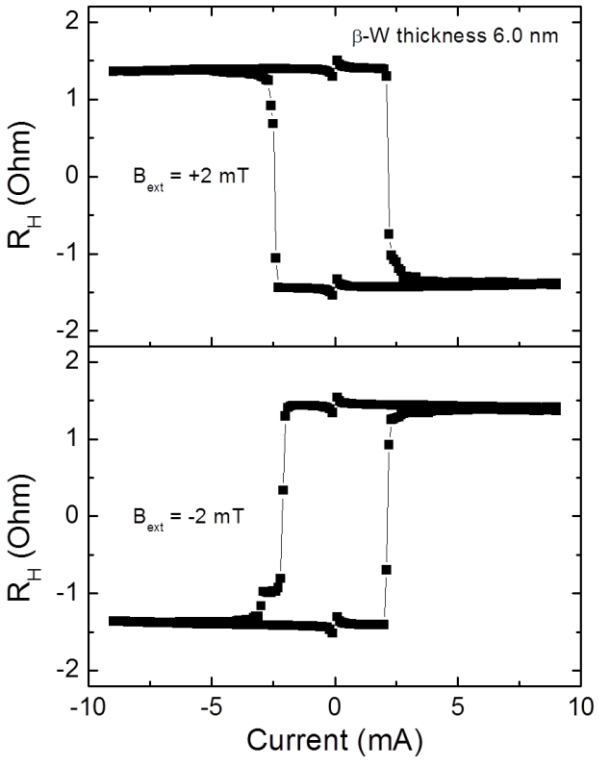

FIG. 4.5. Current-induced magnetic-switching curves in the (6.0)W/(1.0)$Co_{40}Fe_{40}B_{20}$/(1.6)MgO/ (1.0)Ta sample, under an in-plane magnetic field $\mathbf{B_{ext}}$ of +/– 2 mT (+ parallel, and – antiparallel to current direction). Magnetic swithcing in the PMA (1.0)$Co_{40}Fe_{40}B_{20}$ layer is sensed by measuring the anomalous Hall voltage in the layer as current is sweeped in the Hall bar sample.

Using sputtering method described above, we make a layered structure in the form of (t)W/(1.0)$Co_{40}Fe_{40}B_{20}$/(1.6)MgO/(1.0)Ta (number in the units of nm). The (1.0)Ta capping layer is used to prevent the oxidation of the active layers from atmosphere. After annealing, the (1.0)$Co_{40}Fe_{40}B_{20}$ develops PMA [3] while the W layer remains in β-phase. Figure 4.5 shows the magnetic switching of the (1.0)$Co_{40}Fe_{40}B_{20}$

layer by the spin current generated in the (6.0)β-W layer. We detect the switching by measuring the anomalous Hall effect of the (1.0)$Co_{40}Fe_{40}B_{20}$ layer. Under an in-plane magnetic field of 2 mT, the sample (6.0)W/(1.0)$Co_{40}Fe_{40}B_{20}$/(1.6)MgO/(1.0)Ta can be magnetically switched with a critical current (I_C) of 2.2 mA, corresponding to a critical current density (J_C) of 1.2×10^6 A/cm^2 in the W layer, about 1 order of magnitude smaller than those obtained in other similar structures [2,5,21-22].

4.3 Conclusion

In conclusion, β-W thin films have been fabricated using a simple magnetron sputtering process. The as-deposited films are all in β-W phase from 3.0 to 26.7 nm. In order to obtain PMA in a layered structure of β-W/$Co_{40}Fe_{40}B_{20}$ /MgO, high vacuum thermal magnetic annealing is required at a temperature of 280°C. Upon annealing, β-W is transformed into the α-W phase above a critical thickness of 22.1 nm, which is much larger than the spin diffusion length (3.5 nm) for β-W thin films. The stabilization of β-W up to 22.1 nm after annealing makes it possible to exploit the full GSHE in β-W thin films. In our films, the typical grain size is about one third to one half of the thin film thickness. The room temperature resistivity of the bulk β-W film is 195 μΩ-cm and the electron mean free path is very short at 0.45±0.26 nm. Interestingly, the resistivity of β-W is insensitive to temperature and thickness. At 14.5 nm, the temperature coefficient of resistivity is nearly zero between 10 and 360 K. This property is highly desirable for spintronics applications, since the magnetic switching power from GSHE does not depend on temperature. Finally, the normal Hall coefficient for β-W thin films has been

measured between 10 K and 300 K. Although the Hall coefficient has the same magnitude as bulk α-W, it carries a negative sign. This observation provides a useful input into any theory on the electronic structure of β-W incorporating the large SOC. Using our sputtering and magnetic thermally annealing process, PMA and low switching current density can be achieved in the layered structure of β-W/$Co_{40}Fe_{40}B_{20}$ /MgO.

References

1. C.-F. Pai, L. Liu, Y. Li, H. W. Tseng, D. C. Ralph, and R. A. Buhrman, Appl. Phys. Lett. **101**, 122404 (2012).
2. C.-F. Pai, M.-H. Nguyen, C. Belvin, L. H. Vilela-Leão, D. C. Ralph, and R. A. Buhrman, Appl. Phys. Lett. **104**, 082407 (2014).
3. Qiang Hao and Gang Xiao, Phys. Rev. Appl. **3**, 034009 (2015).
4. P. Petroff, T. T. Sheng, A. K. Sinha, G. A. Rozgonyi, and F. B. Alexander, J. Appl. Phys. **44**, 2545 (1973); http://dx.doi.org/10.1063/1.1662611.
5. L. Liu, C.-F. Pai, Y. Li, H. W. Tseng, D. C. Ralph, and R. A. Buhrman, Science **336**, 555 (2012).
6. Supriyo Datta, Sayeef Salahuddin, and Behtash Behin-Aein, Appl. Phys. Lett. **101**, 252411 (2012);
7. W.R. Morcom, W.L. Worrell, H.G. Sell, and H.I. Kaplan, Metallurgical Trans. **5**,155 (1974).
8. C. C. Tang and D. W. Hess, Appl. Phys. Lett. **45**, 633 (1984).
9. D. C. Paine, J. C. Bravman, and C. Y. Yang, Appl. Phys. Lett. **50**, 498 (1987).

10. I.A. Weerasekera, S.I. Shah, D.V. Baxter, and K.M. Unruh, Appl. Phys. Lett. **64**, 3231 (1994).
11. S. M. Rossnagel, I. C. Noyan, and C. Cabral Jr., J. Vac. Sci. Technol. **B20**, 2047 (2002); http://dx.doi.org/10.1116/1.1506905
12. D. Choi, B. Wang, S. Chung, X. Liu, A. Darbai, A. Wise, N.T. Nuhfer, K. Barmak, A.P. Warren, K.R. Coffey, and M.F. Toney, J. Vac. Sci. Technol. **A29**, 051512 (2011).
13. K. Salamon, O. Milat, N. Radic, .P Dubcek, M. Jercinovic, and S. Bernstorff, J. Phys. D: Appl. Phys. **46**, 095304 (2013).
14. V. N. Volodin, Yu. Zh. Tuleushev, and E. A. Zhakanbaev, J. Surf. Invest. **8**, 169 (2014).
15. A. J. Narasimham, M. Medikonda, A. Matsubayashi, P. Khare, H. Chong, R.J. Matyi, A. Diebold and V.P. LaBella, AIP Advances **4**, 117139 (2014).
16. A.L. Patterson, Phys. Rev. **56**, 978 (1939).
17. L. Eckertova, *Physics of Thin Films* (Plenum, New York, 1986), pp 219-233.
18. *AIP Handbook*, 3rd Ed., edited by Dwight E. Gray (American Institute of Physics, New York, 1972).
19. Z. Bastl, Thin Solid Films **10**, 311-313 (1972).
20. *Physical and Chemical Properties of the Elements*, edited by G.V. Samsonov (Naukova Dumka, Kiev, 1965).
21. X. Qiu, P. Deorani, K. Narayanapillai, K.-S. Lee, K.-J. Lee, H.-W. Lee and H. Yang, Scientific Reports **4**, 4491 (2014).

22. Luqiao Liu, O. J. Lee, T. J. Gudmundsen, D. C. Ralph, and R. A. Buhrman, Phys. Rev. Lett. **109**, 096602 (2012).

Chapter 5

Giant Spin Hall Effect in beta-W

5.1 Introduction

Recently, the Spin Hall Effect (SHE) [1-3] has received much attention. Particularly noteworthy is the phenomenon of the Giant Spin Hall Effect (GSHE) [4-13] in non-magnetic metals with strong spin-orbit coupling (SOC). Very large spin Hall angles (Θ) have been discovered in solids ranging from simple SOC solids of Pt ($|\Theta|$=0.08) [4–8], Ta (0.15) [9], W (0.30) [10-11] to topological insulators, Bi_2Se_3 (2.0-3.5) [12] and $BiSbTe_3$ (1.4-4.25) [13]. With a large Θ, a metal can convert efficiently a longitudinal electrical charge current (J_c) to a transverse spin current (J_s), which can be used to manipulate magnetization states in spintronic devices [6, 9, 14]. GSHE has brightened the prospect of magnetic random access memory (MRAM) and spin-logic (SL) devices. One promising embodiment of the new MRAM is to prepare an interface between a GSHE solid and a ferromagnetic thin film (FM) with perpendicular magnetic anisotropy (PMA), commonly referred to as a free layer. The injected spin current from the GSHE solid yields a spin-transfer torque (STT) inside the free layer to effect a magnetization switching [15-16]. The magnetic states representing the digital bits are sensed by an integrated magnetic sensor, *e.g.*, a magnetic tunneling junction (MTJ) [9] or a Tunneling magnetoresistive (TMR) element [17]. The conjectured STT-MRAM with

PMA has the advantages of low power consumption, high reliability and durability, and data non-volatility, over earlier generations of MRAM.

Among the limited number of GSHE solids uncovered so far, tungsten in its high resistivity and metastable beta (β) phase is fundamentally interesting for its large SOC, and potentially useful in applications. Having the largest spin Hall angle (0.3) among transition metals, its preparation is compatible to modern semiconductor fabrication processes. However, structures of β-W/FM with PMA have not been obtained. Although PMA can be enabled by inserting a Hf layer into the bilayer, as in β-W/Hf/CoFeB [10], the Hf layer has the deleterious effects of lowering the effective Hall angle and increasing fabrication complexity. Furthermore, β-W itself has not been well studied, for example, the intrinsic spin Hall angle and spin diffusion length in bulk β-W remain undefined.

In this letter, we report the achievement of β-W/CoFeB/MgO with robust PMA without the need of any insertion layer. We have successfully extended the thickness of β-W to 9 nm in this structure, which has allowed us to explore the variation of spin Hall angle over a broad range of β-W thickness. As a result, we have determined that the bulk-limit spin Hall angle is 0.40 and the spin diffusion length is 3.5 nm for β-W. Both parameters are key to the understanding of the β-W in the context of GSHE, and to the development of STT-MRAM and spin-logic incorporating β-W and FM with PMA. The STT-induced switching current for magnetization reversal is of the order of $10^6 A/cm^2$, one order of magnitude smaller than other similar structures [9-10].

5.2 Sample Preparation and Characterization

We have prepared our layered structures (stacks) on thermally oxidized Si wafers using a high vacuum magnetron sputtering system. The base pressure is less than 2×10^{-8} Torr and the Ar sputtering pressure is ~2.2 mTorr. For each sample, the whole stack was sequentially deposited in the order of W/CoFeB/MgO/Ta. The capping layer, (1)Ta with the thickness value in the units of nanometer (nm), is used to prevent oxidation of the active layers from atmosphere. The DC sputtering power for CoFeB was kept at 10W. The thickness of the $Co_{40}Fe_{40}B_{20}$ layer was always fixed at 1 nm, allowing CoFeB to develop the PMA. For the formation of β-W, we applied a low DC sputtering power of only 3W intermittently to keep the deposition rate below 0.02 nm/s. Multiple stacks have been made with W thickness in the range of the 2.5 to 9.0 nm. These stacks were patterned using photolithography into standard Hall bars for both Hall Effect and resistivity measurements, with the longitudinal dimensions of 20×55 μm^2 in area. Finally, the stacks were annealed at 280°C for 1 min with two hours of ramping up and six hours of natural cooling in vacuum (1×10^{-6} Torr) and magnetic field (0.45 Tesla) which is perpendicular to the stacks. We performed magnetotransport measurements on these stacks using an electromagnet at room temperature. We used the Quantum Design® Physical Property Measurement System (PPMS) to measure the saturated magnetization (M_S) of the stacks at room temperature. M_S for (1)CoFeB in the stacks is about 1100 emu/cm^3. To confirm the phase of β-W, we measured the sheet resistance ($R_\square$) of the stacks denoted by (t)W/(1.0)CoFeB/(1.6)MgO/(1.0)Ta. Fig. 5.1 shows the value of $R_\square$ as a function of W thickness from 2.5 to 9.0 nm. The solid line is the best fit to the data

based on extracted resistivities of $\rho_W \approx 210\ \mu\Omega$-cm and $\rho_{FeCoB} \approx 80\ \mu\Omega$-cm, according to the relationship

$$R_{\square} = \left(\frac{\rho_W}{t} \cdot \frac{\rho_{CoFeB}}{t_{CoFeB}}\right) / \left(\frac{\rho_W}{t} + \frac{\rho_{CoFeB}}{t_{CoFeB}}\right). \quad (5.1)$$

Typical resistivities for the stable α-W phase and the metastable β-W phase are below 40 μΩ-cm and above 150 μΩ-cm, respectively. The high resistivity that we obtained indicates that we have β-W in all samples presented here. We have also used X-ray diffraction to confirm the β-W structure in a film with thickness of 9 nm.

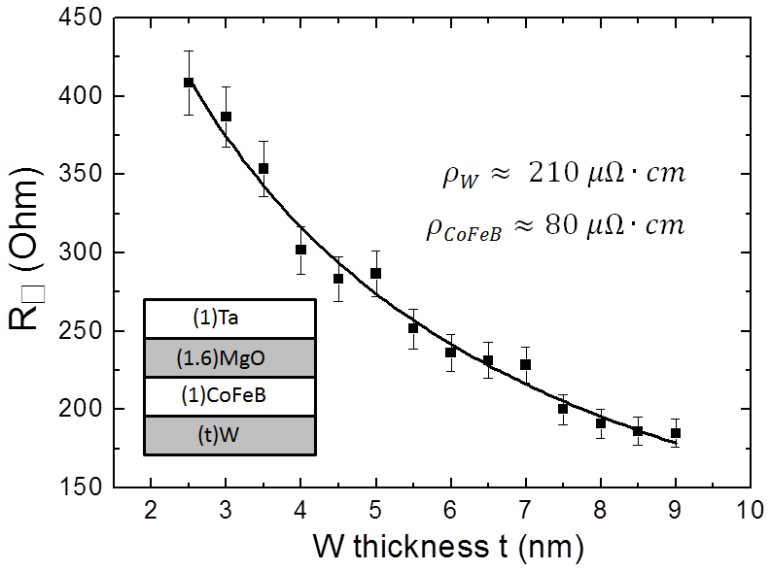

FIG. 5.1 Sheet resistance ($R_{\square}$) of (t)W/(1.0)CoFeB/(1.6)MgO/(1.0)Ta (thickness number in nm) multilayer stacks as a function of W thickness t (2.5-9.0 nm). The solid line is the best fit to the data based on extracted resistivities of $\rho_W \approx 210\ \mu\Omega$-cm and $\rho_{FeCoB} \approx 80\ \mu\Omega$-cm.

5.3 Results and discussion

The conditions for the magnetotransport measurement are illustrated in the schematic Fig. 5.2(a). We sent in a DC current along the *y*-axis of a Hall-bar sample, and measured the Hall voltage along the *x*-axis. We applied the external magnetic field ($\mathbf{B_{ext}}$)

in the *yz* plane with an angle β between the field and *y*-axis. The resulting magnetization vector (**M**) is also in the *yz* plane at an angle θ from the *y*-axis. Fig. 5.2(b) shows the anomalous Hall resistance (R_H) as a function of magnetic field applied perpendicularly to the sample plane (β =90°) for a series of samples with varying W thickness (3-9 nm), (t)W/(1.0)CoFeB/(1.6)MgO/(1.0)Ta. The square hysteresis loops for every sample reveal the attainment of PMA in the W/CoFeB without the need of an insertion layer between W and CoFeB. The switching field, or coercivity H_c, ranges from 5 Oe to 22 Oe.

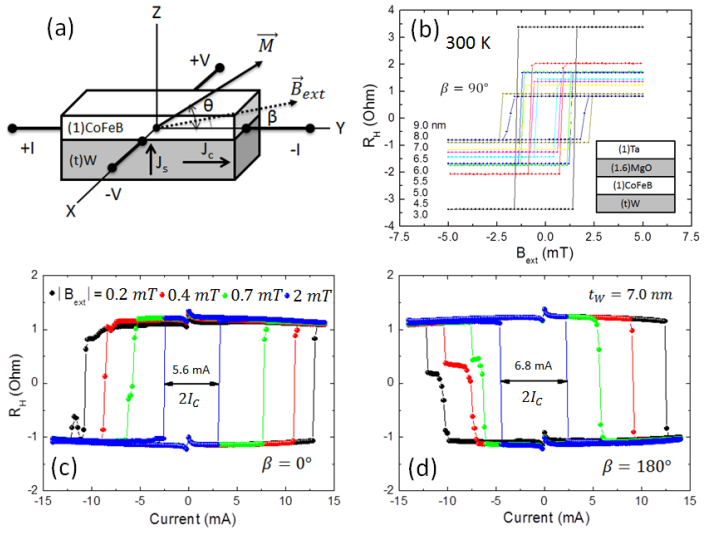

FIG. 5.2 (a) A schematic of W/CoFeB bilayer in the Hall bar configuration for magnetotransport measurement under an external magnetic field (**B_{ext}**) and an excitation DC current (I). J_c is the charge current density in the W layer, and J_s is the SHE converted spin current density into the CoFeB layer. (b) Anomalous Hall resistance versus cycling external magnetic field applied perpendicular to the stacks of (t)W/(1.0)CoFeB/(1.6)MgO/(1.0)Ta (t: 3.0-9.0 nm). (c, d) Current-induced magnetic switching curves in the (7.0)W/(1)CoFeB/(1.6)MgO/(1)Ta sample, under either a positive (β =0°) or a negative (β =180°) external field B_{ext} (0.2, 0.4, 0.7, 2 mT). From each switching curve, critical current (I_C) can be obtained as shown.

The anomalous Hall Effect (AHE) provides a sensing mechanism to measure the magnetization state of the CoFeB layer. From here on, we investigate how this state

responds to an excitation current (I) in the W layer and $\mathbf{B_{ext}}$. Fig. 5.2(c) shows current-induced magnetic switching behavior of a representative sample, (7.0)W/(1.0)CoFeB, under a series of positive ($\beta = 0°$) or negative ($\beta = 180°$) in-plane fields (B_{ext} = 0.2, 0.4, 0.7, and 2 mT). The bi-stable states of (**M** up and down) are accessible by cycling the current in both directions through a critical value (I_c), under either a positive or negative B_{ext}. We define the critical current (I_c) as the average of the positive and negative switching current. The values of switching current are somewhat different for $\beta = 0°$ and $\beta = 180°$. This is due to the hysteretic nucleation process which is stochastic. For (7.0)W/(1.0)CoFeB, I_c≈2.8 mA for $\beta = 0°$ and 3.4 mA for $\beta = 180°$, yielding an average I_c≈3.1 mA. Based on ρ_W≈210 μΩ-cm and ρ_{FeCoB}≈80 μΩ-cm, we estimated that the critical current and the critical current density in the W layer are $I_c(W)$≈2.3 mA and $J_c(W)$≈1.6×10^6 A/cm^2, respectively, under an in-plane field of 2 mT. In this particular sample, the current passing through the W layer is 82.1% of the total current through the stack (7.0)W/(1.0)CoFeB. This critical current density is about one order of magnitude smaller than what were obtained in other PMA structures: Ta/CoFeB [9,18-19], Pt/Co[20], and W/Hf/CoFeB [10].

The current-induced magnetic switching in PMA structures has been explained by the spin-transfer torque mechanism due to the injected spin current density (J_S) from the SOC solid with GSHE [20]. Under the measurement conditions of Fig. 5.2(a), the equilibrium orientation (θ) of **M** in the PMA CoFeB layer is determined from the condition that the net torque on **M** is zero [20], *i.e.*,

$$\tau_{tot} \equiv \hat{x}\cdot(\vec{\tau}_{ST} + \vec{\tau}_{ext} + \vec{\tau}_{an}) = \tau_{ST}^{0} + B_{ext}\sin(\theta-\beta) - B_{an}^{0}\sin\theta\cos\theta = 0\,, \qquad (5.2)$$

where $\tau_{ST}^0 = \frac{\hbar}{2eM_s t} J_S$ is the torque per unit moment, and B_{an}^0 is the perpendicular anisotropy field. This macrospin model predicts the current-induced magnetic switching, as shown in Fig. 5.2(c), at sufficient current density ($>J_c$) or corresponding spin-transfer torque τ_{ST}^0 per unit moment.

In the coherent spin rotation regime, Eq. (5.2) has also been used as a method to measure τ_{ST}^0, hence, the converted spin current density J_S from which the spin Hall angle can be derived ($\Theta = J_s/J_c$) [20]. In Eq. (5.2), the angle (θ) can be obtained from the anomalous Hall resistance, $R_H/R_0 = \sin\theta$, where R_0 is the maximum Hall resistance when **M** is perpendicular to the sample plane. According to Eq.(5.2), as B_{ext} approaches zero or infinity, θ reaches 0 or 90°, respectively. Under an intermediate B_{ext}, θ is dependent on τ_{ST}^0, B_{ext}, and B_{an}^0, as demonstrated in Fig. 5.3(a) which shows how the R_H or $\sin\theta$ varies as a function of B_{ext} under a positive or a negative current of 2 mA. It can be seen in Fig. 5.3(a) that, at an arbitrary $\sin\theta$, there exist two B_{ext} values, $B_+(\theta)$ and $B_-(\theta)$, corresponding to the positive and negative current, respectively. From Eq.(5.2),

$$\tau_{ST}^0(+J_S) + B_+(\theta)\sin(\theta-\beta) - B_{an}^0 \sin\theta\cos\theta = 0 \tag{5.3}$$

$$\tau_{ST}^0(-J_S) + B_-(\theta)\sin(\theta-\beta) - B_{an}^0 \sin\theta\cos\theta = 0\,. \tag{5.4}$$

By solving the simultaneous equations using combination of (3)±(4), one obtains

$$[B_+(\theta) - B_-(\theta)] = -\Delta\tau_{ST}^0 / \sin(\theta-\beta) \tag{5.5}$$

$$[B_+(\theta) + B_-(\theta)] = 2B_{an}^0 \sin\theta\cos\theta / \sin(\theta-\beta)\,, \tag{5.6}$$

where $\Delta\tau_{ST}^0 = \tau_{ST}^0(+J_S) - \tau_{ST}^0(-J_S) = 2\,\tau_{ST}^0(|J_S|)$. The experimental procedure implied in Fig. 5.3(a) generates the quantities of $B_+(\theta)$, $B_-(\theta)$, and θ. Then, using Eq. (5) and (6),

one can calculate $\tau_{ST}^{0}(|J_S|)$ and B_{an}^{0}. Fig. 5.3(b) shows $[B_{+}(\theta)-B_{-}(\theta)]$ as a function of $1/\sin(\theta-\beta)$, based on the data in Fig. 5.3(a). As predicted by Eq. (5.5), linear relations are confirmed for various current values, and the slope is $\Delta\tau_{ST}^{0}$ for each supplied current. Using this method, we have determined the spin-transfer torque per unit moment $\tau_{ST}^{0}(|J_S|)$ versus current in our samples with varying W thickness, as shown in Fig. 5.3(c). We also determined that the anisotropy field B_{an}^{0} is 214 mT for the sample used in Fig. 5.3(b).

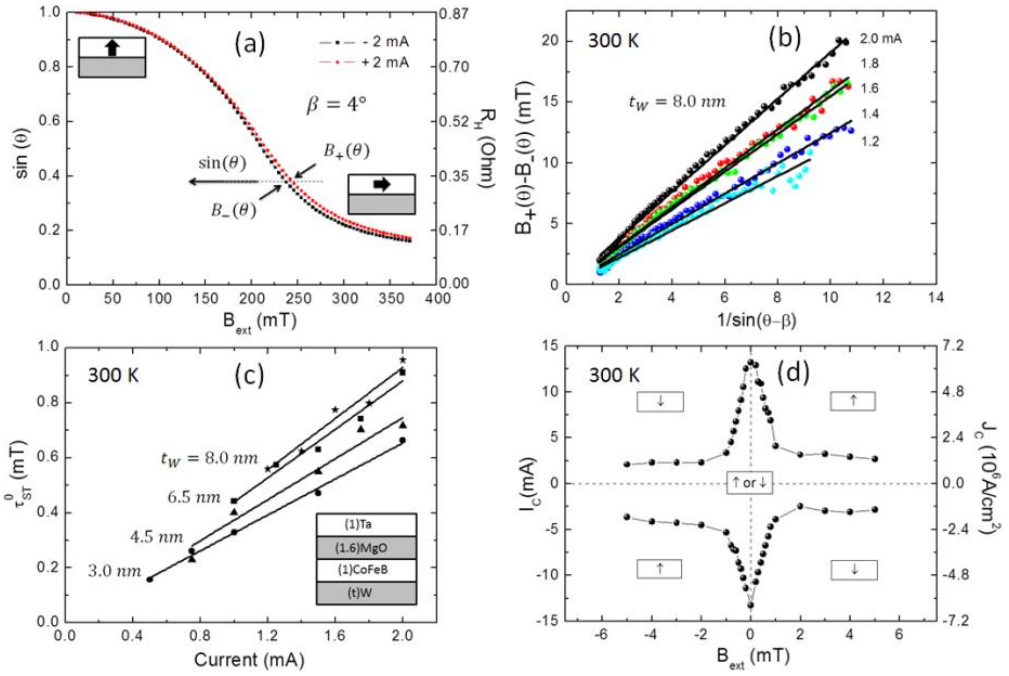

FIG. 5.3(a) Normalized Hall resistance (*i.e.*, sin θ) as functions of nearly in-plane magnetic field B_{ext} (β =4°) under a positive or negative current ($\pm$2mA). θ is the angle between the magnetization vector **M** and the *y*-axis. $B_{+}(\theta)$ and $B_{-}(\theta)$ are the magnetic fields required to rotate the **M** to θ corresponding to the positive and the negative current, respectively. (b) Linear relationships between $B_{+}(\theta)-B_{-}(\theta)$ and $1/\sin(\theta-\beta)$ under different excitation current (0.5-2 mA). The slope for each fitted straight line is the net spin-transfer torque per unit moment, $\Delta\tau_{ST}^{0}$, between the positive and negative excitation current. (c)

Spin-transfer torques (τ_{ST}^{0}) per unit moment as functions of excitation currents for (t)W/(1.0)CoFeB/(1.6)MgO/(1.0)Ta (t: 3.0-9.0 nm). All the torques are linear in current and vanish as current approaches zero. Thicker W generates more torque per unit of current. (d) Magnetic switching phase diagram of (7.0)W/(1.0)CoFeB/(1.6)MgO/(1.0)Ta, in the parameter space of B_{ext} and critical current (I_c) or critical current density (J_c). The arrows (↑ or ↓) denote the directions of the **M** vector in various regions. I_c is the net current into the Hall bar, and J_c is the corresponding current density *only* in the W layer. The lines connecting the data are guides to the eyes.

Based on data in Fig. 5.3(c), we calculated the spin Hall angle according to $\Theta = J_s/J_c = (\frac{2eM_s t}{\hbar})(\tau_{ST}^{0} / J_c)$. Fig. 5.4 shows the spin Hall angle as a function of W thickness (t) from 3 nm to 9 nm for the (t)W/(1.0)CoFeB/(1.6)MgO/(1.0)Ta system with PMA. At 9.0 nm, the spin Hall angle is 0.35 ± 0.04. In thinner limit, spin Hall angle decreases, as the W thickness becomes comparable to the spin diffusion length(λ_{sf}). The variation of the Hall angle versus W thickness allows us to obtain $\Theta(\infty)=0.40 \pm 0.03$ and $\lambda_{sf} = 3.5 \pm 0.3\ nm$ in the bulk β-W film, according to $\frac{J_s(t)}{Js(\infty)} = \frac{\Theta(t)}{\Theta(\infty)} = 1 - \text{sech}\left(\frac{t}{\lambda_{sf}}\right)$ [21] which is used to fit the data in Fig. 5.4. In comparison, $\Theta(5.2nm)=0.33 \pm 0.06$ was obtained in W/CoFeB/MgO with in-plane magnetic anisotropy, and *effective* $\Theta(4nm)=0.34 \pm 0.05$ in W/Hf/CoFeB/MgO with Hf-induced PMA. Our determination of the bulk $\Theta(\infty)$ and λ_{sf} for β-W is beneficial to further theoretical understanding of this important SOC solid and to the design of spintronic devices by selecting appropriate β-W thickness. Moreover, PMA can be achieved in W/CoFeB/MgO without the need of any insertion layer which reduces spin Hall angle [10].

As shown earlier in Fig. 5.2 (c), with sufficient current (*i.e.*, spin-transfer torque), **M** of the CoFeB layer will undergo switching which can also be described by Eq. (5.2). Based on results in Fig. 5.2(c), we have obtained the magnetic switching phase diagram, shown in Fig. 5.3(d), for a representative sample (7.0)W/(1.0)CoFeB/(1.6)MgO (area 20×55 μm^2). The critical switching current density (J_C) in the W layer decreases rapidly and linearly with increasing field (B_{ext}) up to a characteristic field B_0~1 mT, and at a slower rate when $B_{ext} > B_0$. As a comparison, B_0~15 mT and 300 mT have been measured for two other PMA systems, (5)Ta/(0.6 nm)CoFe/(1.8)MgO (area 1.2×15 μm^2) [22] and (2)Pt/(0.6)Co/AlO_x (20×200 μm^2) [20], respectively. The significantly lower B_0 obtained

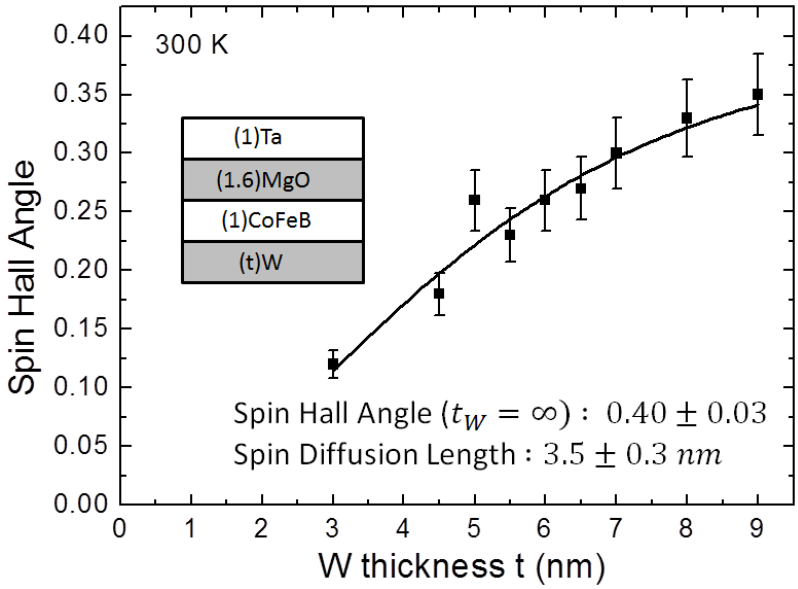

FIG. 5.4 Spin Hall angles versus W thickness for (t)W/(1.0)CoFeB/(1.6)MgO/(1.0)Ta (t: 3.0-9.0 nm). The line represents theoretical fitting to the data assuming a finite spin diffusion length in the β-W film. For the bulk β-W film, spin Hall angle is determined to be 0.40±0.03 and spin diffusion length is $3.5 \pm 0.3\ nm$ at room temperature.

in our PMA system bodes well for achieving reliable switching under a small external field. In STT-MRAM or spin-logic applications, a low biasing field can be much more

easily implemented than a ten-time larger field. It is noted that B_0 is of the magnitude of the nucleation field in our system (see coercivity values in Fig. 5.2(b)). From Fig. 5.2(c), we have obtained the lowest $J_C \sim 1.6\times10^6 A/cm^2$ at 2 mT, about 5 to 10 times smaller than other PMA systems. [9-10, 18-20]. Our insight is that this is partly due to the GSHE, and partly to the low coercivity in our samples which we developed through meticulous optimization of magnetic thermal annealing.

5.4 Conclusion

We have observed GSHE in β-W/CoFeB/MgO system with perpendicular magnetic anisotropy. We have determined that the spin Hall angle is 0.40 ± 0.03 and spin diffusion length is $3.5 \pm 0.3\ nm$ in bulk β-W film at room temperature. It is the largest spin Hall angle among elemental solids with a large spin-orbit coupling [4-11, 23-24]. We have obtained the magnetic switching phase diagram of the PMA CoFeB driven by spin-transfer torque from the β-W. Under an in-plane biasing field of only 2 mT, the switching current density is about $1.6\times10^6 A/cm^2$ which is the lowest among other PMA systems with GSHE. We have demonstrated that, without the need of any tricks such as the use of insertion layer, thick β-W films can be integrated with the well-known CoFeB ferromagnetic film to achieve a robust PMA. The large Hall angle and acquired PMA makes β-W an ideal candidate for STT-MRAM and spin-logic applications, with the added advantage of its compatibility to modern semiconductor fabrication. We also note that the long spin diffusion length would require somewhat thicker β-W film to take full advantage of its GSHE. This tends to increase the total current, which, coupled with the high resistivity of the β-W film, may require more power for magnetic switching.

References

1. M.I. Dyakonov and V.I. Perel, Current-induced spin orientation of electrons in semiconductors, Phys. Lett. **A35**, 459 (1971).
2. J. E. Hirsch, Spin Hall effect, Phys. Rev. Lett. **83**, 1834 (1999).
3. S. Zhang, Spin Hall effect in the presence of spin diffusion, Phys. Rev. Lett. **85**, 393 (2000).
4. A. Azevedo, L. H. Vilela-Leão, R. L. Rodríguez-Suárez, A. F. Lacerda Santos, and S. M. Rezende, Spin pumping and anisotropic magnetoresistance voltages in magnetic bilayers: Theory and experiment, Phys. Rev. B **83**, 144402 (2011).
5. N. Vlietstra, J. Shan, V. Castel, J. Ben Youssef, G. E. W. Bauer, and B. J. van Wees, Exchange magnetic field torques in YIG/Pt bilayers observed by the spin-Hall magnetoresistance, Appl. Phys. Lett. **103**, 032401 (2013).
6. L. Liu, T. Moriyama, D. C. Ralph, and R. A. Buhrman, Spin-torque ferromagnetic resonance induced by the spin Hall effect, Phys. Rev. Lett. **106**, 036601 (2011).
7. O. J. Lee, L. Q. Liu, C. F. Pai, Y. Li, H. W. Tseng, P. G. Gowtham, J. P. Park, D. C. Ralph, and R. A. Buhrman, Central role of domain wall depinning for perpendicular magnetization switching driven by spin torque from the spin Hall effect, Phys. Rev. B **89**, 024418 (2014).
8. A. Ganguly, K. Kondou, H. Sukegawa, S. Mitani, S. Kasai, Y. Niimi, Y. Otani, and A. Barman, Thickness dependence of spin torque ferromagnetic resonance in $Co_{75}Fe_{25}$/Pt bilayer films, Appl. Phys. Lett. **104**, 072405 (2014).
9. L. Liu, C.-F. Pai, Y. Li, H. W. Tseng, D. C. Ralph, and R. A. Buhrman, Spin-

torque switching with the giant spin Hall effect of tantalum, Science **336**, 555 (2012).

10. C.-F. Pai, M.-H. Nguyen, C. Belvin, L. H. Vilela-Leão, D. C. Ralph, and R. A. Buhrman, Enhancement of perpendicular magnetic anisotropy and transmission of spin-Hall-effect-induced spin currents by a Hf spacer layer in W/Hf/CoFeB/MgO layer structures, Appl. Phys. Lett. **104**, 082407 (2014).
11. C.-F. Pai, L. Liu, Y. Li, H. W. Tseng, D. C. Ralph, and R. A. Buhrman, Spin transfer torque devices utilizing the giant spin Hall effect of tungsten, Appl. Phys. Lett. **101**, 122404 (2012).
12. A. R. Mellnik, J. S. Lee, A. Richardella, J. L. Grab, P. J. Mintun, M. H. Fischer, A. Vaezi, A. Manchon, E.-A. Kim, N. Samarth and D. C. Ralph, Spin-transfer torque generated by a topological insulator, Nature **511**, 449 (2014).
13. Y. Fan, P. Upadhyaya, X. Kou, M.g Lang, S. Takei, Z. Wang, J. Tang, L. He, L.-T. Chang, M. Montazeri, G. Yu, W. Jiang, T. Nie, R. N. Schwartz, Y. Tserkovnyak and K. L. Wang, Magnetization switching through giant spin–orbit torque in a magnetically doped topological insulator heterostructures, Nature Materials **13**, 699 (2014).
14. D. Bhowmik, L. You, and S. Salahuddin, Spin Hall effect clocking of nanomagnetic logic without a magnetic field, Nature Nanotechnology **9**, 59 (2014).
15. J. C. Slonczewski, Current-driven excitation of magnetic multilayers, J. Magn. Magn. Mater. **159**, L1 (1996).
16. J. A. Katine, F. J. Albert, and R. A. Buhrman, Current-induced realignment of

magnetic domains in nanostructured Cu/Co multilayer pillars, Appl. Phys. Lett. **76**, 354 (2000).

17. M. Cubukcu, O. Boulle, M. Drouard, K. Garello, C. O. Avci, I. M. Miron, J. Langer, B. Ocker, P. Gambardella, and G. Gaudin, Spin-orbit torque magnetization switching of a three-terminal perpendicular magnetic tunnel junction, Appl. Phys. Lett., **104**, 042406 (2014).
18. C. Zhang, M. Yamanouchi, H. Sato, S. Fukami, S. Ikeda, F. Matsukura, and H. Ohno, Magnetization reversal induced by in-plane current in Ta/CoFeB/MgO structures with perpendicular magnetic easy axis, J. Appl. Phys. **115**, 17C714 (2014).
19. X. Qiu, P. Deorani, K. Narayanapillai, K.-S. Lee, K.-J. Lee, H.-W. Lee and H. Yang, Angular and temperature dependence of current induced spin-orbit effective fields in Ta/CoFeB/MgO nanowires, Scientific Reports 4, 4491 (2014).
20. Luqiao Liu, O. J. Lee, T. J. Gudmundsen, D. C. Ralph, and R. A. Buhrman, Current-induced switching of perpendicularly magnetized magnetic layers using spin torque from the spin Hall effect, Phys. Rev. Lett. 109, 096602 (2012).
21. L. Liu, T. Moriyama, D. C. Ralph, and R. A. Buhrman, Spin-torque ferromagnetic resonance induced by the spin Hall effect, Phys. Rev. Lett. 106, 036601 (2011).
22. N. Perez, E. Martinez, L. Torres, S.-H. Woo, S. Emori, and G. S. D. Beach, Chiral magnetization textures stabilized by the Dzyaloshinskii-Moriya interaction during spin-orbit torque switching, Appl. Phys. Lett. 104, 092403 (2014).

23. H. J. Zhang, S. Yamamoto, Y. Fukaya, M. Maekawa, H. Li, A. Kawasuso, T. Seki, E. Saitoh and K. Takanashi, Current-induced spin polarization on metal surfaces probed by spin-polarized positron beam, Scientific Reports 4,4844 (2014).

24. H. L. Wang, C. H. Du, Y. Pu, R. Adur, P. C. Hammel, and F. Y. Yang, Scaling of spin Hall angle in 3d, 4d, and 5d metals from $Y_3Fe_5O_{12}$/metal spin pumping, Phys. Rev. Lett. 112, 197201 (2014).

Chapter 6

Temperature Dependence of Giant Spin Hall Effect in Beta-Ta

6.1 Introduction

During the last few years, Giant Spin Hall Effect (GSHE) [1-14] has received much attention for its fundamental magnetotransport property and promising potential for spintronics applications, particularly in magnetic random access memories (MRAM), spin logics (SL), RF devices, and magneto-optical components. Solids with large atomic numbers and resistivities, such as Pt [4-8], β-Ta [9], and β-W [10-12], exhibit a very large spin Hall angle (SHA), a key and characterizing parameter of GSHE. The metastable β forms of Ta and W display much larger intrinsic resistivities than their corresponding stable α forms. The origin of GSHE is the enhanced spin-orbit coupling (SOC), based on which the search on solids with even larger SHA continues. Recently, it has been shown that some topological insulators are capable of generating phenomenally large GSHE [13, 14]. However, transition metals with GSHE have the advantages of compatibility to semiconductor fabrication process and ability to sustain larger bulk current densities. These transition metals typically carry a SHA in the range of 0.1 to 0.4 [9-12, 15-18].

A common method to study the GSHE is to use a bi-layer structure consisting of a thin film with large SOC and a ferromagnetic thin film (FM) whose magnetization (***M***) is

perpendicular to the bi-layer, a property called perpendicular magnetic anisotropy (PMA). A normal longitudinal current density in the SOC film induces a large transverse spin current, which exerts a spin-transfer torque (STT) on the $\boldsymbol{M}$ of the FM. Above a critical current density (J_c) inside the SOC film, $\boldsymbol{M}$ switches its direction abruptly via domain wall motion, which is experimentally measured by using the Anomalous Hall Effect (AHE) of the FM layer [9-10, 12]. To make GSHE useful for MRAM or SL applications, J_c must be reduced as much as possible by virtue of the large SHA and the interfacial match between the SOC and FM layers. A lower J_c reduces power consumption and improves durability in spintronic devices.

In this work, we conducted a comprehensive study on the electron transport, magnetotransport, and magnetic properties of the β-Ta/$Co_{40}Fe_{40}B_{20}$/MgO system over a wide temperature range (5K-300K). The ferromagnetic thin film $Co_{40}Fe_{40}B_{20}$ has the composition of $Co_{40}Fe_{40}B_{20}$. We focused our study on the unique configuration in which the $Co_{40}Fe_{40}B_{20}$ displays a robust PMA achieved under an optimal magnetic thermal annealing process. We have obtained the strength of SHA, magnetic anisotropy, magnetization as functions of temperature. We have also measured the magnetic switching phase diagram, which allowed us to observe the lowest switching current density among similar systems. Our approach shows that a systematic study on multiple properties in this type of systems is highly beneficial to the understanding of the GSHE and its spin-orbit coupling mechanism.

6.2 Experimental

We deposited a series of (t)Ta/(1)$Co_{40}Fe_{40}B_{20}$/(1.6)MgO (thickness number in nanometer, nm) multilayer stacks on thermally oxidized Si wafers in a homemade high vacuum magnetron sputtering system with a base pressure less than 2×10^{-8} Torr and Ar sputtering pressure ~2 mTorr. The face-up sputtering guns have a diameter of 5 cm and use an NdFeB permanent magnet ring. The target-substrate distance is 9 cm. The face-down substrates are thermally oxidized single crystal Si wafers (5-cm diameter), which rotate at about 50 rpm during deposition for achieving thickness uniformity. The off-center distance is 3 cm between the center of a substrate and that of a target. A capping layer of (1)Ta was deposited on top of the MgO layer to prevent oxidation of the metal layers from atmosphere. The growth rate of Ta was about 0.5Å/s under a DC sputtering power of 10W, and the substrates were kept at ambient temperature. The thin-film stacks were patterned using photolithography into standard Hall bars (20×55 μm^2 in area) for both Hall effect and resistivity measurements. Before measurements, the patterned samples were annealed in vacuum (1×10^{-6} Torr) at different temperatures for 1 hour with two hours of ramping up and six hours of natural cooling under a magnetic field of 0.45 Tesla perpendicular to the sample planes. We used the Quantum Design® Physical Property Measurement System (PPMS) for magnetization and transport measurement in the temperature range of 5K to 300K. We also used a few other transport measurement instruments equipped with electromagnets for some measurements.

6.3 Results and discussion

To determine the resistivities of Ta and $Co_{40}Fe_{40}B_{20}$ films, we measured the sheet resistance ($R_{\square}$) of Ta/ $Co_{40}Fe_{40}B_{20}$ bilayers with different Ta thickness ($4 \leq t \leq 8$ nm). The analysis on the thickness dependent data of $R_{\square}$ provides the resistivity of the Ta layer ($\rho_{Ta} \approx 200$ μΩ-cm) and the resistivity of the $Co_{40}Fe_{40}B_{20}$ layer ($\rho_{CoFeB} \approx 100$ μΩ-cm) post-annealing. The high resistivity of Ta is indicative of its β phase, as its α phase has a typical resistivity of ~50 μΩ-cm [19, 20]. Fig. 6.1 shows the temperature dependence of resistivities for both Ta and $Co_{40}Fe_{40}B_{20}$ layers from 5 K to 300 K. The resistivity of the $Co_{40}Fe_{40}B_{20}$ layer is weakly dependent on temperature (3% variation), ranging from 103 μΩ-cm at 5K to 100 μΩ-cm at 300 K. The resistivity of the β-Ta layer also changes little (9% variation) from 218 μΩ-cm at 5 K to 200 μΩ-cm at 300 K. Therefore, the temperature dependent electron-photon scattering is not the main mechanism for resistivity. Disorder scattering in $Co_{40}Fe_{40}B_{20}$, which is temperature independent, is responsible for its resistivity. The thickness of $Co_{40}Fe_{40}B_{20}$ is only 1 nm which sets a limit on the electron mean-free-path. The as-prepared $Co_{40}Fe_{40}B_{20}$ has an amorphous structure. After post-deposition magnetic annealing, $Co_{40}Fe_{40}B_{20}$ retains some of its structural disorder as implied by its high resistivity. The slight increase in the resistivity of the β-Ta layer at low temperatures is interesting. It is not clear what the mechanism is for the resistivity upturn. Low temperature can induce lattice strain on the 4nm β-Ta thin film and change its band structure somewhat. The resistivity upturn may also be due to some thermally activated electron transport processes. It is noted that the weakly temperature dependent resistivities bode well for spintronics application with regard to thermally

stable operation. However, the large resistivity in β-Ta layer does pose a challenge in that the power consumption is somewhat large in order to generate sufficient spin-polarized current using β-Ta.

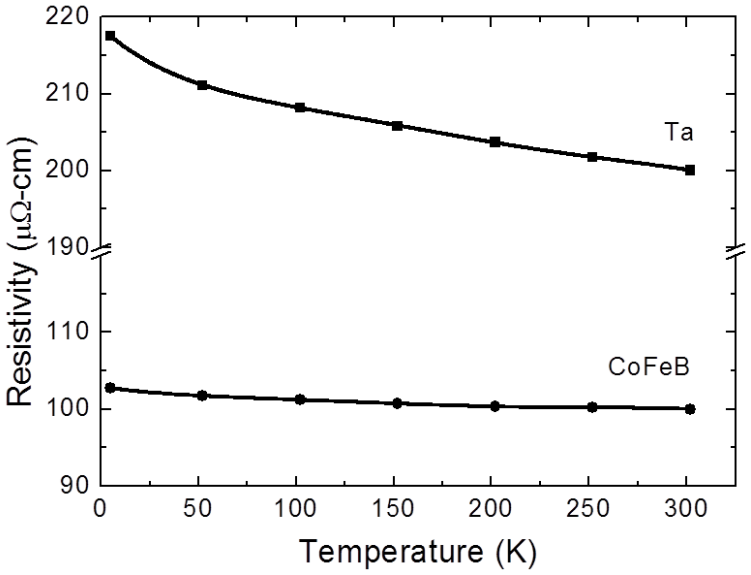

FIG. 6.1 Resistivities of β-Ta (4 nm thick) and CoFeB (1 nm thick) as functions of temperature

In our bilayer structures, the $Co_{40}Fe_{40}B_{20}$ layer is always fixed at 1 nm which is required for surface-induced PMA. We investigated the magnetic stability of this thin $Co_{40}Fe_{40}B_{20}$ layer as a function of temperature. Fig. 6.2 (a) shows the in-plane magnetization versus magnetic field curves (up to +/- 2T) measured at various temperatures between 5 and 300K for the (4)Ta/(1)$Co_{40}Fe_{40}B_{20}$/(1.6)MgO sample. A large magnetic field of the order of 0.5T is required to saturate the magnetization. By extrapolating the magnetization curve within the region of 1 to 2T to zero field, we extracted the spontaneous magnetization, M_s, which is displayed in Fig. 6.2(b) versus temperature. Within 5 and 300 K, M_s decreases about 23% linearly with temperature, rather than following the Bloch's law of $T^{3/2}$ dependence based on three dimensional

(3D) spin wave excitations. The linear temperature dependence in M_s is due to the 2D nature of our 1 nm-thick $Co_{40}Fe_{40}B_{20}$. It is consistent with observations in other and similar ultrathin ferromagnetic films [21,22]. The measurement of $M_s(T)$ is necessary to study the thermal effect on GSHE to be presented later.

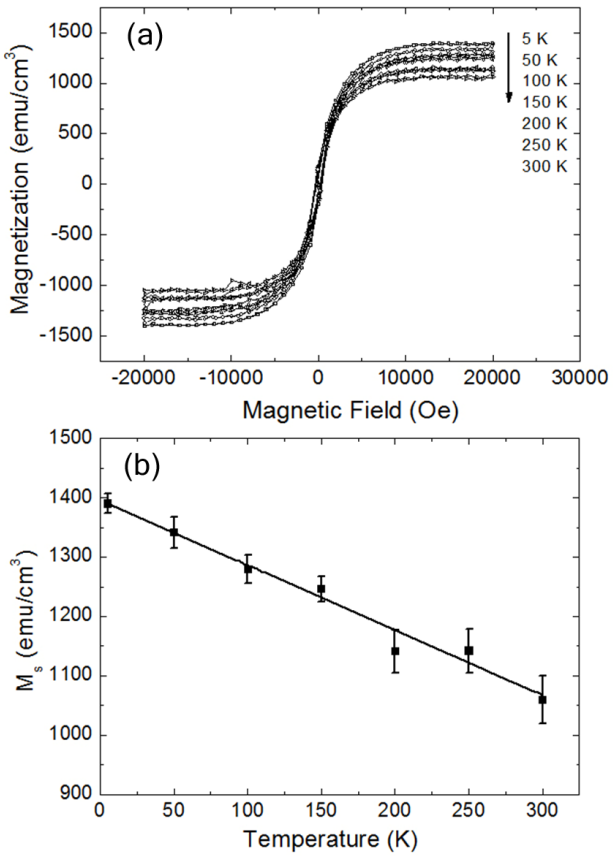

FIG. 6.2 (a) Magnetization of (4)Ta/(1)CoFeB/(1.6)MgO stack as a function of temperature; (b) Extracted spontaneous magnetization ($\boldsymbol{M_S}$) as a function of temperature.

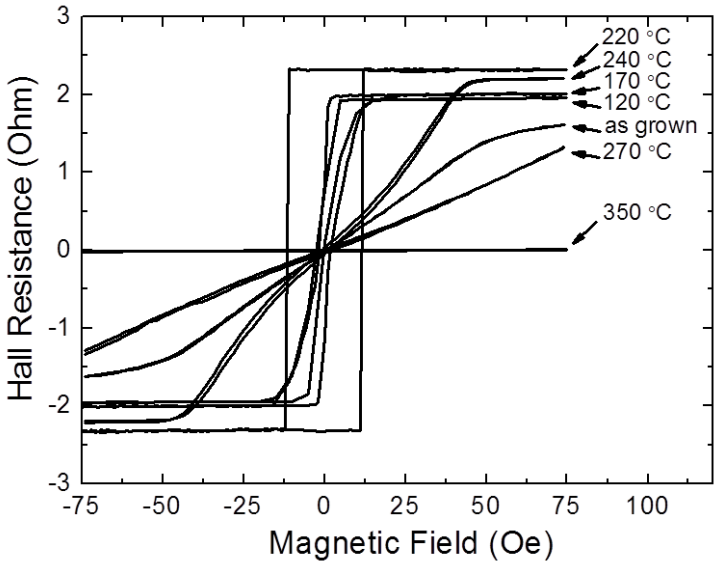

FIG. 6.3 The anomalous Hall resistance of (4)Ta/(1)CoFeB/(1.6)MgO stacks versus magnetic field applied perpendicularly to the stacks for samples annealed at different temperatures.

Fig. 6.3 shows the magnetic hysteresis loops (in the format of AHE resistance which is proportional to magnetization) of a series of (4)Ta/(1)$Co_{40}Fe_{40}B_{20}$/(1.6)MgO stacks annealed in vacuum at different temperatures under a perpendicular field of 0.45T. The as-deposited sample exhibits magnetic in-plane anisotropy. Increasing the annealing temperature cultivates the emergence of a perpendicular magnetic anisotropy (PMA). At 220°C, a robust PMA is established with a nearly perfect square hysteresis loop. The coercivity H_c is 12 Oe. For our chosen layer structure, 220°C seems to be the optimized temperature for PMA, as further annealing (270°C) brings back the dominance of in-plane magnetic anisotropy again (see Fig. 6.3). At 350°C, the AHE disappears due to the possible disintegration of the layered structure. Our results show that the magnetic thermal annealing has a profound influence on the magnetic quality and the PMA of the Ta/$Co_{40}Fe_{40}B_{20}$/MgO system. It seems that a robust PMA is sustained in a well ordered Ta/$Co_{40}Fe_{40}B_{20}$/MgO structure developed under magnetic annealing at 220°C. The as-prepared sample has sharp but disordered interfaces, which are unable to support the

PMA. On the other hand, higher annealing temperatures (> 220°C) are also deleterious to PMA, most likely, due to significant diffusion in the interfacial region. Our finding of the optimal annealing condition is consistent with previous study [23, 24]. From here on, we will focus on the (4)Ta/(1)$Co_{40}Fe_{40}B_{20}$/(1.6)MgO stacks annealed at 220°C.

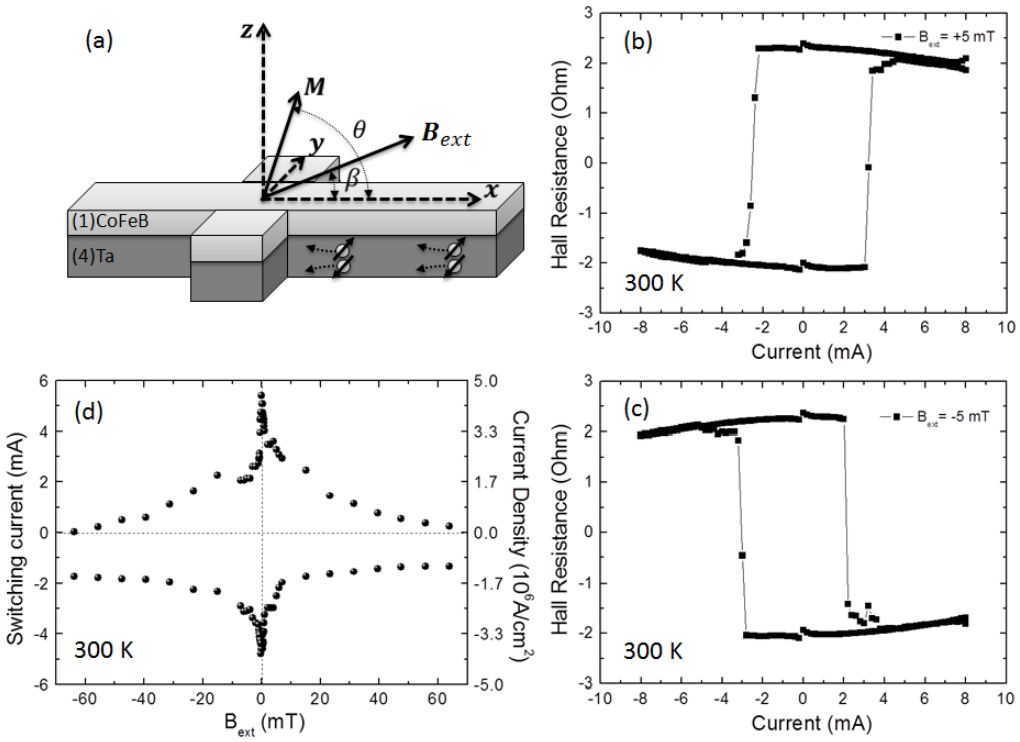

FIG. 6.4 (a) Schematic drawing of Ta/CoFeB bilayer in the Hall bar configuration for magnetotransport measurement under an external magnetic field ($\boldsymbol{B_{ext}}$) and total excitation current ($\boldsymbol{I}$) along the *x*-axis; (b) and (c) Current induced magnetic switching curves in (4)Ta/(1)CoFeB/(1.6)MgO stack under a positive (β =0°) and a negative (β =180°) external field $\boldsymbol{B_{ext}}$ of 5mT. The average total critical current I_C is determined to be 2.7 mA; (d) Magnetic switching phase diagram of (4)Ta/(1)CoFeB/(1.6)MgO in the parameter space of $\boldsymbol{B_{ext}}$ and total critical current $\boldsymbol{I_C}$ or critical current density $\boldsymbol{J_C}$ (*only* in the Ta layer).

To measure the SHE in Ta, we measured the magnetotransport of the (4)Ta/(1)$Co_{40}Fe_{40}B_{20}$/(1.6)MgO Hall bar according to the schematic shown in Fig. 6.4(a). We applied a charge current *I* along the length of the Hall bar (*x*-axis). As a result, a spin current is generated perpendicular to the Ta layer (along the *z*-axis). An external magnetic

field, $\boldsymbol{B_{ext}}$, was applied to the sample within the *z*-*x* plane at an angle β to the *x*-axis. The direction of magnetization vector, ***M***, of the $Co_{40}Fe_{40}B_{20}$ layer is controlled by $\boldsymbol{B_{ext}}$ and the spin-transfer torque (STT) of the SHE-induced spin current. The angle of ***M***, defined by the angle θ to the *x*-axis, is determined by measuring the AHE resistance, *i.e.*, $\sin\theta = R_H/R_0$. R_0 is the maximum Hall resistance when ***M*** is perpendicular to the sample plane. The equilibrium condition for ***M*** is,

$$\tau_{tot} \equiv \hat{x}\cdot(\vec{\tau}_{ST} + \vec{\tau}_{ext} + \vec{\tau}_{an}) = \tau_{ST}^{0} + B_{ext}\sin(\theta-\beta) - B_{an}^{0}\sin\theta\cos\theta = 0 \qquad (6.1)$$

where $\tau_{ST}^{0} = \dfrac{\hbar}{2eM_s t} J_S$, and B_{an}^{0} is the perpendicular anisotropy field [25]. According to this macrospin model, a magnetic switching would occur at a critical current density (J_c) which corresponds to a critical STT (τ_{ST}^{0}). Fig. 6.4(b) and (c) show two special cases for such magnetic switching under B_{ext} = 5mT and -5mT (along *x*-axis), respectively. The switching current at approximately 2.7 mA in the bi-layer of $Ta/Co_{40}Fe_{40}B_{20}$ corresponds to a charge current density in Ta layer of $J_c \approx 2.3\times10^6$ A/cm^2. Under a comparable B_{ext}, this observed J_c is the smallest critical current density ever reported in $Ta/Co_{40}Fe_{40}B_{20}/MgO$ and $Pt/Co/AlO_x$ systems [9, 13, 16, 25-26].

Fig. 6.4(d) shows our experimentally observed magnetic switching phase diagram of the (4)Ta/(1)CoFeB/(1.6)MgO structure under the influence of B_{ext} (along *x*-axis) and current (or current density in the Ta layer only). It can be seen that, as we reduce B_{ext}, a larger critical current is required to provide complete switching between M_z and $-M_z$. At B_{ext} =0, consecutive cycling in current leads to partial switching between various magnetic domain states. The switching current density at zero field is determined to be 4.2×10^6 A/cm^2, which is much smaller than previously reported values [13, 17-18, 27].

To achieve reliable and complete switching, a small field of B_{ext} = 5 mT along the *x*-axis is sufficient.

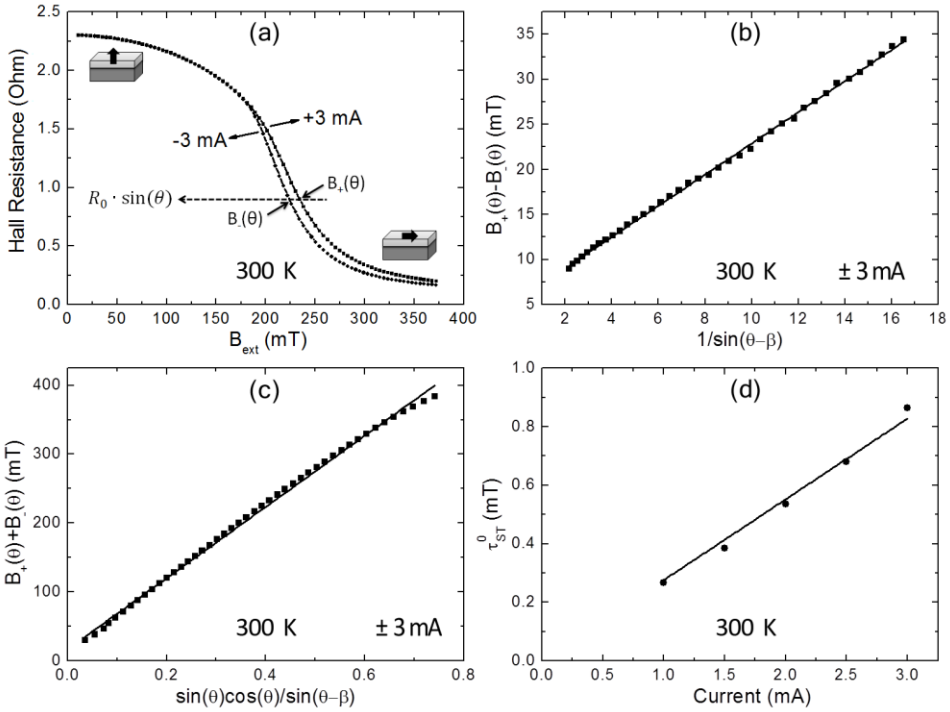

FIG. 6.5 (a) Hall resistance as a function of in-plane magnetic field along *x*-axis under ±3 mA excitation currents. θ is the angle between the magnetization vector ***M*** and the *x*-axis and can be obtained from the relationship sin θ =R_H/R_0 where R_0 is the Hall resistance with ***M*** perpendicular to sample plane; (b) Linear relationships between $[B_+(\theta) - B_-(\theta)]$ and $1/\sin(\theta - \beta)$ as expected from Eq. (6.4); (c) Linear relationships between $[B_+(\theta) + B_-(\theta)]$ and $\sin\theta\cos\theta / \sin(\theta - \beta)$ as expected from Eq. (6.5); (d) The spin-transfer torque as a function of total excitation current in the Ta/CoFeB/MgO stack. The slope of the linear curve provides the torque per unit of total charge current.

To measure quantitatively the induced STT (τ_{ST}^0) and spin current (J_s) for a given charge current (J_c), we bring our system as shown in Fig. 6.4(a) into the coherent spin rotation regime, where the ***M*** rotates from 90° to 0° coherently under an increasing B_{ext} along the x-axis (see Fig. 6.5(a)) and a positive or negative charge current. At such moderately high fields (up to 375 mT), we do not need to be concerned with domain wall

formation or thermally activated processes. The macro-spin model of Eq. (6.1) is fully valid. Fig. 6.5 (a) shows the R_H (= $R_0 \sin\theta$) of the $Co_{40}Fe_{40}B_{20}$ layer as a function of B_{ext} under a positive and a negative current of 3 mA (in Ta/CoFeB bilayer). At an arbitrary $R_0 \sin\theta$, two B_{ext} values exist, $B_+(\theta)$ and $B_-(\theta)$, corresponding to the positive and negative current, respectively. From Eq. (6.1),

$$\tau_{ST}^0(+J_S) + B_+(\theta)\sin(\theta-\beta) - B_{an}^0 \sin\theta\cos\theta = 0 \tag{6.2}$$

$$\tau_{ST}^0(-J_S) + B_-(\theta)\sin(\theta-\beta) - B_{an}^0 \sin\theta\cos\theta = 0\,. \tag{6.3}$$

By solving the simultaneous equations using the combinations of (2)±(3), one obtains

$$[B_+(\theta) - B_-(\theta)] = \Delta\tau_{ST}^0 / \sin(\theta-\beta) \tag{6.4}$$

$$[B_+(\theta) + B_-(\theta)] = 2B_{an}^0 \sin\theta\cos\theta / \sin(\theta-\beta)\,, \tag{6.5}$$

where $\Delta\tau_{ST}^0 = \tau_{ST}^0(+J_S) - \tau_{ST}^0(-J_S) = 2\,\tau_{ST}^0(|J_S|)$. The experimental procedure implied in Fig. 6.5(a) generates the quantities of $B_+(\theta)$, $B_-(\theta)$ and θ. Then, using Eq.(6.4) and (6.5), one can calculate $\tau_{ST}^0(|J_S|)$ and B_{an}^0. Fig. 6.5(b) shows $[B_+(\theta) - B_-(\theta)]$ as a function of $1/\sin(\theta-\beta)$, and Fig. 6.5(c) shows $[B_+(\theta) + B_-(\theta)]$ as a function of $sin(\theta)cos(\theta)/sin(\theta-\beta)$ based on the data in Fig.6.5(a). The value of β in our setup is measured to be 2°. As predicted by Eqs. (6.4) and (6.5), the slopes in Figs. 6.5(b) and (c) are $\Delta\tau_{ST}^0$ and 2 B_{an}^0, respectively. Fig. 6.5(d) shows the STT values, $\tau_{ST}^0(|J_S|)$, under various charge currents. As predicted, the STT is proportional to the current. The magnetic anisotropy constant, B_{an}^0, remains independent of current. Using the formula for SHA,

$$\Theta = J_S/J_C = \left(\frac{2eM_s t}{\hbar}\right)(\tau_{ST}^0 / J_c)\,, \tag{6.6}$$

we calculated the spin Hall angle (Θ) for the 4nm-thick Ta, which is 0.11±0.01 at 300 K. The main source of Θ uncertainty is in the thicknesses of our films. Also, using Eq. (6.5), we obtained the magnetic anisotropy constant B_{an}^{0}, which is $260 \pm 5\ mT$ at 300 K.

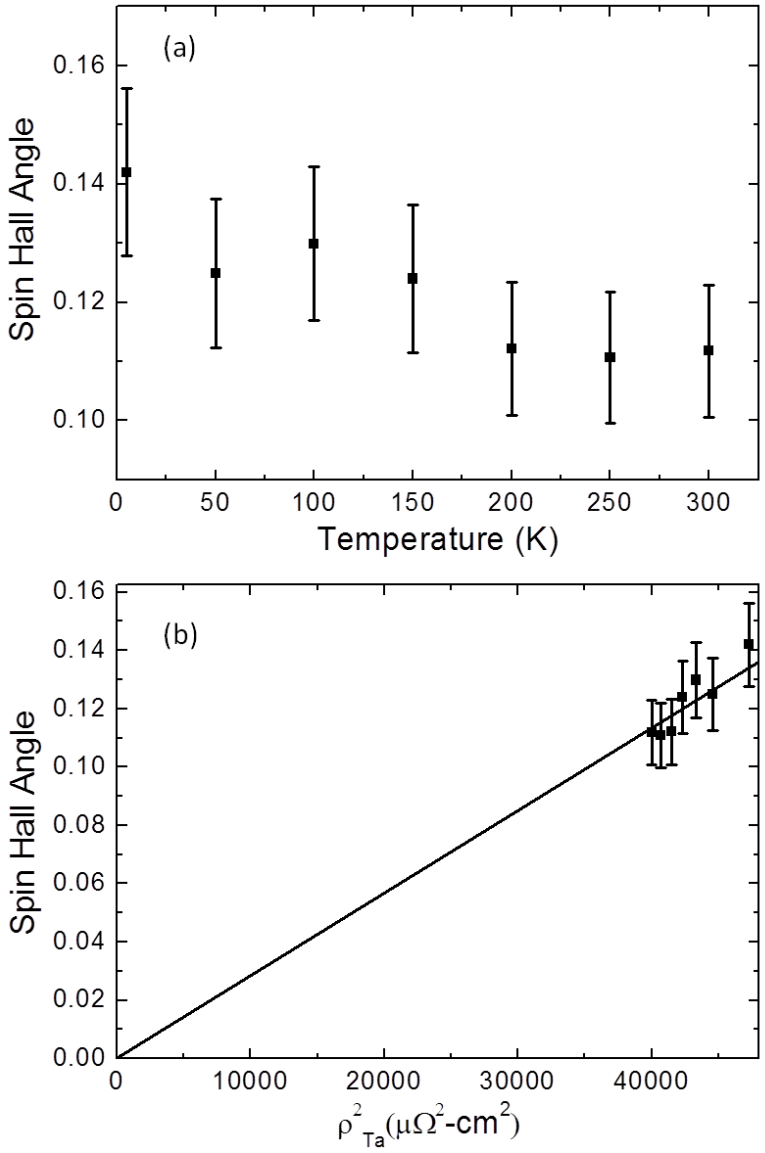

FIG. 6.6 (a) Determined spin Hall angle of β-Ta versus temperature; (b) Scaling relation between SHA and ρ_{Ta}^{2}.

We have repeated the measurement and analysis over the temperature range of 5K-300K to study the thermal effect on GSHE. Fig. 6.6(a) shows the SHA as a function

of temperature. SHA steadily increases (27%) from 0.11 at 300K to 0.14 at 5K. In metals with spin orbit coupling, the anomalous Hall effect scales with resistivity (ρ) linearly or quadratically (ρ^2). The former is due to the extrinsic skew scattering and the latter due to

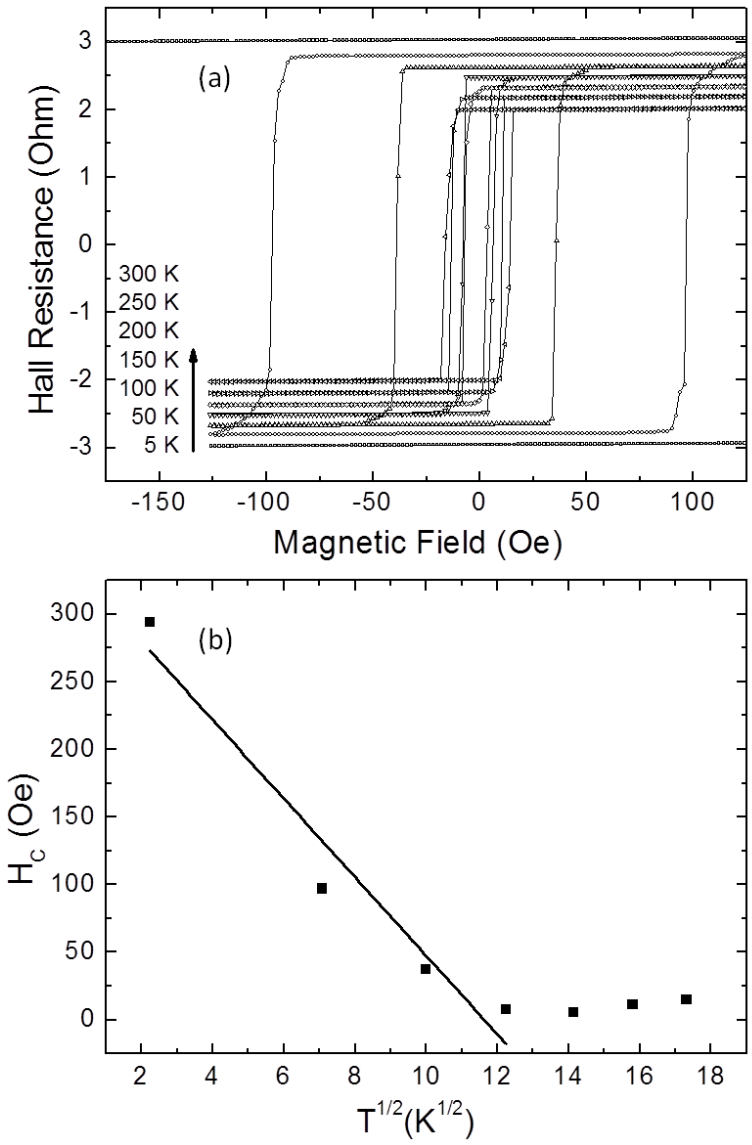

FIG. 6.7 (a) Square Hysteresis loops (β =90°) at different temperatures; (b) Coercivity of (4)Ta/(1) $Co_{40}Fe_{40}B_{20}$/(1.6)MgO multilayer as a function of temperature.

the extrinsic side jump or intrinsic mechanism in spin-orbit coupling[28]. In metals with high resistivity, the scaling relation of Hall angle $\Theta \propto \rho^2$ is most likely. Fig. 6.6 (b) shows

the spin Hall angle of our samples as a function of ρ^2, which explains our data better than a linear correlation. Due to limited variations in our spin Hall angle and ρ data, more studies are needed to confirm the exact correlation be between the spin Hall angle and ρ. However, our observation does indicate a positive correlation between the GSHE and high resistivity.

Next, we focus on the thermal effect of the magnetic properties of the (4)Ta/(1)$Co_{40}Fe_{40}B_{20}$/(1.6)MgO structure, in particular, the coercivity (H_c) and the magnetic anisotropy constant. These are important parameters for applications, because they influence the thermal stability of the magnetic elements such as memory cells. Fig. 6.7(a) shows the hysteresis loops (measured as AHE resistance) between 5K and 300 K in the $\beta = 90°$ configuration. Robust PMA is sustained over the whole temperature range, with square-like hysteresis loops. Between 150K and 300 K, H_c is low at 10-20 Oe. Below 150 K, H_c increases significantly, reaching 300 Oe at 5K. The strong temperature dependence in H_c is an indication of the mechanism of thermally activated domain wall (DW) motion, which predicts the following form,

$$H_c=H_0(1-aT^{1/2}) \qquad (6.7)$$

where H_0 is the coercivity at 0K and the constant a depends on the activation energy of DW motion [29-31]. Fig. 6.7(b) shows that between 5K and 150K, Eq. (6.7) can account for the temperature dependence of H_c in our sample. Interestingly, between 150K and 300K, there exists another mechanism for H_c (~15 Oe) which is nearly independent of temperature. The weakly temperature dependent H_c near room temperature is beneficial to applications.

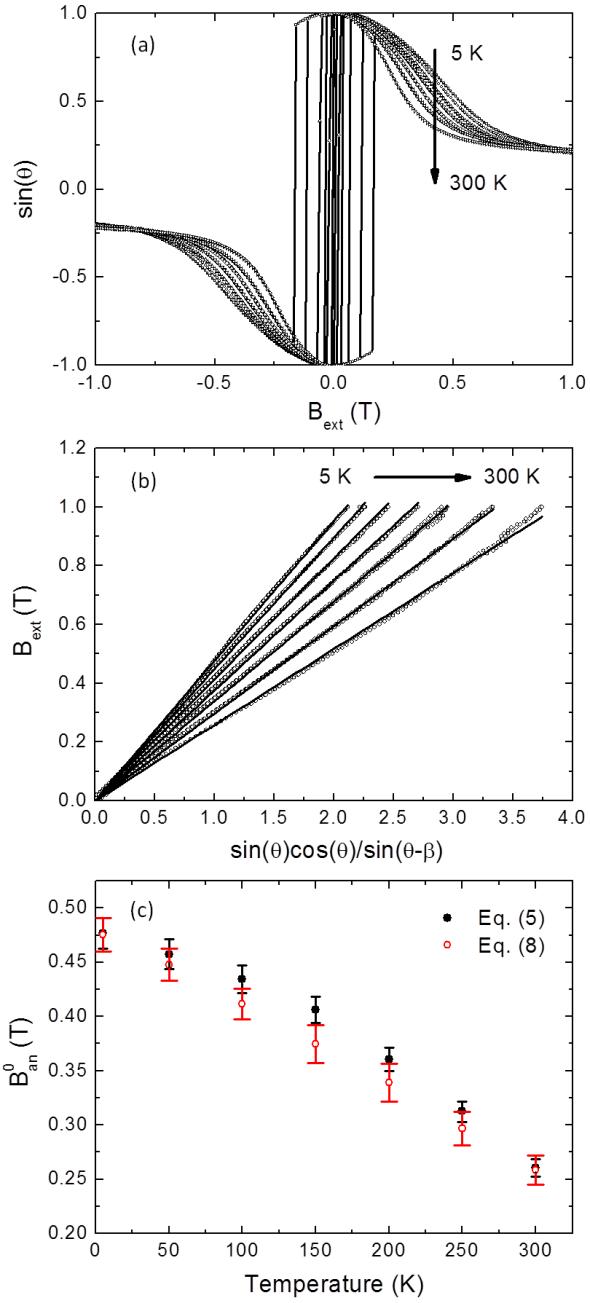

FIG. 6.8 (a) Normalized anomalous Hall resistance ($\sim sin\theta$) versus nearly in-plane magnetic field ($\beta \sim 0°$) at different temperatures. Switching is caused by the nonzero β angle (slight tilting); (b) The $\boldsymbol{B_{ext}}$ as a linear function of $sin(\theta)cos(\theta)/sin(\theta-\beta)$ with slope equal to the anisotropy field strength B_{an}^{0} according to Eq. (6.5); (c) The extracted B_{an}^{0} as a function of temperature using Eq. (6.5) and (6.8).

There are two ways to extract the magnetic anisotropy constant B_{an}^{0}. The first method is given by Eq.(6.5), in which a finite charge current is supplied to the Hall bar. In the second method, one can reduce the charge current to nearly zero. Then, Eq. (6.5) is reduced to

$$B_{ext} = B_{an}^{0} sin(\theta) cos(\theta) / sin(\theta - \beta) \ . \qquad (6.8)$$

Fig. 6.4(a) shows the normalized AHE resistance (R_H/R_0), which is $sin(\theta)$, as a function of an in-plane magnetic field B_{ext}, measured at multiple temperatures between 5K and 300K. As B_{ext} is varied from -1 T to 0, $\boldsymbol{M}$ rotates coherently from θ ~ - 180° to - 90°. As B_{ext} increases into the positive field region, above a critical field (H^*), $\boldsymbol{M}$ switches abruptly to θ ~ + 90°, and then coherently rotates toward θ ~ 180° with increasing field strength. The existence of H^* is due to the fact the sample plane is slightly tilted in such a way the in-plane field is not precisely within the plane (i.e., $H_c = H^* tan\beta$). Based on Fig. 6.8(a), we plot B_{ext} as a function of $sin(\theta)cos(\theta)/sin(\theta - \beta)$ in Fig. 6.8(b). As expected from Eq. (6.8), at every temperature, complete linear relationship is observed. The slopes of these lines are $B_{an}^{0}(T)$. Using both methods, we have determined $B_{an}^{0}(T)$ as shown in Fig. 8(c). The results from the two methods are consistent between each other. $B_{an}^{0}(T)$ is 0.475 T at 5 K and decreases monotonically to 0.260 T at 300 K.

The large variation of $B_{an}^{0}(T)$ (73%) within 5K and 300 K is the result of increasing magnetic surface anisotropy constant K_s, which opposes the increasingly large magnetic shape anisotropy (larger M_s) at low temperatures. $B_{an}^{0}(T)$ consists of two terms, one from magnetic shape anisotropy and the other from PMA, *i.e.*,

$$B_{an}^{0}(T) = \frac{2K_s(T)}{tM_s(T)} - 4\pi M_s(T) \qquad (6.9)$$

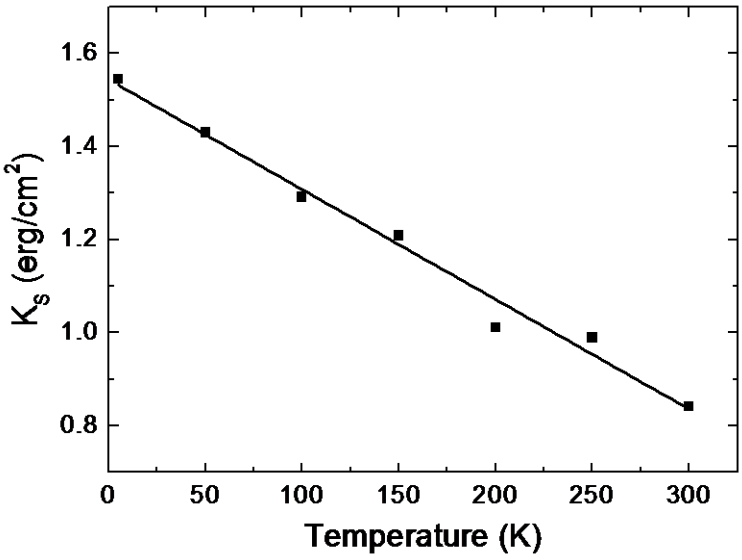

FIG. 6.9 Perpendicular magnetic surface anisotropy constant (K_s) in (4)Ta/(1)CoFeB/(1.6)MgO as a function of temperature.

In Eq. (6.9), In Eq. (6.9), $B_{an}^{0}(T)$ and $M_S(T)$ have been determined as shown in Fig. 6.8(c) and Fig. 6.2(b), respectively. The thickness (t) of $Co_{40}Fe_{40}B_{20}$ is 1nm. Therefore, from Eq.(6.9), we can calculate $K_S(T)$, which is shown in Fig. 6.9. Over the whole temperature range studied (5K-300K), K_s is linearly dependent on temperature, increasing 85% from 0.84 erg/cm^2 at 300 K to 1.55 erg/cm^2 5 K. It is reported in the (2)MgO/(t)$Co_{40}Fe_{40}B_{20}$/(5)Ta/(10)Ru layered structure, the K_s is 1.03 erg/cm^2 at 300K. [32]. The value of K_s is comparable for both systems which share the same interface (MgO/CoFeB) on one side and somewhat different interface on the other side (CoFeB/β-Ta, versus CoFeB/Ta/Ru). Therefore, the MgO/CoFeB interface seems to contribute the most to the PMA (K_s). It is a coincidence that both $K_s(T)$ and $M_s(T)$ depend linearly on temperature in our layered structure. We note that $M_s(T)$ is due to the thermally excited spin waves in the confinement of a thin film, and is characterized by the exchange

coupling and the dimensionality. On the other hand, $K_s(T)$ is characterized by the spin-orbit coupling at the interfaces of a magnetic thin film.

6.4 Conclusion

In conclusion, we have performed a comprehensive study on the GSHE and magnetic properties of the (4)Ta/(1)$Co_{40}Fe_{40}B_{20}$/(1.6)MgO spin-orbit coupled system over a wide temperature range between 5K and 300 K. We have optimally annealed the system in high vacuum and in a strong magnetic field, to develop a robust perpendicular magnetic anisotropy. The spin Hall angle in Ta is very large with a value of 0.14 at 5K and 0.11 at 300 K. We have determined the magnetic anisotropy field of 0.475 T at 5K and 0.260 T at 300K. We have achieved a low switching current density of 2.3×10^6 A/cm^2 in the presence of 5 mT in-plane magnetic field. This is the lowest switching current density among all studies reported on the Ta/$Co_{40}Fe_{40}B_{20}$/MgO systems. The resistivities of the β-Ta and the $Co_{40}Fe_{40}B_{20}$ are weakly dependent on temperature, indicating the dominance of electron elastic scatterings from disorder (intrinsic or interfacial) and/or spin-orbit interaction. The spontaneous magnetization of the 1nm-thick $Co_{40}Fe_{40}B_{20}$ layer exhibits linear temperature dependence, rather than following the Bloch's law of spin wave excitations in a 3D system. The GSHA in Ta combining with a ferromagnetic layer with PMA have provided us with a fertile platform to study a plethora of spin dependent transport and magnetic properties. Our results may benefit future spintronic devices such as MRAMs, spin logics, or RF oscillators.

References

1. M.I. Dyakonov and V.I. Perel, Phys. Lett. **A35**, 459 (1971).

2. J. E. Hirsch, Phys. Rev. Lett. **83**, 1834 (1999).

3. S. Zhang, Phys. Rev. Lett. **85**, 393 (2000).

4. A. Azevedo, L. H. Vilela-Leão, R. L. Rodríguez-Suárez, A. F. Lacerda Santos, and S. M. Rezende, Phys. Rev. B **83**, 144402 (2011).

5. N. Vlietstra, J. Shan, V. Castel, J. Ben Youssef, G. E. W. Bauer, and B. J. van Wees, Appl. Phys. Lett. **103**, 032401 (2013).

6. L. Liu, T. Moriyama, D. C. Ralph, and R. A. Buhrman, Phys. Rev. Lett. **106**, 036601 (2011).

7. O. J. Lee, L. Q. Liu, C. F. Pai, Y. Li, H. W. Tseng, P. G. Gowtham, J. P. Park, D. C. Ralph, and R. A. Buhrman, Phys. Rev. B **89**, 024418 (2014).

8. A. Ganguly, K. Kondou, H. Sukegawa, S. Mitani, S. Kasai, Y. Niimi, Y. Otani, and A. Barman, Appl. Phys. Lett. **104**, 072405 (2014).

9. L. Liu, C.-F. Pai, Y. Li, H. W. Tseng, D. C. Ralph, and R. A. Buhrman, Science **336**, 555 (2012).

10. C.-F. Pai, M.-H. Nguyen, C. Belvin, L. H. Vilela-Leão, D. C. Ralph, and R. A. Buhrman, Appl. Phys. Lett. **104**, 082407 (2014).

11. C.-F. Pai, L. Liu, Y. Li, H. W. Tseng, D. C. Ralph, and R. A. Buhrman, Appl. Phys. Lett. **101**, 122404 (2012).

12. Qiang Hao and Gang Xiao, Phys. Rev. Applied. **3**, 034009 (2015).

13. A. R. Mellnik, J. S. Lee, A. Richardella, J. L. Grab, P. J. Mintun, M. H. Fischer, A. Vaezi, A. Manchon, E.-A. Kim, N. Samarth, and D. C. Ralph, Nature **511**,449 (2014).

14. Y. Fan, P. Upadhyaya, X. Kou, M.g Lang, S. Takei, Z. Wang, J. Tang, L. He, L.-T. Chang, M. Montazeri, G. Yu, W. Jiang, T. Nie, R. N. Schwartz, Y. Tserkovnyak, and K. L. Wang, Nature Materials **13**, 699 (2014).

15. M. Cubukcu, O. Boulle, M. Drouard, K. Garello, C. O. Avci, I. M. Miron, J. Langer, B. Ocker, P. Gambardella, and G. Gaudin, Appl. Phys. Lett., **104**, 042406 (2014).

16. X. Qiu, P. Deorani, K. Narayanapillai, K.-S. Lee, K.-J. Lee, H.-W. Lee, and H. Yang, Scientific Reports **4**, 4491 (2014).

17. D. Bhowmik, L. You, and S. Salahuddin, Nature Nanotechnology **9**, 59 (2014).

18. S. Emori, E. Martinez, K.-J. Lee, H.-W. Lee, U. Bauer, S.-M. Ahn, P. Agrawal, D. C. Bono, and G. S. D. Beach, Phys. Rev. B **90**, 184427 (2014).

19. L. A. Clevenger, A. Mutscheller, J. M. E. Harper, C. Cabral Jr., and K. Barmak, J. Appl. Phys. **72**, 4918 (1992).

20. Mildred H. Read and C. Altman, Appl. Phys. Lett. **7**, 51 (1965).

21. G. Xiao, C.L. Chien, and M. Natan, J. Appl. Phys. **61**, 4314(1987).

22. J. Kim, J. Sinha, S. Mitani, M. Hayashi, S. Takahashi, S. Maekawa, M.

Yamanouchi, and H. Ohno, Phys. Rev. B **89**, 174424 (2014).

23. D.C Worledge, G. Hu, D.W Abraham, J.Z. Sun, P.L. Trouilloud, J. Nowak, S. Brown, M.C. Gaidis, E.J. O'sullivan, R.P. Robertazzi, Appl. Phys. Lett. **98**, 022501 (2011).
24. C. O. Avci, K. Garello, C. Nistor, S. Godey, B. Ballesteros, A. Mugarza, A. Barla, M. Valvidares, E. Pellegrin, A. Ghosh, I. M. Miron, O. Boulle, S. Auffret, G. Gaudin, and P. Gambardella, Phys. Rev. B **89**, 214419 (2014).
25. L. Liu, O. J. Lee, T. J. Gudmundsen, D. C. Ralph, and R. A. Buhrman, Phys. Rev. Lett. **109**, 096602 (2012).
26. C. Zhang, M. Yamanouchi, H. Sato, S. Fukami, S. Ikeda, F. Matsukura, and H. Ohno, J. Appl. Phys. **115**, 17C714 (2014).
27. N. Perez, E. Martinez, L. Torres, S.-H. Woo, S. Emori, and G. S. D. Beach, Appl. Phys. Lett. **104**, 092403 (2014).
28. N. Nagaosa, J. Sinova, S. Onoda, A. H. MacDonald, and N. P. Ong, Rev. Mod. Phys. **82**, 1539 (2010).
29. Z. Zablotshii, M. Kisielewski, O. Tsiganenko, and J. Ferre, Acta Phys. Polonica A **97**, 471 (2000).
30. M. Tsai, C. Cheng, C.C. Tsai, and G. Chern, J. Appl. Phys. **113**, 17C118 (2013).
31. K. Narayanapillai, X. Qiu, J. Rhensius, and H. Yang, J. Phys D **47**, 105005 (2014).
32. X.Y. Liu, W.Z. Zhang, M.J. Carter, and Gang Xiao, J. Appl. Phys. **110**, 033910 (2011).

Chapter 7

Anomalous Hall Effect in Fe-Pt Alloy

7.1 Introduction

The rich spin-orbit interaction in Pt-based alloys has offered the platform for studying the ferromagnetic Anomalous Hall effect (AHE) and for understanding the underlying physics [1]. Compared to ordinary Hall effect, the AHE enhances the magnetic field sensing capability by almost two or three orders of magnitude, making AHE sensors practical for relevant sensing applications [2-3]. Although people have reported works in Fe_xPt_{100-x} alloys [4], there has been a lack of a systematic study focusing on the AHE at different temperature, Fe concentration and alloy thickness. Understanding how the properties changes with different sample thickness and Fe concentration will help us find the optimal combination that associates with higher Hall coefficient, larger Hall angle or lower noise level. Also, temperature dependent study will provide the guidance for applying proper AHE sensors in different temperature environment and achieve the highest AHE. Most importantly, we hope this systematic study will complete our understanding in the physics and mechanisms in AHE. Hence, we investigated in the Fe_xPt_{100-x} alloys in various combinations of Fe concentration from 27% to 47% and thickness from 18 Å to 300 Å at temperatures from 2 K to 300 K. This work confirmed our previous results in Ref. [5] as Fe_xPt_{100-x} alloy with 29% Fe

concentration presents largest Hall slope, and also discovered temperature and thickness dependence on this Fe-Pt system. Another important factor of AHE that we focus on is Hall angle (ρ_{xy}/ρ_{xx}) which indicates the percentage of converting longitudinal current to transverse current. The enhancement of Hall angle could significantly improve the efficiency of AHE sensors for practical magnetic field sensing applications [6]. Meanwhile, we examined the scaling law between Hall coefficient Rs and longitudinal resistivity ρ_{xx} ($Rs \sim \rho_{xx}^{n}$) by varying temperature from 2 K to 300 K in different Fe_xPt_{100-x} samples and investigated the intrinsic and extrinsic mechanisms that give rise to the AHE in Fe-Pt system [7-8].

The Fe-Pt based AHE sensors caught a lot of attention due to their fantastic advantages including GHz operating frequency [9], easy fabrication process and low-noise performance when compared to the semiconductor Hall sensors. Although semiconductor Hall sensors could offer higher sensitivity to 1000V/AT [10] which is about one or two orders of magnitude larger than our best AHE sensor, our Fe-Pt thin-film sensor exhibits better noise performance since the semiconductor Hall sensor always suffers from the random telegraph noise especially when operating current gets larger [11]. Thus, the noise level of AHE sensor could be one or two orders of magnitude smaller than semiconductor Hall sensors, and thus performs equally well or even better in terms of signal-to-noise ratio compared to semiconductor Hall sensor in a certain frequency range. The Noise-equivalent Field (noise spectrum density divided by sensitivity in a 1 Hz bandwidth) of our best Fe-Pt Hall sensor is 7 μT at 1 Hz and 0.05 μT at 1k Hz [12].

In addition, the fabrication procedure of AHE Hall sensors takes only one step Fe-Pt deposition after photolithography pattern and one lift-off step, making it easy and fast to produce. Our samples are fabricated using magnetron sputtering in vacuum environment below $1 \times 10^{-7}\ Torr$, and the sputtering rates of Pt and Fe are separately controlled to achieve different Fe concentrations in the alloy after careful calibrations. Thermally oxidized Si substrates are utilized and pre-patterned with photoresist before sputtering Fe_xPt_{100-x}. Hall and longitudinal resistivity are first done by four-probe measurement in a perpendicular magnetic field at room temperature; Both the temperature dependent measurements and the magnetic property measurements are performed by Physical Property Measurement System (PPMS). Vibrating Sample Magnetometer (VSM) is well calibrated using standard Palladium before and after measurements, both showing smaller than 1.6% error. Besides, as we have noticed that annealing process (at 320 °C) always tends to reduce the AHE by as much as 50%, all samples in this study are not annealed.

7.2 Experimental

We first study the magnetic properties of Fe_xPt_{100-x} alloys with different thicknesses and Fe concentrations at varying temperature. In $Fe_{29}Pt_{71}$ Hall bars of different thicknesses ranging from 40 Å to 300 Å, as plotted in Fig. 1(a), we observe that saturation field decreases with the inverse of thickness at every temperature from 2K to 300K. Linear curves are fitted for each set of data. Clearly, thinner samples have reduced saturation field because of larger perpendicular anisotropy. Higher temperature also leads

to lower saturation field, implying that thermal fluctuation enhances the magnetic moment to be aligned with external magnetic field. Furthermore, by extending the fitted lines to the zero saturation field (X axis), we extract the critical thickness of $Fe_{29}Pt_{71}$ without ferromagnetism as 1.72 nm at room temperature and 1.13 nm at 2 K. Besides, in Fig. 7.1(b), Fe concentration also indicates linearly dependent saturation field for all 300 Å Fe_xPt_{100-x} samples. This is predictable since higher Fe concentration in the same sample volume (Hall bar area times thickness) contains proportionally more magnetic moment that needs to be saturated.

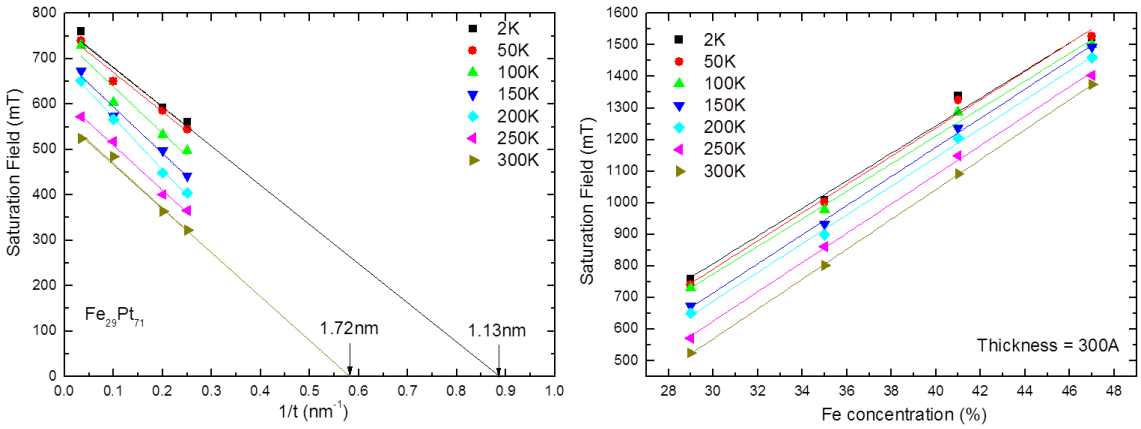

Fig. 7.1 (a) Linear relationship between saturation field of $Fe_{29}Pt_{71}$ and the inverse of the sample thickness at different temperatures. Extensions of linear fitting curves indicate critical thickness of $Fe_{29}Pt_{71}$ with full perpendicular anisotropy. The critical thicknesses are 1.13 nm and 1.72 nm at 2 K and 300 K respectively. (b) Linear relationship between saturation field of Fe_xPt_{100-x} and Fe concentration x, with x equals to 29, 35, 41, 47 respectively.

To better understand the magnetic properties, we also study the temperature dependent on the magnetizations of the Fe_xPt_{100-x} thin-film samples. According to the Bloch's law,

$$Ms(T)/Ms(0) = 1 - AT^{3/2}, \tag{7.1}$$

magnetization declines with increasing temperature in the behavior expressed in Equation (7.1) which is also plotted in Figure 7.2.(a). It can be seen that $Ms(T)$ declines faster in thinner Fe_xPt_{100-x} samples. Further examination of the magnetization $Ms(T)$ and curve fitting to extract the Bloch coefficient A provides the information of spin-wave stiffness constant D. It can be calculated using the equation

$$A = 2.612\left(\frac{V}{S}\right)\left(\frac{k_B}{4\pi D}\right)^{3/2}, \tag{7.2}$$

where V is the volume per magnetic (Fe) atom, S is the spin, and k_B is the Boltzmann constant [13]. Since Equation (7.1) only holds at temperature much smaller than Curie temperature, we only conduct linear curve fitting before $Ms(T)$ drops more than 80% of $Ms(0)$ to obtain more accurate Bloch coefficient A. When thickness is the only variable with Fe concentration fixed at 29%, Fig. 7.2(b) shows how the spin-wave stiffness constant increases with increasing thickness in a power-law-like trend. This power-law behavior originates from the linear relationship between $Ms(0)$ and inverse of film thickness as well as the power-law in Equation (7.2), consistent with analysis and experimental work done in Ref. [14], where the Bloch coefficient A is found to be inversely proportional to the sample thickness t. Therefore, according to Equation (7.2), a linear relationship between $D^{-3/2}$ and $1/t$ could be plotted, which is shown in Fig. 7.2 (c). Furthermore, the interception of the linear curve fitting gives an estimate spin-wave stiffness constant for bulk material of $Fe_{29}Pt_{71}$, which is about 130 $meV\text{Å}^2$. This number is close to the reported values for the Fe based alloys in the range from 110 $meV\text{Å}^2$ to 197 $meV\text{Å}^2$[15-16]. Meanwhile, when keeping the Fe_xPt_{100-x} sample thickness the same at 300 Å and considering Fe concentration as the only variable, we noticed that the spin-

wave stiffness constant shows upward-like trend with increasing Fe concentration (Fig. 7.2(d)). According to relevant proposed theories, the behavior of spin-wave stiffness constant at different impurity concentration in an alloy could be rather complicated [17], so more experiments and data might be required to show the relation between D and Fe concentration clearly.

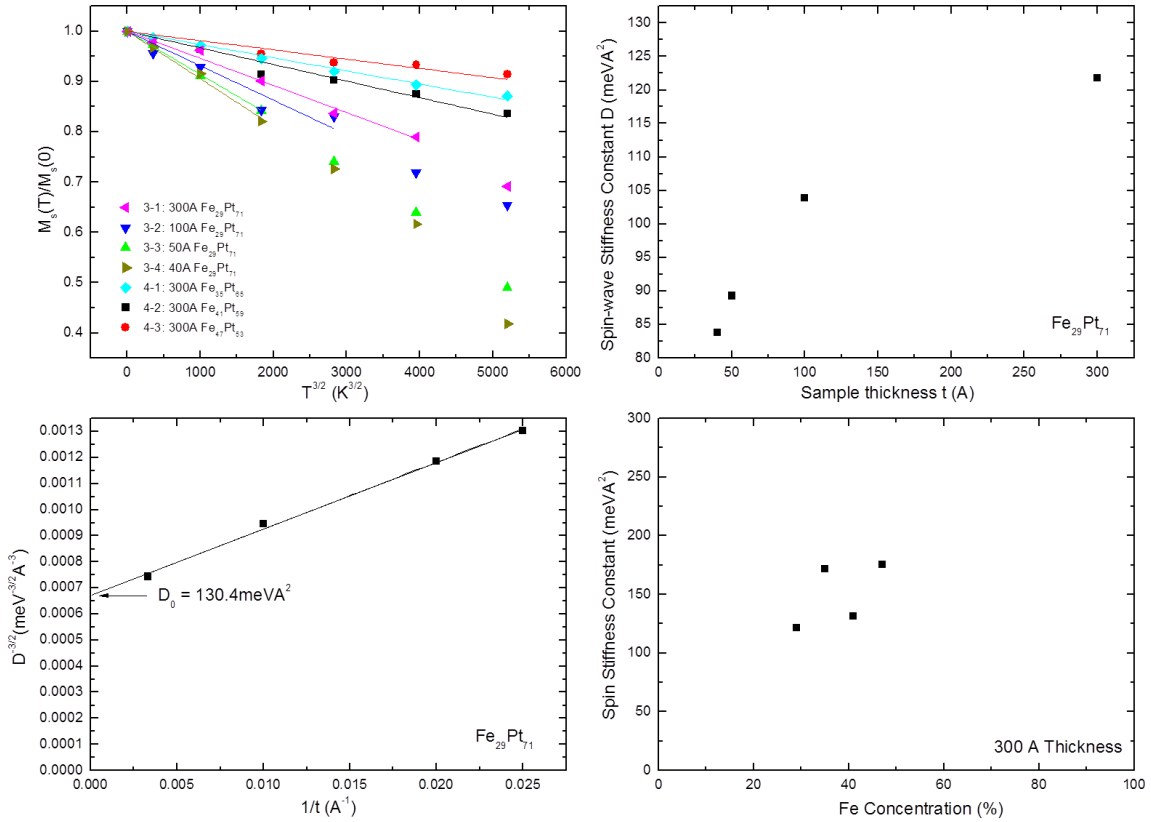

Fig. 7.2. (a) The magnetizations $Ms(T)$ normalized by $Ms(0)$ as a function of $T^{3/2}$; (b) Power law relationship between spin-wave stiffness constant D and sample thickness t of $Fe_{29}Pt_{71}$. (c) Linear relation between $D^{-3/2}$ and $1/t$, also the estimation of the spin-wave stiffness constant for $Fe_{29}Pt_{71}$ from the intercept of the fitted linear curve is indicated next to the arrow, $D_0 = 130.4\ meV\text{Å}^2$. (d) Spin-wave stiffness constant versus Fe concentration with constant thickness at 300 Å.

Next, we examine the transport properties of Fe-Pt AHE samples at room temperature by using standard four-probe measurement in the presence of a perpendicular

magnetic field. Fig. 7.3(a) shows that the longitudinal resistivity ρ_{xx} of Fe-Pt alloy steadily increases with reducing sample thickness t, following a $1/t$ behavior. These results are consistent with previous reports [2]. Also, at room temperature, we achieve the highest Hall slope of 16.6 $\mu\Omega \cdot \mathrm{cm/T}$ in 200 Å $Fe_{29}Pt_{71}$. This is close to the value reported in Ref. [5] and efficiently large for field sensing application at room temperature. Furthermore, we investigate the Hall angles (ρ_{xy}/ρ_{xx}) for samples with different thickness and Fe concentration combinations, which show the clear trend of increasing Hall angle with increasing thickness (Fig. 7.3(b)). The highest Hall angle at room temperature is about 0.05 for 300 Å $Fe_{35}Pt_{65}$, comparable with results reported by other groups in Pt-based system [18-20]. Also, it can be inferred that smaller longitudinal resistivity is related to larger Hall angle, both due to stronger spin-orbit interaction. At room temperature, in our thickest 300 Å AHE samples, $Fe_{35}Pt_{65}$ presents the largest Hall angle, while $Fe_{29}Pt_{71}$ presents the least, although it provides the largest Hall slope compared to Fe_xPt_{100-x} samples with higher Fe concentration.

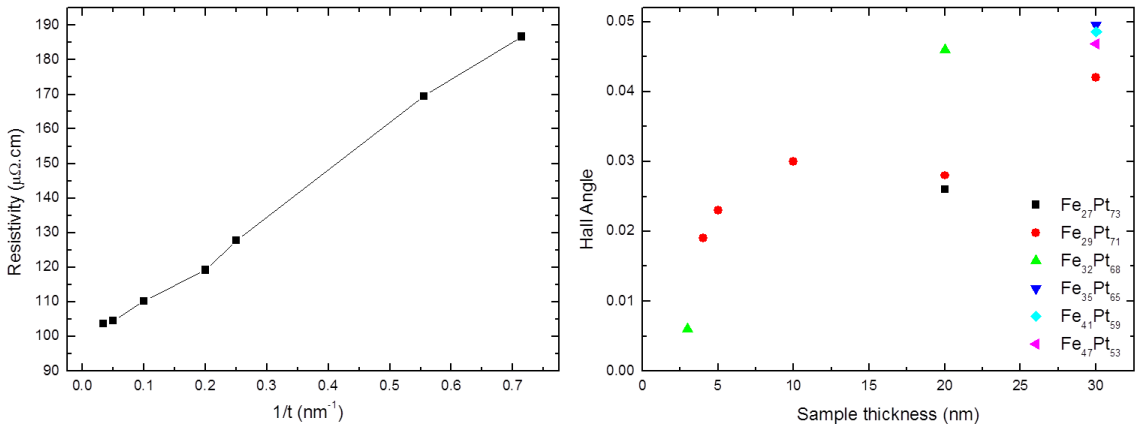

Fig. 7.3. (a) Inverse thickness dependence of the longitudinal resistivity ρ_{xx} of $Fe_{29}Pt_{71}$ at room temperature. (b) Hall angles of Fe_xPt_{100-x} for different sample thickness and Fe concentration combinations at room temperature. Highest Hall angle reaches 0.05 in 300 Å $Fe_{35}Pt_{65}$.

Meanwhile, since varying temperature could also introduce different transport properties in the Fe-Pt system, we further study the AHE for Fe_xPt_{100-x} samples by using the PPMS. Fig. 7.4 (a)-(d) shows Hall resistivity ρ_{xy} as a function of applied perpendicular magnetic field up to ±2T in 300 Å $Fe_{29}Pt_{71}$, 50 Å $Fe_{29}Pt_{71}$, 300 Å $Fe_{41}Pt_{59}$, and 300 Å $Fe_{47}Pt_{53}$ at varying temperature from 2 K to 300 K, as plotted in colors. The max ρ_{xy} either increases or decreases with reducing temperature, depending on Fe concentration, and the largest ρ_{xy} is 6.02 μΩ · cm, given in 300 Å $Fe_{41}Pt_{59}$ sample at 300 K.

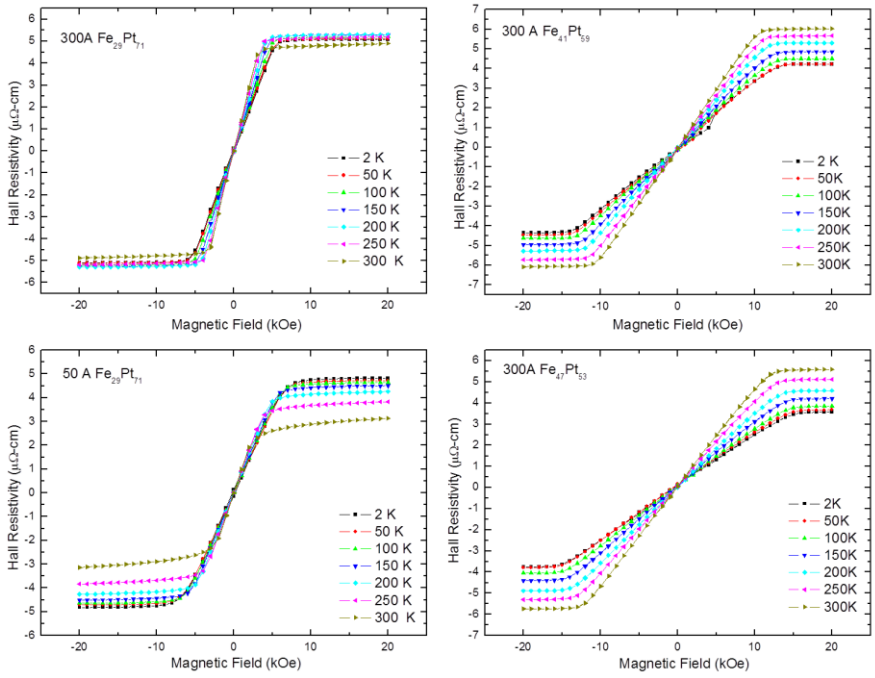

Fig. 7.4. (a)-(d) Hall resistivity (ρ_{xy}) measured in the range of ±2 Tesla magnetic field in 300 Å $Fe_{29}Pt_{71}$, 50 Å $Fe_{29}Pt_{71}$, 300 Å $Fe_{41}Pt_{59}$, and 300 Å $Fe_{47}Pt_{53}$ from 2 K to 300 K. Test current is 1 mA.

Different from Hall resistivity, the longitudinal resistivity ρ_{xx} in all Fe_xPt_{100-x} samples increases with increasing temperature, faster for thicker sample and slower for thinner sample as indicated in Fig. 7.5(a), all falling in the range of 85 μΩ · cm~130 μΩ ·

cm. The variance of ρ_{xx} from 2 K to 300 K enables us to study the correlation between Hall coefficient and resistivity which we will address later in this paper. Fig. 7.5(b) shows that the maximum Hall angle is about 0.05 at room temperature for 300 Å $Fe_{35}Pt_{65}$ and about 0.058 at 2 K for 300 Å $Fe_{29}Pt_{71}$. Meanwhile, 300 Å thickness sample tends to give the highest Hall angle at all temperatures when comparing with thinner $Fe_{29}Pt_{71}$ samples, consistent with our previous results in room temperature measurements shown in Fig. 7.3(b). According to this result, thicker Fe-Pt AHE samples tend to have larger Hall angle, while $Fe_{29}Pt_{71}$ gives relatively higher Hall angle below room temperature and $Fe_{35}Pt_{65}$ gives higher Hall angle only at room temperature. This implies that for magnetic field sensing applications, thicker Fe-Pt AHE sample is preferable and the Fe concentration should be chosen appropriately according to different temperature application.

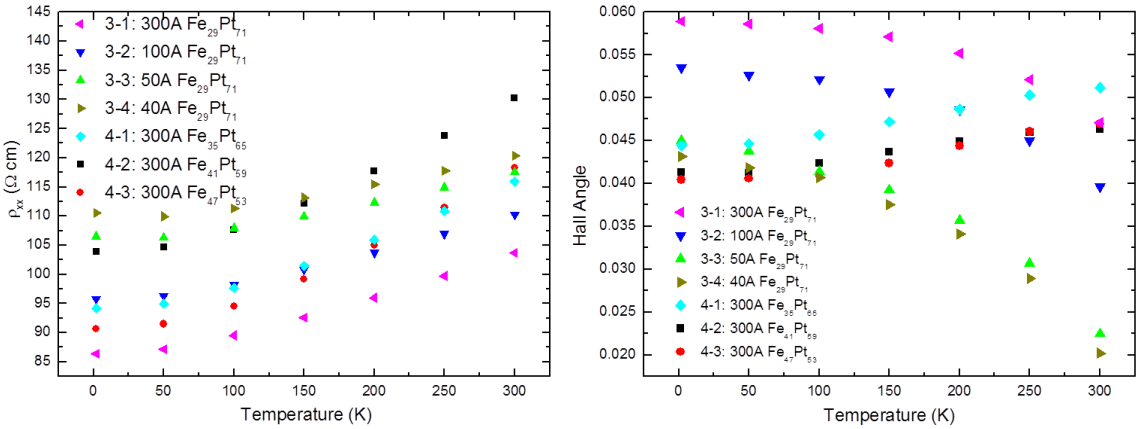

Fig. 7.5. (a) Longitudinal resistivity ρ_{xx} (b) Hall angle (ρ_{xy}/ρ_{xx}) as a function of temperature from 2 K to 300 K in Fe_xPt_{100-x} alloys of different thicknesses and Fe concentrations

Since the longitudinal resistivity ρ_{xx} varies with the temperature change in the region of 2 K to 300 K, we are able to further investigate in the correlation between either ρ_{xy} or Rs and ρ_{xx} in order to find the origin of the AHE effect in Fe-Pt system. Here,

however, the scaling law relationship between ρ_{xy} and ρ_{xx} is not suitable because the magnetization of Fe_xPt_{100-x} is inevitably reduced by as much as 40 % due to temperature changing as shown in Fig. 7.2(a) and the influence of changing magnetization on ρ_{xy} could not be neglected. As such, given the equation

$$\rho_{xy} = \rho_0 H + 4\pi R_s M_s \tag{7.3}$$

we could investigate the correlation between ρ_{xx} and $\rho_{xy}/4\pi M_s$, which gives Hall coefficient Rs considering that ρ_0 is relatively small in this system and can be neglected. Moreover, the plot of $Rs \sim \rho_{xx}^n$ is more preferred, where $n = 1$ indicates extrinsic skew scattering mechanism or $n = 2$ indicates extrinsic indicates side-jump/intrinsic Karplus-Luttinger (Berry phase) mechanism [21]. In Fig. 7.6, we plotted $Rs \sim \rho_{xx}$ in a log-log scale and fitted the plots by $Rs = C\rho_{xx}^n$. We noticed that all the exponents n are close to 2, consistent with previous result in the spin Hall effect study of Pt which proposed a side jump origin [22]. Different theories and experiments have also proposed and compared between intrinsic and extrinsic mechanisms in ferromagnetic films that leads to exponent of $n = 2$ [7, 21, 23]. Consistently, the longitudinal resistivity ρ_{xx} about 100 $\mu\Omega \cdot$ cm in all of our Fe_xPt_{100-x} samples falls in the regime far away from high-conductivity regime where skew scattering mechanism dominates. In out Fe-Pt system, the expected side-jump mechanism and Berry phase mechanism dominate as our sample is close to the good-conductivity regime ($\rho_{xx} \sim 1 - 100$ $\mu\Omega \cdot$ cm). Besides, we would like to emphasize that the exponent of $n = 2$ is found in our system instead of 1.6~1.8 which is commonly found in poor-conductivity regime ($\rho_{xx} > 100$ $\mu\Omega \cdot cm$), implying that the Fe-Pt system in this study is still out of the dirty metallic regime or the hopping regime. [7, 24-26]

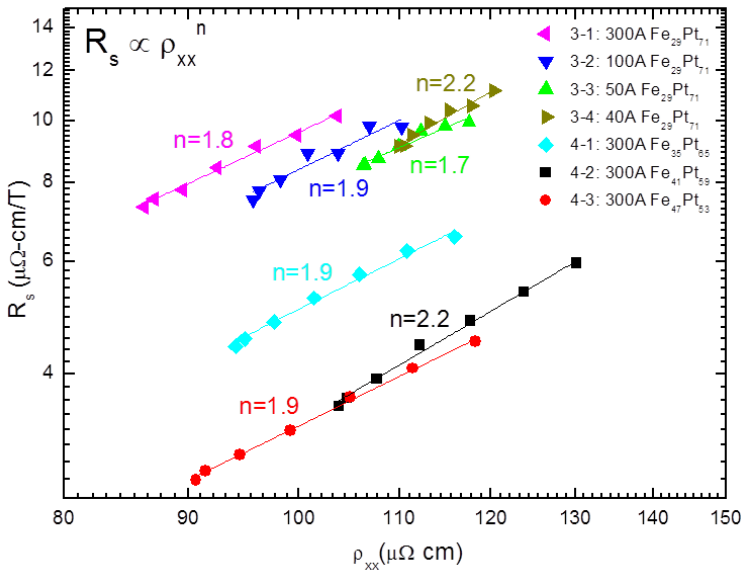

Fig. 7.6. Hall coefficient Rs as a function of longitudinal resistivity ρ_{xx} indicating $Rs \sim \rho_{xx}^2$ behavior.

7.3 Conclusion

To summarize, we systematically studied the AHE in Fe_xPt_{100-x} alloys at different magnetic concentration, thickness and temperature. Study of saturation fields as a function of the sample thickness has shown more significant changes in thinner sample, and we found the critical thickness of Fe-Pt thin-film with non-ferromagnetism from curve fitting at various temperature. This will be helpful for further studying the AHE in Fe-Pt system with thinner thickness. In addition, we investigated in the spin-wave stiffness constant at different Fe concentrations and thicknesses. A linear relationship between $D^{-3/2}$ and $1/t$ is found, and extracting from the intercept in the linear curve fitting provides an estimated spin-wave stiffness constant D of about $130\ meV\text{Å}^2$ in $Fe_{29}Pt_{71}$ alloy which is consistent with previous study in Fe-based alloys. Besides, the

Hall angle dependences on thickness and Fe concentration at different temperatures will provide useful guide for application, as Hall angle is directly related to the efficiency of converting longitudinal charge current to transverse Hall current. We found that thicker sample gives higher Hall angle at all temperatures, even though Hall angles are reduced by increasing temperature. Also, higher Fe concentration will inverse the trend of Hall angle as a function of temperature, leading to higher Hall angles at room temperature than low temperature. Moreover, study of the correlation between Rs and ρ_{xx}^{n} indicates both intrinsic mechanism and side-jump mechanism contribute in Fe-Pt AHE sample as all samples have given an average exponents of $n = 2$. This result is consistent with previous experimental work and proposed theories regarding ferromagnetic transition metals. Our study not only provides useful information for better understanding in the physics of AHE in the Fe-Pt system, but also is of significant importance for magnetic field sensing applications based on AHE thin-film sensors with the possibility of replacing semiconductor Hall sensors in the future.

References

1. X. W. Li, A. Gupta, and G. Xiao, Appl. Phys. Lett. 75, 713 (1999)
2. A. Neuweiler, B. Hofmann, and H. Kronmuller, J. Magn. Magn. Mater. 153 (1996) 28
3. N. Nagaosa, J. Sinova, S. Onoda, A. H. MacDonald, and N. P. Ong, Rev. Mod. Phys. 82, 1539 (2010)
4. T. Seki, Y. Hasegawa, S. Mitani, S. Takahashi, H. Imamura, S. Maekawa, J. Nitta

and K. Takanashi, Nat. Mater. 7, 125 (2008)

5. Edwards D M and Hill D J 1976 J. Phys. F: Met. Phys. 6 607
6. M. Becherer, J. Kiermaier, S. Breitkreutz, G. Csaba, X. Ju, J. Rezgani, T. Kießling , C. Yilmaz, P. Osswald, P. Lugli, D. Schmitt-Landsiedel, Solid-State Electron. 54 (9) , 1027 (2010)
7. C. W. Hicks, L. Luan, K. A. Moler, E. Zeldov, and H. Shtrikman, Appl. Phys. Lett. 90 133512
8. J. S. Lee, K. H. Ahn, Y. H. Jeong, and D. M. Kim, IEEE Trans. Electron Devices 43, 1665 (1996)
9. C. L. Canedy, X. W. Li, and G. Xiao, Phys. Rev. B 62, 508 (2000)
10. Y. Tian, L. Ye, and X. Jin, Phys. Rev. Lett. 103, 087206 (2009)
11. A.K. Panda, Ojaswini Mohanta, A. Basumallick, and A. Mitra, J. Magn. Magn. Mater. 322 (2010) 23
12. K. Ando, S. Takahashi, K. Harii, K. Sasage, J. Ieda, S. Maekawa, and E. Saitoh, Phys. Rev. Lett. 101, 036601 (2008)
13. I. Fergen, K. Seemann, A. v. d. Weth, and A. Schuppen, J. Magn. Magn. Mater. 242–245, 146 (2002)
14. L. Liu, C.-F. Pai, Y. Li, H. W. Tseng, D. C. Ralph, and R. A. Buhrman, Science 336, 555 (2012).
15. Y. Zhu and J. W. Cai, Appl. Phys. Lett. 90, 012104 (2007)
16. L. Liu, T. Moriyama, D. C. Ralph, and R. A. Buhrman, Phys. Rev. Lett. 106,

036601 (2011)

17. G. X. Miao and G. Xiao, Appl. Phys. Lett. 85, 73 (2004)
18. Q. Hao, S. Wang, W. Chen, G. Xiao, “Low frequency noise in Fe-Pt alloy-based thin-film Extraordinary Hall effect sensor”, (to be published).
19. G. Xiao and C. L. Chien, J. Appl. Phys. 61, 3308 (1987)
20. T. Golod, A. Rydh, and V. M. Krasnov, J. Appl. Phys. 110, 033909 (2011)
21. L. Vila, T. Kimura, and Y. C. Otani, Phys. Rev. Lett. 99, 226604 (2007)
22. W. R. Branford, K. A. Yates, E. Barkhoudarov, J. D. Moore, K. Morrison, F. Magnus, Y. Miyoshi, P. M. Sousa, O. Conde, A. J. Silvestre, and L. F. Cohen, Phys. Rev. Lett. 102, 227201 (2009)
23. D. Venkateshvaran, W. Kaiser, A. Boger, M. Althammer, M. S. Ramachandra Rao, S. T. B. Goennenwein, M. Opel, and R. Gross, Phys. Rev. B 78, 092405 (2008)
24. S. Sangiao, L. Morellon, G. Simon, J. M. De Teresa, J. A. Pardo, J. Arbiol, and M. R. Ibarra, Phys. Rev. B 79, 014431 (2009)
25. R. Karplus and J.M. Luttinger, Phys. Rev. 95, 1154 (1954)
26. H. Kontani, T. Tanaka, and K. Yamada, Phys. Rev. B 75, 184416 (2007)

Chapter 8

Low Frequency Noise in Fe-Pt Alloy Thin Film

8.1 Introduction

The Anomalous Hall Effect (AHE) in ferromagnetic metals and alloys due to spin-orbit interaction (SOI) has drawn great attention lately as a potential candidate for magnetic field sensing applications [1-2]. The sensitivity of such thin film sensors have been improved greatly to $1200V/AT$ [3] and even $12000V/AT$ [4] at room temperature, which are comparable to that of a commercial semiconductor Hall sensors without resorting to geometrical enhancement. The benefits of thin film sensor, typically Pt-based ferromagnetic alloy, include easy fabrication, high operation frequency and low noise performance. However, as different kinds of thin-film sensors are well studied at present especially in the aspect of increasing the sensitivity of Hall sensors, very few studies focus on the noise performance of such Hall sensors. In order to comprehensively characterize the performance and capability of the Hall sensors, we conduct the noise measurement together with the sensitivity of the AHE sensor to reveal its intrinsic sensing capability.

In this chapter, we focused on the Fe_xPt_{100-x} alloys at different Fe concentration and thickness, as experiments have found large Hall angel and Hall slope in Pt [5-7], which means potentially large sensitivity. Samples are prepared using Magnetron

sputtering technique [8] with single step lift-off lithography process; the transport properties are measured in the standard four-probe method in an out-of-plane magnetic field [9] and the noise spectrums are measured in a two-channel time cross-correlation method 10]. It is worth noting that the Noise-Equivalent Field, which is calculated as noise spectrum density (in the unit of $V/\sqrt{Hz}$) divided by sensitivity (in the unit of V/T), indicates the intrinsic capability that a Hall sensor could sense magnetic field assuming a signal-to-noise ratio of 1.

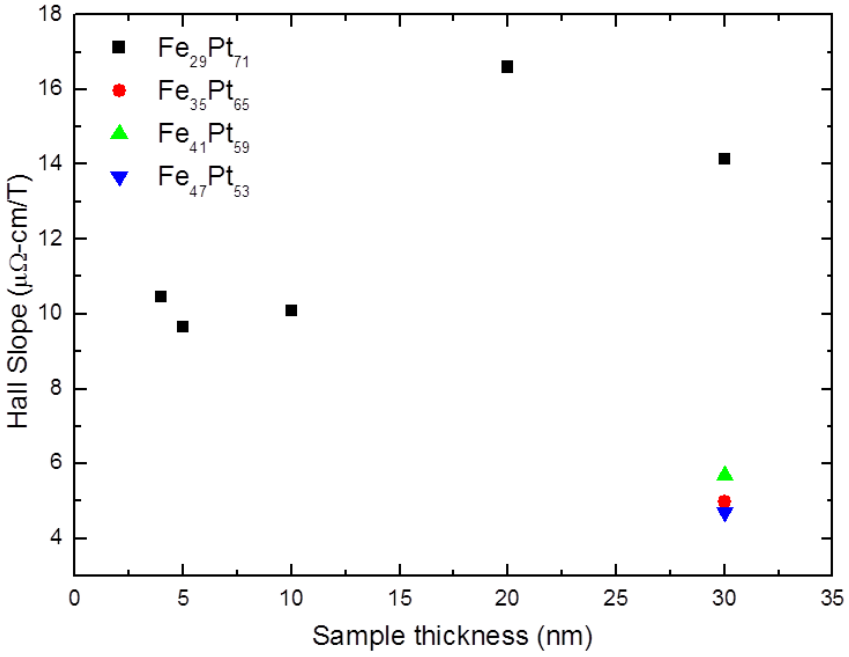

Fig.8.1. Hall slopes as a function of sample thickness and Fe concentration.

To obtain the sensitivity, four point Hall measurements are first performed and Hall slopes of Fe_xPt_{100-x} alloys with different thickness and Fe concentration are obtained and plotted in Fig.8.1. $Fe_{29}Pt_{71}$ samples have higher Hall slopes than Fe_xPt_{100-x} with other Fe concentrations and the highest Hall slope is 16.6 $\mu\Omega \cdot cm/T$ for 200 Å $Fe_{29}Pt_{71}$ at room temperature, which is consistent with previous report [9]. Best sensitivity in our AHE samples reaches 23.6 $V/A\,T$ at room temperature, which is one or two magnitude

smaller than that of reported semiconductor Hall sensors [11-12]. However, as it will be shown later, the low-noise performance of thin-film Hall sensor still makes it a good candidate for magnetic field sensing applications.

8.2 Experimental

The noise of a thin-film Hall sensor mainly includes the $1/f$ noise and the Johnson noise. Thus, noise spectrum can be simply characterized by three parameters: noise at 1Hz, the knee frequency f_{knee} and the noise floor (Johnson noise). Knee frequency separates the high frequency Johnson noise region and the low frequency $1/f$ noise region. Obviously, Hall voltage (signal) is proportional the input current, therefore the first problem is that whether increasing input current also magnifies the noise level and affects the signal-to-noise ratio. As we find out, the noise floor is independent of input current as long as the current density is not too large (typically$10^6 - 10^7\ A/cm^2$) to significantly heat-up the thin-film sample or even break it. Fig.8.2 (a) shows that the noise floor of 200 Å $Fe_{29}Pt_{71}$ sample remains constant while input current increases from 0.01 mA to 8.9 mA. This is understandable since Johnson noise is only determined by the resistance of the thin-film sample at room temperature:

$$S_V^{1/2} = \sqrt{4k_B RT} \tag{8.1}$$

, where R is the two-point Hall resistance (output resistance), k_B is Boltzmann constant and T is temperature. So in the high frequency region, Noise-Equivalent Field of the thin film sensor can be easily improved by increasing input current as long as it does not introduce over-heating and sample breakage.

However, this is not the case for the 1/f noise which increases significantly when the input current exceeds a critical value. As shown in Fig. 2(b), we are able to characterize the 1/f noise by examining the knee frequency f_{knee}. In this log-log scale plot, the two regions where knee frequency is almost independent of input current and where the power-law relationship between knee frequency and input current exists are separated by a critical current. Curve fitting on the scaling law behavior reveals an exponent of 1.88, close to 2, which reminds us that the $1/f$ noise has quadratic dependence on bias voltage:

$$S_V = \frac{\alpha V^2}{N f^\gamma} \tag{8.2}$$

and knee frequency is determined by

$$4k_B RT = \frac{\alpha V^2}{N f_{knee}^\gamma}, \quad f_{knee}^\gamma = \frac{\alpha V^2 / N}{4k_B RT} \tag{8.3}$$

Here, α is Hooge constant, exponent γ is an empirical number typically in the range of 0.9 to 1.4, and N is the number of fluctuators, which is proportional to the volume of Fe-Pt Hall bar. The quadratic relationship between knee frequency and input current beyond a critical value (Fig. 8.2(b)) implies that voltage V in Equation (8.2) results from the misalignment between both sides of the Hall bar and is proportional to the input current by a misaligned resistance R_0, which is typically about 0.3 Ω. Meanwhile, fitted exponent of 1.88 indicates the exponent γ is equal to 1.06, close to 1. We assume the number of fluctuators is about the number of charge carrier, which could be calculated from charge-carrier density ($3 \times 10^{27} m^{-3}$ as we calculated) extracted from normal Hall effect. From the 50 Å $Fe_{29}Pt_{71}$ Hall bar, we obtain the Hooge constant α to be 1.7×10^{-3}. With the knowledge that applying input current larger than a critical value will both significantly

increase the $1/f$ noise and the knee frequency, we always apply input current close to the critical number to optimize the Noise-Equivalent Field.

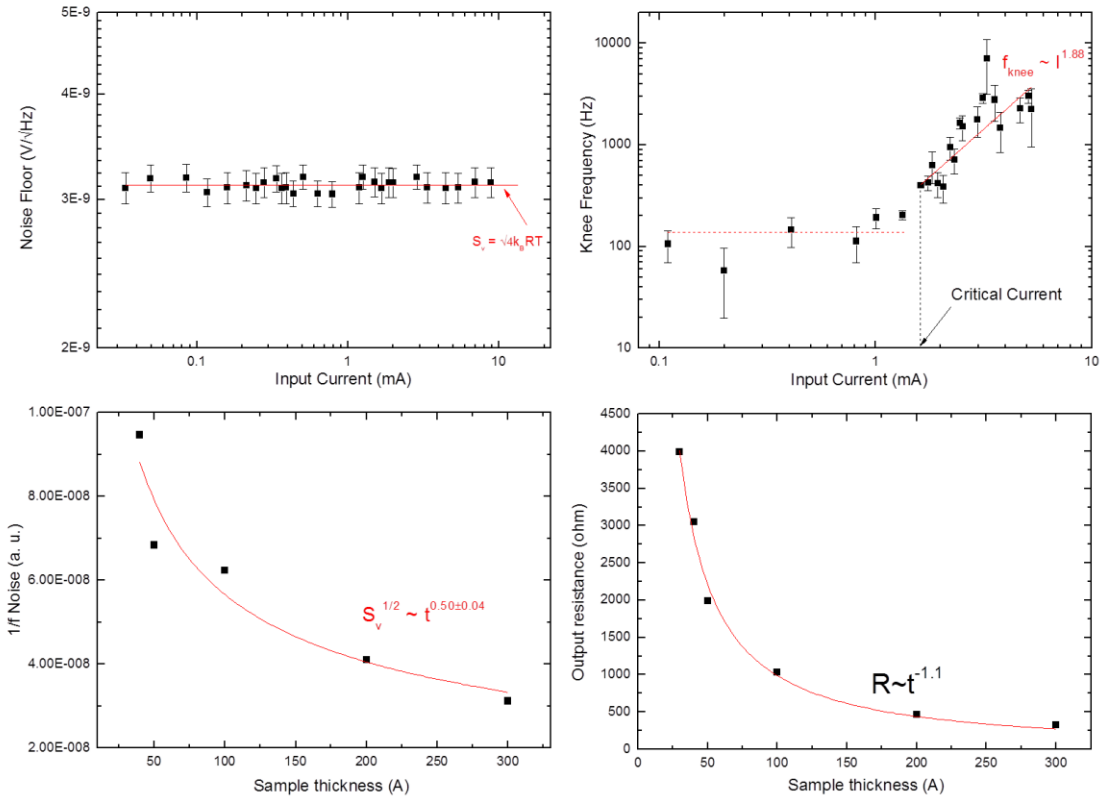

Fig.8.2.(a) Independence of Johnson noise in a Fe/Pt alloy on input current (red line indicates theoretical value); (b) Knee frequency as a function of input current with input current (red dash line is guided for eye, red solid line is exponential curve fitting); (c) 1/f noise as a function of sample thickness, indicating that $S_v^{1/2} \sim N^{-0.5} \sim t^{-0.5}$. (Data are averaged from 1/f noise power density at 1 Hz to 10 Hz); (d) Output resistance R as a function of sample thickness in a power law behavior with exponent close to -1.

If we focus on the region of small input current where 1/f noise is nearly constant as shown in Fig. 8.2 (b), we could examine the relationship between the 1/f noise and different sample thickness t. Curve fitting of the 1/f noise from frequency range of 1 Hz to 10 Hz (using $Fe_{29}Pt_{71}$ samples with 5 different thicknesses) indicates a relation of $S_v^{1/2} \sim t^{-0.50\pm0.04}$ in Fig. 8.2(c). According to Equation (8.2), 1/f noise is a function of the number of fluctuators N which is proportional to the volume of sample,

implying $S_v^{1/2} \sim N^{-0.5} \sim t^{-0.5}$. Hence, one can conclude the 1/f noise is only a function of $t^{-0.5}$ as long as the operating current does not exceed critical current. Therefore, determining the critical current for different Fe_xPt_{100-x} samples becomes important. We show in Fig. 3 that the critical current is proportional to the sample cross-section area, which is calculated as thickness times Hall bar width. Linear curve fitting demonstrates the critical current density of the $Fe_{29}Pt_{71}$ sample is about 1.7×10^6 A/cm^2, and this number is an intrinsic parameter of $Fe_{29}Pt_{71}$ alloy, independent of Hall bar dimension, input current and sample thickness.

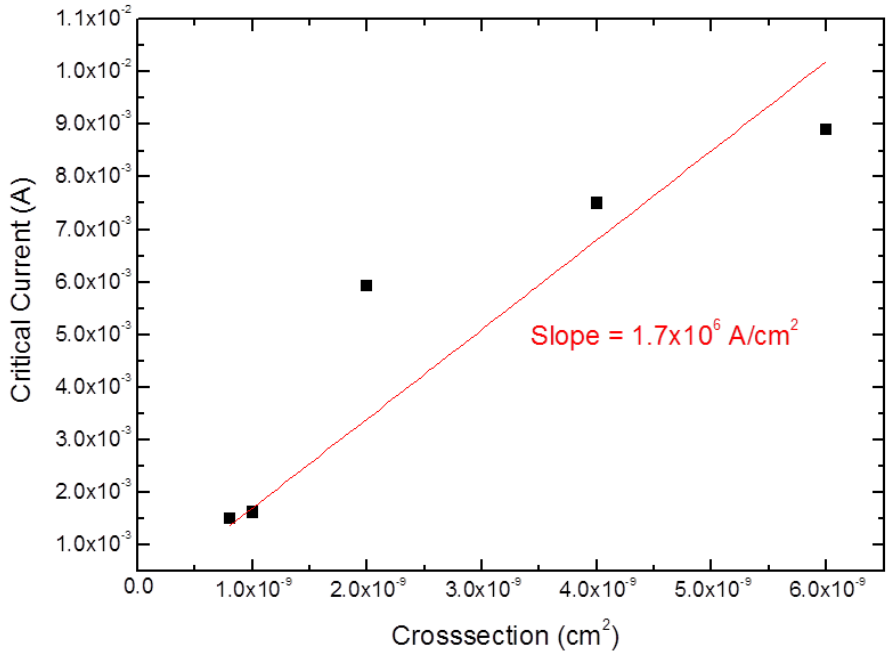

Fig.8.3. Linear relationship between critical current and the cross-section area for $Fe_{29}Pt_{71}$ AHE sample, giving a critical current density of $1.7 \times 10^6 A/cm^2$.

With the knowledge of the noise spectrum dependence on input current, we further examine the Noise-Equivalent Field of the Fe_xPt_{100-x} sample, which is calculated by noise level over sensitivity. As plotted in Fig. 8.4, the Noise-Equivalent Field of 40 Å $Fe_{29}Pt_{71}$ decreases with increasing input current, until the critical current of 1.86 mA is

applied, when Noise-Equivalent Field in low frequency region starts to increases even though the Noise-Equivalent Field in high frequency region keeps decreasing. This behavior results from the significantly increased 1/f noise that scales with squared input current I^2 as shown in Fig. 8.2 (b). Hence, with a well-defined critical current applied, the Noise-Equivalent Field of a thin-film Hall sensor is optimized, even though further increasing input current still enhances the output signal (but not the Noise-Equivalent Field). According to definition, the Noise-Equivalent Field can be calculated by

$$NEF = \frac{Noise\ level}{sensitivity} = \frac{Noise\ level}{R_s/_t \times I_c} \sim \frac{Noise\ level}{R_s \times J_c}, \tag{8.4}$$

where R_s is the Hall slope, t is the sample thickness, I_c is the critical current and J_c is the critical current density. Notice J_c is proportional to I_c/t according to the results from Fig. 8.3. Better Noise-Equivalent Field can be achieved at lower noise level and larger Hall slope assuming a constant critical current density. In the high frequency region, noise level is Johnson noise which depends on the two-point output resistance R so Equation (8.4) can be rewritten as

$$NEF_{high\ f} \sim \frac{\sqrt{4k_B RT}}{R_s \times J_c} \tag{8.5}$$

To study the relationship between output resistance and sample thickness, we plotted and fitted the curve in Fig. 8.2(d). Accordingly, the output resistance R is a power-law function of thickness t with the exponent of *-1.1.* Hence, we conclude that Johnson noise level is proportional to $t^{-0.5}$ and Equation (8.4)-(8.5) can be further simplified as

$$NEF_{high\ f} = \frac{Const}{R_s \times t^{1/2}} \tag{8.6}$$

Since the Hall slope is demonstrated to be achieved at maximum for $Fe_{29}Pt_{71}$ alloy, so thicker $Fe_{29}Pt_{71}$ sample is more preferred for better (smaller) Noise-Equivalent Field in

high frequency application. According to Fig.8.1, the Hall slopes R_s in $Fe_{29}Pt_{71}$ samples of all thicknesses are in the same order of magnitude; hence the Noise-Equivalent Field of $Fe_{29}Pt_{71}$ alloy in high frequency range should be proportional to $t^{-0.5}$. This result is demonstrated by the plots in Fig. 8.5(a), and fitted exponent is -0.54, close to -0.5. The lowest Noise-Equivalent Field is achieved in 300 Å $Fe_{29}Pt_{71}$ about $0.05\ uT$ at 1k Hz.

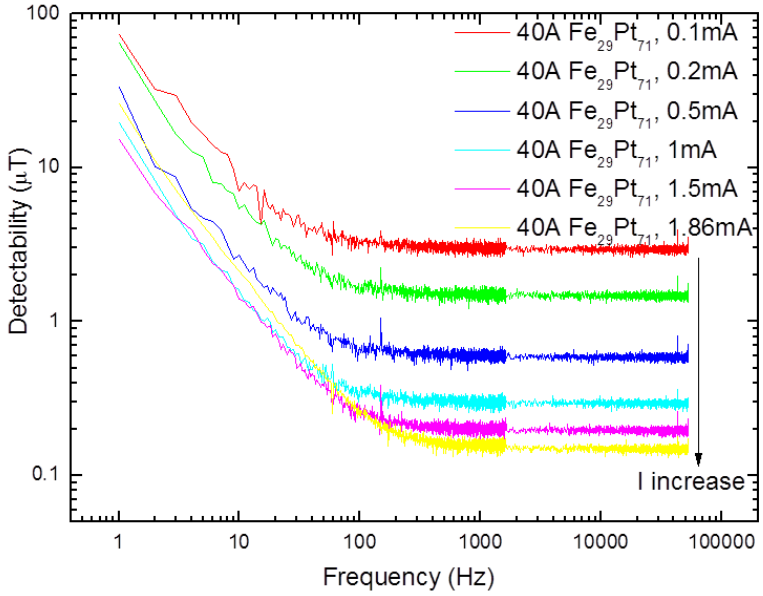

Fig. 8.4 Noise-Equivalent Field as a function of input current, showing an input current of 1.5 mA optimize the performance.

Similarly, in the case of low frequency region where $1/f$ noise dominates, Noise-Equivalent Field could be expressed as

$$NEF_{low\ f} = Const' \times \frac{{}^{1}/_{f}\ noise\ level}{R_s} \tag{8.7}$$

According to above analysis and Fig. 8.2(c), $1/f$ noise is a function of sample thickness in a power-law behavior of $S_v^{1/2} \sim t^{-0.5}$ as long as the applied current is below the critical value. Therefore, the Noise-Equivalent Field $D_{low\ f}$ of AHE sample is a function of $t^{-1/2}$, which means thicker sample provides better Noise-Equivalent Field. Lower $1/f$

noise is preferable not only because it enhances the low-frequency Noise-Equivalent Field, it also reduces the knee frequency and thus broadens the high-frequency region where the noise performance is much better compared to low-frequency region. Fig. 8.5(b) indicates the Noise-Equivalent Field as a function of sample thickness, and the fitted exponent is -0.62, close to theoretically calculated -0.5. The best Noise-Equivalent Field at low frequency region is achieved in 300 Å $Fe_{29}Pt_{71}$, which is about 7 uT at 1 Hz. In addition, because of lower hall slopes, other AHE samples with higher Fe concentrations present much higher Noise-Equivalent Fields (Fig. 8.5(a)(b)), which is consistent with our analysis.

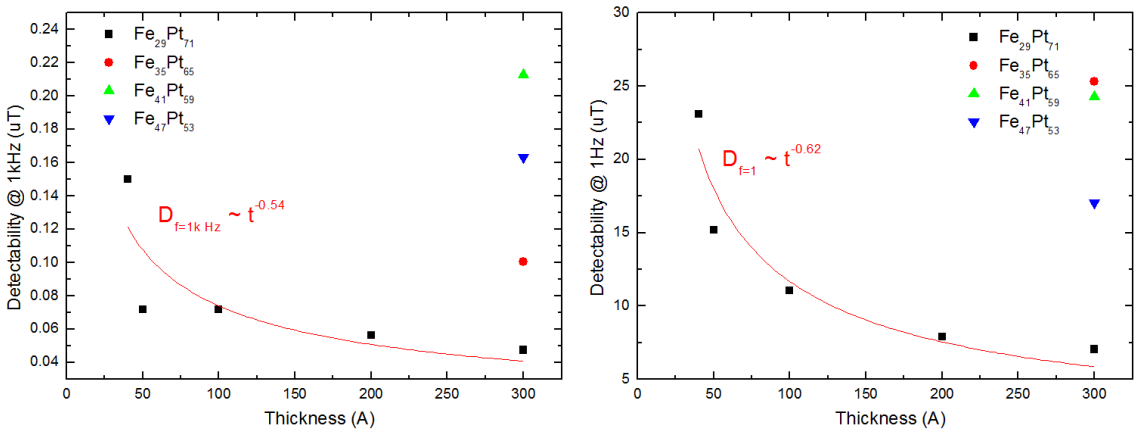

Fig.8.5 (a),(b) Noise-Equivalent Field as a function of thickness at 1k Hz and 1 Hz, respectively. Curve fitting indicates the dependence of Noise-Equivalent Field on thickness t is a power law with exponent close to -0.5 for $Fe_{29}Pt_{71}$ AHE Hall sensor.

Furthermore, we examine the influence of external magnetic field on the noise performance of the AHE samples. DC perpendicular magnetic field ranging from 0 Oe to 3500 Oe is applied seperately on 50 Å $Fe_{29}Pt_{71}$ (saturation field is about 3600 Oe) and noise spectrum is measured at input current well below critical current. Fig. 6 shows that the Johnson noise does not change with applied magnetic field while the knee frequency and the noise level at 1 Hz increases with magnetic field, indicating that perpendicular

external magnetic field increases the $1/f$ noise but not the Johnson noise. Further curve fitting analysis shows that noise at 1Hz increases with magnetic field in a scaling law of $S_v^{1/2}(f=1)=(\frac{\alpha V^2}{N})^{1/2}\sim B^{0.14}$, and the knee frequency increases with the magnetic field in a scaling law of $f_{knee}\sim B^{0.29}$. Notice that the knee frequency f_{knee} can be extracted from Equation (8.3), and is proportional to $(\frac{\alpha V^2}{N})^{1/\gamma}$. Therefore, we obtain the exponent γ to be 0.97, close to 1 and consistent with the γ extracted from above knee frequency vs current curve fitting. Also we conclude that the term $\frac{\alpha V^2}{N}$ is proportional to $B^{0.29}$. Since the input current is well below the critical current, we attribute the 1/f noise increase to the changes of the number of fluctuators N in the presence of an external magnetic field, in a scaling-law behavior of $N\sim B^{-0.29}$. This is understandable because the applied perpendicular magnetic field is smaller than the saturation field, larger field leads to less possibility of the aligned spin to flip and thus the less number of fluctuators N.

When comparing with the commercial semiconductor Hall sensor which suffers from the Random Telegraph Noise (RTN) [13] as larger input current increases noise in scale of increased sensitivity, the thin-film sensor benefits from larger input current which only increases signal output but not the noise level as long as input current is chosen optimally near below critical current. Therefore, even the sensitivity of AHE thin-film sensors are one or two orders of magnitude lower than that of semiconductor Hall sensor, it is possible that AHE sensor could outperform in terms of Noise-Equivalent Field. In Fig. 8.7 (a), we compared the noise spectrum of a typical semiconductor Hall sensor with one of our Fe/Pt Hall sensors. The semiconductor Hall sensor behaves an increased noise level in scale of increasing applied current, while the 200 Å $Fe_{29}Pt_{71}$ Hall

sensor indicates one or two orders of magnitude lower noise. Hence, even though the semiconductor Hall sensor has higher sensitivity as 173 $V/A\ T$ while 200 Å $Fe_{29}Pt_{71}$ Hall

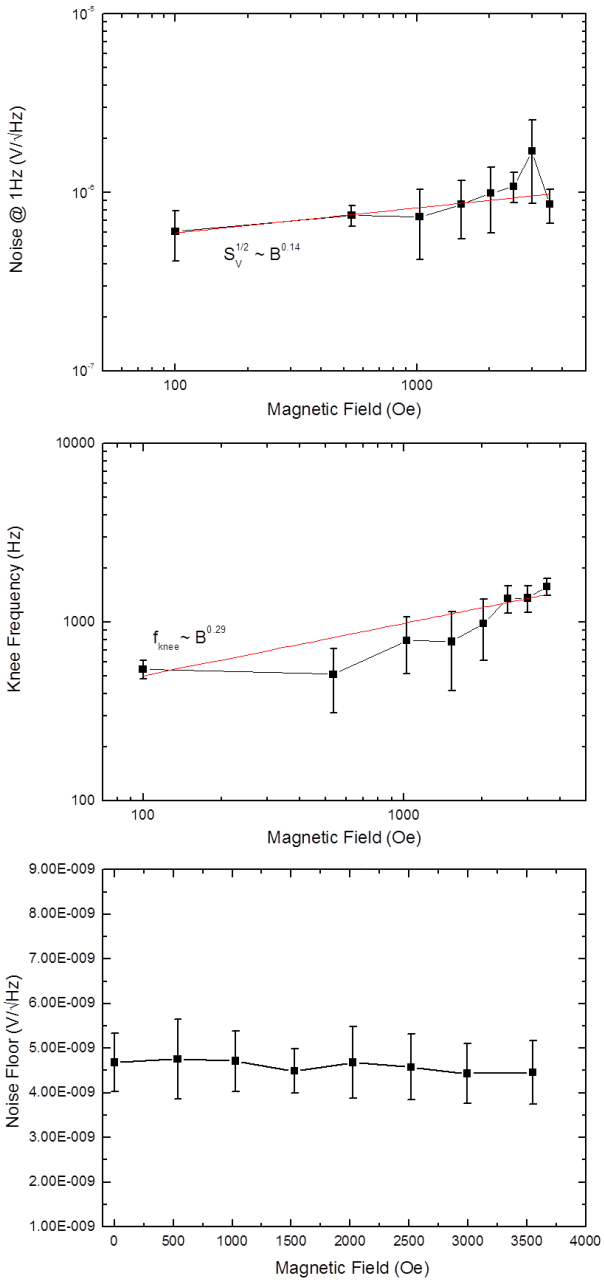

Fig.8.6. (a) noise floor, (b) knee frequency and (c) noise at 1 Hz as a function of applied magnetic field perpendicular to AHE sample surface. Johnson noise is independent on magnetic field; knee frequency and noise at 1 Hz are in a scaling law with magnetic field with the exponents of 0.14 and 0.29, respectively.

sensor has only 8.2 $V/A\,T$ sensitivity, the Noise-Equivalent Field comparison between the two still indicates a better performance for thin-film sensor in the frequency range between 3 Hz to 1500 Hz. According to previous analysis, the Noise-Equivalent Field of thin-film Hall sensor could be improved (but not too much due to the $t^{-1/2}$ scaling law behavior) using thicker sample.

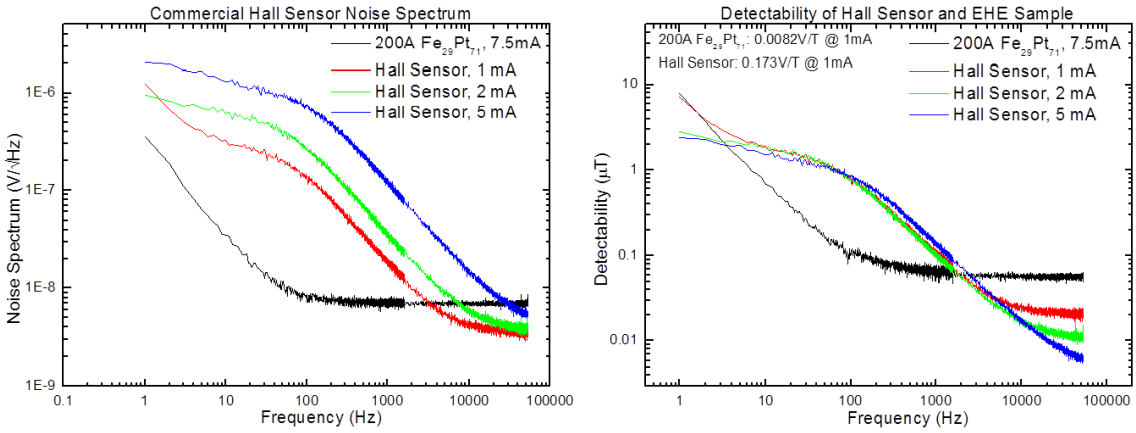

Fig.8.7.Comparison of the (a) noise spectrum and (b) Noise-Equivalent Field between 200 Å $Fe_{29}Pt_{71}$ AHE Hall sensor and commercial semiconductor Hall sensor indicates that AHE Hall sensor outperforms the semiconductor Hall sensor in frequency range of 3 Hz to 1500 Hz.

8.3 Conclusion

In conclusion, we proposed a more comprehensive parameter, Noise-Equivalent Field that better describes the capability and performance of Hall sensors than the biased parameter like sensitivity. As a function of noise level and sensitivity, Noise-Equivalent Field depends on the noise performance, sample thickness, Hall slope and critical current density. Based on our analysis, Noise-Equivalent Field of thin-film Hall sensor is only the function of sample thickness for a given Hall slope and intrinsic critical current

density. Also, as Noise-Equivalent Field depends linearly with inverse of Hall slope, our $Fe_{29}Pt_{71}$ tends to perform better in terms of Noise-Equivalent Field due to relatively large Hall slope at 29% Fe concentration, which agrees with results in previous work [9]. The best Noise-Equivalent Field in our Hall sensors is $0.05\ uT$ at 1k Hz and $7\ uT$ at 1 Hz. In the presence of external magnetic field that applied perpendicular to Hall sensor, we found out that magnetic field tend to increase $1/f$ noise in a scaling law because of the decreased number of fluctuators in the Fe/Pt system. When comparing with the semiconductor Hall sensor, our 200 Å $Fe_{29}Pt_{71}$ AHE sensor outperforms in the frequency range 3-1500Hz. Due to the easy fabrication procedure and low noise level, we believe that thin-film Hall sensor is also a promising candidate for the low field sensing application. Further improvement could be achieved by finding the maximum Hall slope in thicker AHE samples.

References:

1. C. L. Canedy, X. W. Li, and G. Xiao, Phys. Rev. B **62**, 508 (2000)
2. W. Zhang, Q. Hao, and Gang Xiao, Phys. Rev. B **84**, 094446 (2011)
3. J. S. Lee, K. H. Ahn, Y. H. Jeong, and D. M. Kim, IEEE Trans. Electron Devices **43**, 1665 (1996).
4. N. Haned and M. Missous, Sensors and Actuators A **102**, 216 (2003)
5. Y. M. Lu, J. W. Cai, H. Y. Pan, and L. Sun, Appl. Phys. Lett. **100**, 022404 (2012)
6. L. Liu, T. Moriyama, D. C. Ralph, and R. A. Buhrman, Phys. Rev. Lett. **106**, 036601 (2011)

7. K. Ando, S. Takahashi, K. Harii, K. Sasage, J. Ieda, S. Maekawa, and E. Saitoh, Phys. Rev. Lett. **101**, 036601 (2008)

8. S. Shimizu, K. S. Takahashi, T. Hatano, M. Kawasaki, Y. Tokura, and Y. Iwasa, Phys. Rev. Lett. **111**, 216803 (2013)

9. S. L. Zhang, Y. Liu, L. J. Collins-McIntyre, T. Hesjedal, J. Y. Zhang, S. G. Wang and G. H. Yu, Sci. Rep. **3**, 2087

10. G. X. Miao and G. Xiao, Appl. Phys. Lett. **85**, 73 (2004)

11. Y. Zhu, J. W. Cai, Appl. Phys. Lett. **90**, 012104 (2007)

12. T. Seki, Y. Hasegawa, S. Mitani, S. Takahashi, H. Imamura, S. Maekawa, J. Nitta and K. Takanashi, Nat. Mater. **7**, 125 (2008)

13. C. W. Hicks, L. Luan, K. A. Moler, E. Zeldov, and H. Shtrikman, Appl. Phys. Lett. **90**, 133512 (2007)

Chapter 9

MgO-based Magnetic Tunnel Junction: Magneto-transfer Curve Study

9.1 Introduction

Over the past decade, significant effort has been dedicated to the development of devices and technologies based on discoveries from the emergent field of spin-based electronics (spintronics) [1-3]. With the discovery of large magnetoresistance (MR) effects at room temperatures, magnetically-engineered thin-film devices were studied extensively as the basis for advanced magnetic sensors and high-density non-volatile magnetic random access memories (MRAMs) [4-5]. Among all the devices developed to date, magnetic tunnel junctions (MTJs) have generated perhaps the greatest interest due to their significant tunnel magnetoresistance (TMR). Consisting of layered heterostructures with two ferromagnetic layers separated by an insulating layer, the comparatively simple design of an MTJ lends itself well to potential applications in the next-generation of spintronic devices [6-7]. Moreover, aside from their capacity for practical applications such as magnetic field sensing, MTJs are also attractive as a platform for advanced studies of fundamental spin-dependent tunneling effects and transport properties [8]. At present, one of the defining factors for both practical and basic applications of MTJs is the upper limit of the TMR ratio. Thus, the attainment of the maximal value possible for the TMR ratio is of paramount importance. Recent studies

have demonstrated that the use of a highly-textured MgO barrier significantly increases the TMR ratio due to coherent tunneling processes [9-11]. Thus, we have focused solely on MgO-based MTJs.

More importantly, the development of MTJ is a demand for integration with Giant Spin Hall Effect solids which was studied in great details as described in Chapter 4-6, where it was the AHE that has been utilized to sense the Giant Spin Hall Effect. The MTJ as a sensor or a memory unit will perform even better in device integration and development because of the large MR and simpler three-terminal design. Therefore, we also put great effort into the research of MTJ and its electron transport measurement which will be detailed in this chapter.

We have divided our efforts to improve the performance of MgO-based MTJs into two areas. First, the parameters and techniques to fabricate the MTJ multilayer structure, including MgO-barrier thickness, free layer structure and thickness, deposition pressure, and annealing temperature, were analyzed to systematically optimize the devices. Second, comprehensive methods for measuring the intrinsic magnetic properties were developed. We focused on maximizing the low-field magnetic sensitivity, the free layer and pinned layer coupling, and the signal-to-noise ratio. For example, it has been proved that a series of MTJs could lower the noise floor and improve the sensitivity in comparison to a single MTJ [12].

To extract the magnetic parameters of our devices, we developed a series of novel measurement methods. Traditionally, the most basic magnetoresistive transfer curve is the so-called “linear transfer curve” (LTC). The resistance is measured as a function of magnetic field along a particular axis. From an LTC, one can readily obtain the magnetic

coercivity (H_C). But this method cannot determine either the free layer anisotropy orientation and strength or the pinning direction and strength of the pinned layer. Without prior knowledge of the pinning direction, this method cannot even measure the total magnetoresistance precisely. Another commonly-used measurement, the so called "asteroid curve", is helpful in providing information about the free layer but is not able to determine the pinned layer properties [13]. Thus, a more complete magnetic characterization technique was developed, based on earlier work from Saffron, et al. [13].

Here, we will introduce the new technique of magnetoresistive transfer curve characterization via the manipulation of a two-dimensional external magnetic field. We will use computational simulation and analysis to extract a plethora of magnetic parameters for both the pinned layer and the free layer of MTJ structures with different internal magnetic configurations.

9.2 Magnetoresistive Transport Curve Study

In the layered structure of our fabricated MTJ, (as shown in Fig. 9.1), :Substrate/$Co_{50}Fe_{50}$(30)/$Ir_{22}Mn_{78}$(180)/$Co_{50}Fe_{50}$(30)/Ru(8.5)/$Co_{40}Fe_{40}B_{20}$(30)/ MgO(t)/$Co_{40}Fe_{40}B_{20}$(30)/Ta(3)/Conetic($Ni_{77}Fe_{14}Cu_5Mo_4$)(400) (numbers in parenthesis in Angstroms), the most critical layers are the MgO barrier and the two adjacent ferromagnetic electrodes. All layers are deposited sequentially using a high vacuum sputtering system [14-16]. The $Co_{50}Fe_{50}$ layer acts as a seeding layer to improve the deposition of the $Ir_{22}Mn_{78}$ antiferromagnetic (AFM) layer [17]. The AFM layer ensures the adjacent ferromagnetic layer is well-pinned over the operating temperature of the

device via an exchange bias coupling mechanism. To further enhance the stability of the device, a composite tri-layer structure of CoFe/Ru/CoFeB, referred to as the synthetic anti-ferromagnetic (SAF) layer, is used instead of the more-common single, thin ferromagnetic layer. The increased exchange bias strength and magnetic stability of this tri-layer is due to the coupling of the two magnetic layers through the Ru spacer via short-range RKKY interactions. After annealing, the combination of the $Ir_{22}Mn_{78}$ layer and SAF layer is sufficiently strong as a foundation for a pinning layer over the normal operating magnetic field range (approximately a few hundred Gauss) of an MTJ.

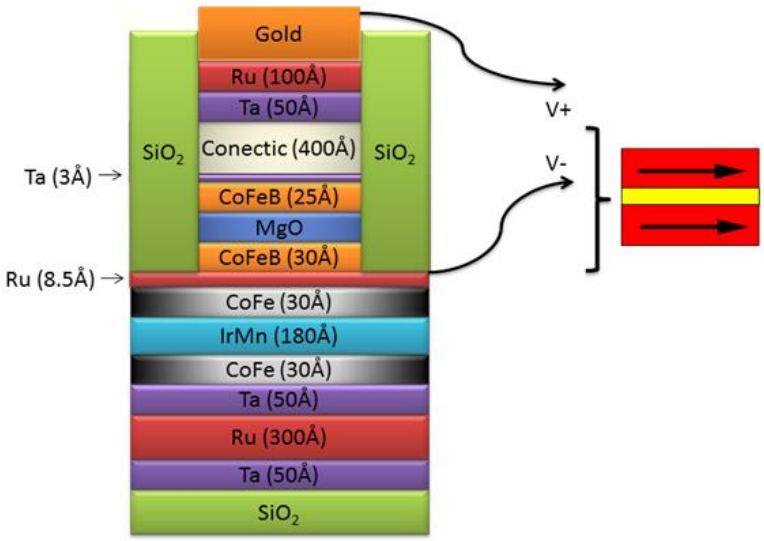

Fig.9.1 Schematic drawing of an MgO-based magnetic tunnel junction. Arrows indicate the orientation of the magnetization of the free layer and the pinned layer.

The most critical process in the generation of an MJT stack is the deposition of a pinhole-free and smooth MgO layer, whose thickness (t) can be selectively varied from 10 to 22 Å. This highly-oriented MgO barrier with a (001) texture is a prerequisite for large TMR ratios [18]. The free layer in our MTJ consists of a CoFeB/Ta/Conetic stack. CoFeB is the primary component necessary for magneto-tunneling, while the Conetic

layer serves to make the free layer magnetically "softer", thereby increasing its susceptibility and response to an external magnetic field [19]. The entire MTJ multilayer stack was sputtered in a single run under a high vacuum (~10^{-8} Torr) before wet processing and standard high-temperature magnetic annealing. The magnetic annealing process determines the pinning direction of the pinned layer. It allows an MTJ sample to be made in one of the two commonly-used spin configurations. In the "switch" configuration, the pinning direction is parallel to the free layer anisotropy direction. In the "sensor" configuration, the two directions are orthogonal to each other.

9.2.1 Magneto-transfer Curve Measurements

Linear Transfer Curve and Circular Transfer Curve

The linear transfer curve is the most common magnetoresistive transfer curve measurement used to extract magnetic information about a magnetic device. It is obtained by measuring the resistance of the device versus a uniaxial external magnetic field (Fig. 9.2). Consider the "switch" configuration. As shown in Fig. 9.2, when the magnetic field is along the anisotropy orientation, the free layer magnetization is either anti-parallel or parallel to the pinning direction, giving rise to two resistance values: R_{ap} and R_p. From the linear transfer curve, the R_{ap}, R_p, and coercivity H_C can be extracted directly, while magnetoresistance and sensitivity can be calculated indirectly. The linear transfer curve also serves as basis for further magnetic property analyses, including plotting asteroid curves and sensitivity mapping. For the case shown in Fig. 9.2, H_C is 14.5 Oe, R_{ap} is 20.376 kΩ, and R_p is 8.717 kΩ.

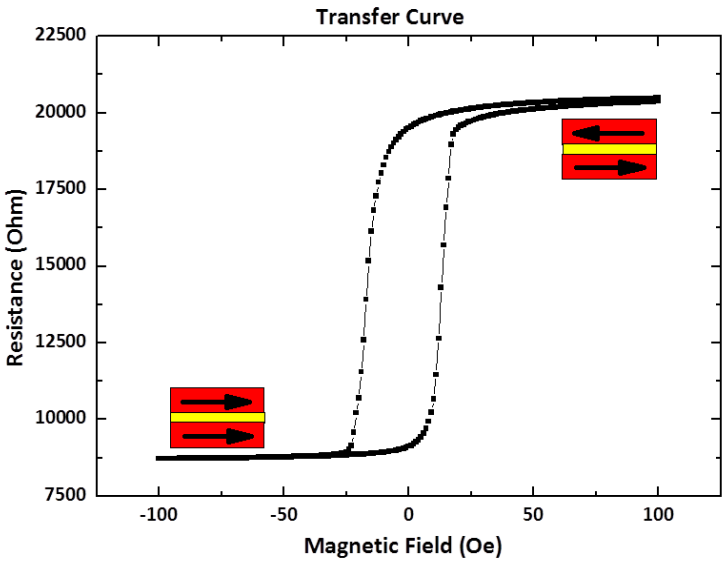

Fig. 9.2 Linear transfer curve of an MTJ sample. The anti-parallel state and the parallel state are achieved by applying 100 Oe and -100 Oe magnetic fields, respectively. In both cases, only the free layer is responding to external magnetic field.

An angle-dependent resistance measurement, the "circular transfer curve", is performed by rotating the in-plane magnetic field 360° with constant magnitude (Fig. 9.3). During the rotation, the free layer magnetization correlates to the magnetic field in two dimensions. For a large magnetic field enough to overcome the free layer anisotropy, the magnetization will rotate with the field, giving a nearly sinusoidal resistance curve. Such a curve is shown in Fig. 3. R_{ap} and R_p are 20.638 kΩ and 8.672 kΩ, respectively. Note that both the linear transfer curve and the circular transfer curve are taken from the same sample. The differences between the two measurements arise from the fact that the linear transfer curve, although assumed to be taken along the free layer anisotropy orientation, cannot be guaranteed to be perfectly aligned so as to obtain precise values for R_{ap} and R_p. In contrast, rotating the magnetic field will always sample the two positions where the free layer magnetization is parallel and anti-parallel to the pinning direction as

long as the amplitude of the magnetic field is sufficiently large. Consequently, a more precise magnetoresistance can be obtained by the equation

$$MR = \frac{R_{ap} - R_p}{R_{ap}}. \tag{9.1}$$

In the case shown in Fig. 9.3, this relation yields an MR ratio of 138%. As predicted, the free layer magnetization follows the direction of the magnetic field; the two positions on the curve with extreme resistance values denote the pinning direction of pinned layer. In Fig. 9.3, the two corresponding angles are 177° and 357°. So, the pinning direction is 177°, where R_p is achieved.

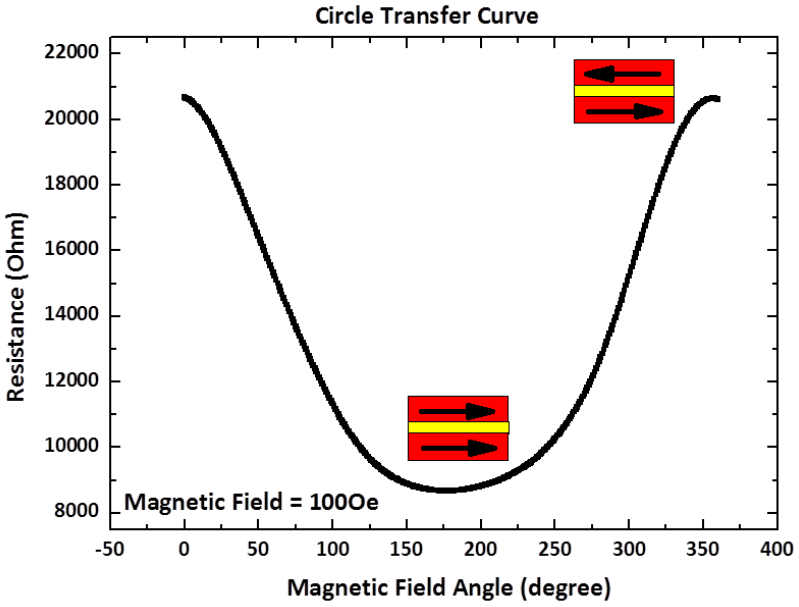

Fig. 9.3 Circular transfer curve of an MTJ. By fixing the magnetic field magnitude at 100 Oe and rotating the field 360º in the sample plane, the anti-parallel and the parallel states are observed at approximately 177º and 357º, respectively.

Remnant Resistance Curve

A magnetic particle in the "switch" configuration has two energy minima parallel to the pinning direction, corresponding to two different resistance values. Thus, its free layer anisotropy direction can be determined by another magnetoresistive transport curve measurement called the "remnant resistance curve" (RRC) [20]. This curve is obtained by applying a large magnetic field (sufficient to saturate the free layer magnetization) and then reducing the field to zero before measuring the angularly-dependent resistance. Because of the free layer anisotropy, the magnetization will parallel or anti-parallel to the anisotropy direction after removing the external field. According to the Stoner-Wohlfarth (S-W) model, the free layer magnetization favors the direction that forms a minimum

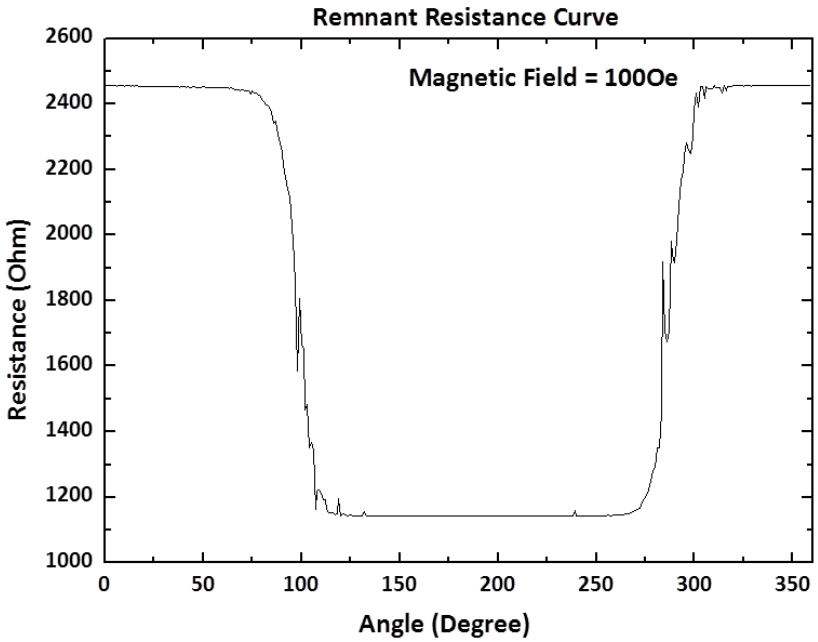

Fig. 9.4 Plots of a circular remnant resistance curve, which is obtained by relaxing a 50 Oe magnetic field and measuring the resistance for all angles within the sample plane. The locations of the two quasi-asymptotic features indicate the angles perpendicular to the free-layer anisotropy orientation. Averaging the two angles gives the anisotropy direction.

angle with the magnetic field. Thus, for all angles, there will be only two states that are stable leading to two resistance values with sharp transitions between them (Fig. 9.4).

In the example curve given in Fig. 9.4, the two angles where the resistance drops dramatically, about 100° and 280°, denote the angles perpendicular to the anisotropy direction. Therefore, by averaging these two values, we can get the anisotropy angle, 190°, which agrees with our fabrication process result (180°) allowing for 10° variance due to probable sample patterning offsets.

Asteroid Curve

Theoretically, for a single domain magnetic particle, an asteroid curve based on the S-W model is determined by minimizing the free energy equation

$$G\,(\theta) = -HM\cos(\theta - \theta_H) + K_a sin^2(\theta - \theta_a) - H_{0x}Mcos\theta - H_{0y}sin\theta \qquad (9.2)$$

with respect to the magnetic moment M, the free layer anisotropy strength K_a and direction θ_a, and the internal offsets H_{0x} and H_{0y} (See Fig. 9.5) [21]. Within the area enclosed by the asteroid curve, four energy extremes can be achieved, including two maxima and two minima. Outside the asteroid, there are two energy extremes, one maximum and one minimum. Thus, the asteroid curve is a well-defined boundary separating the region where two energy minimum exist from that where only one exists. Thus, only one magnetization direction is possible when H is outside the asteroid, while two possible magnetization directions exist when H is inside the asteroid.

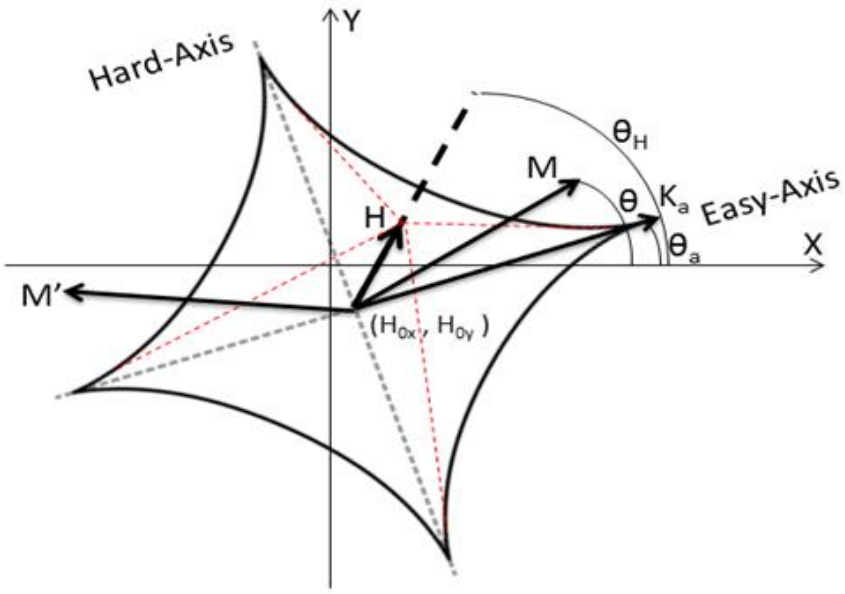

Fig. 9.5 Schematic of an asteroid curve and the free layer magnetization M orientation in the presence of an applied magnetic field H. According to the S-W model, the equilibrium orientations of the magnetization have to meet two requirements: (1) they must be parallel to the lines (red dashes) that are tangent to the asteroid and pass through the tip of the H arrow; (2) they must make the smallest angles possible with respect to the easy-axis direction. As shown in the figure, the magnetization directions are geometrically determined, and are labeled M and M'.

The free layer magnetization direction can also be obtained by geometrically finding the direction(s) parallel to the tangential lines passing through the tip of the external magnetic field H that make(s) the smallest angles with the easy axis (labeled as M and M', respectively, in Fig. 9.5). When H is outside the asteroid, only one line makes the smallest angle with respect to the easy axis; when H is inside the asteroid, two lines possess smaller angles, corresponding to the two equilibrium states.

Therefore, taking the linear transfer curve means that the field H is uniaxially increasing or decreasing, making two interceptions with the asteroid curve. The distance

between these two interceptions, by definition, is twice the value of the coercivity. When the magnetic field is large in both directions, the magnetization direction tends to align with the magnetic field in one or the other direction, giving rise to anti-parallel and parallel states. Taking the RRC means that the free layer magnetization is close to the initial applied magnetic field direction and then aligns with the anisotropy direction which takes the smallest angle after the magnetic field is removed. Hence, two energy states and two resistance values are obtained after applying the field in all 360 degrees. Consider a circle transfer curve with large magnetic field that has no interceptions with the asteroid curve. The free layer magnetization rotates in 360 degrees and generates a sine-like resistance curve. However, if the magnetic field is small enough and no interceptions with the asteroid curve occur, the free layer magnetization cannot complete an entire 360-degree rotation, but will rotate harmonically within a certain range [22]. In this case, a sine-like resistance curve is also obtained. Things are quite different in the transition range between these two situations, as the magnetic field magnitude happens to intercept the asteroid curve. This phenomenon can be observed by measuring circle transfer curves while subsequently increasing magnetic field amplitude, as we will discuss later.

Typically, there are two methods to record an asteroid curve: “fixed bias field” and “fixed-angle”. In the former method, transfer curves are taken repeatedly under different fixed orthogonal bias fields. Therefore, for each bias field value, there are two points on the transfer curve that have the largest derivative, ($\frac{dR}{dH}$). These points correspond to the two switching fields. Plotting these values for all fixed bias fields yields the

asteroid curve as in Fig. 9.6. In the latter method, transfer curves are taken from 0 to 180 degrees. Finding the switching fields and plotting them also gives the asteroid curve.

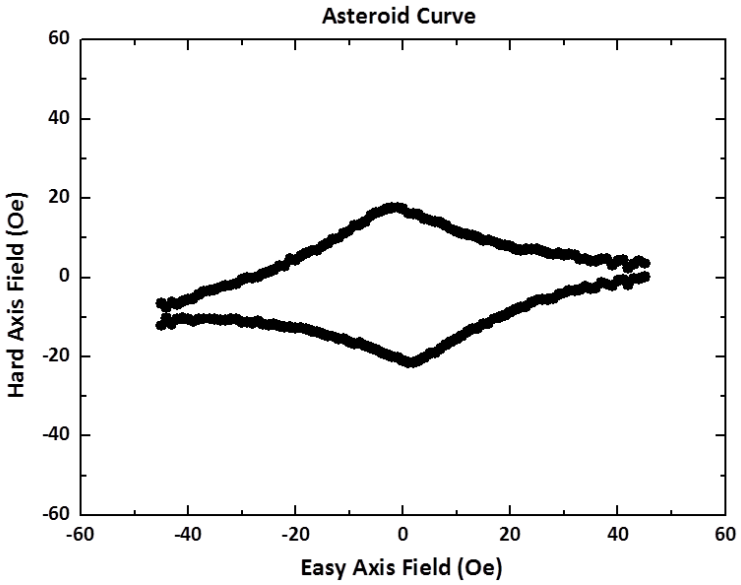

Fig. 9.6 Experimentally-measured asteroid curve of a sample MTJ by "fixed-bias" method.

Several magnetic parameters are extracted from the asteroid curve shown in Fig.9.6, including the following: the offset of the asteroid center, $(H_{0x}, H_{0y}) = (0.08, -4.04)Oe$; the free layer anisotropy strength, $K_a = L_x = 42\ Oe$, where L_x is half the length of the asteroid axis perpendicular to the easy axis direction; and the anisotropy direction $\theta_a = 6.2°$ with respect to X axis. All these parameters are required for further circular transfer curve analysis and pinning direction calculations, as well as theoretical simulation.

3D Magnetoresistive Transfer Curve Contour

Different external magnetic field magnitudes yield different circular transfer curve behaviors, due to the interceptions between the asteroid curve and the different-scale circles formed by the rotating magnetic field. The field dependence of the CTC

fundamentally differs from a “switch” to a “sensor”. Without an external magnetic field, for a “switch” configuration the free layer magnetization and pinning direction can be either anti-parallel or parallel. This is not the case for the “sensor” configuration, in which the free layer magnetization is orthogonal to the pinning direction. Each of these cases was analyzed independently.

Case (1): “Switch” Configuration (pinning direction parallel to anisotropy direction)

To better understand the magnetic field magnitude dependence of the circular transfer curves, we plot the 3D magnetoresistive transfer curve contour (Fig. 9.7 and Fig. 9.8) with two different initial states: anti-parallel (AP) or parallel (P). Starting from the AP state, a dip in the anti-parallel resistance occurs at approximately 15 Oe when sweeping the rotating magnetic field magnitude from 1 Oe to 80 Oe (Fig. 9.7). This dip suggests that the energy gaps between the magnetization of a domain switching from the AP state to the P state and from the P state to the AP state are different, with the former energy gap being smaller than the latter one. These gaps imply that the critical magnetic field required to switch the domain from the AP state to the P state is smaller than that needed to flip the magnetization back from the P state to the AP state. Due to the large scale of our sample, about 50×100 μm^2, a multi-domain structure is formed in the presence of an external magnetic field. When the switch is initially in the AP state and the rotating magnetic field amplitude increases, the system first encounters the lower critical field region. The field is sufficiently large to switch some of the domains from the AP state to the P state, but not large enough to switch them back resulting in the observed drop in the R_{ap} resistances on each circular transfer curve. Afterwards, when the magnetic field increases to the higher critical field region and is able to switch the domain back

from the P to the AP state, the R_{ap} rapidly increases to its possible maximum value, and then remains almost constant while the magnetic field keeps increasing.

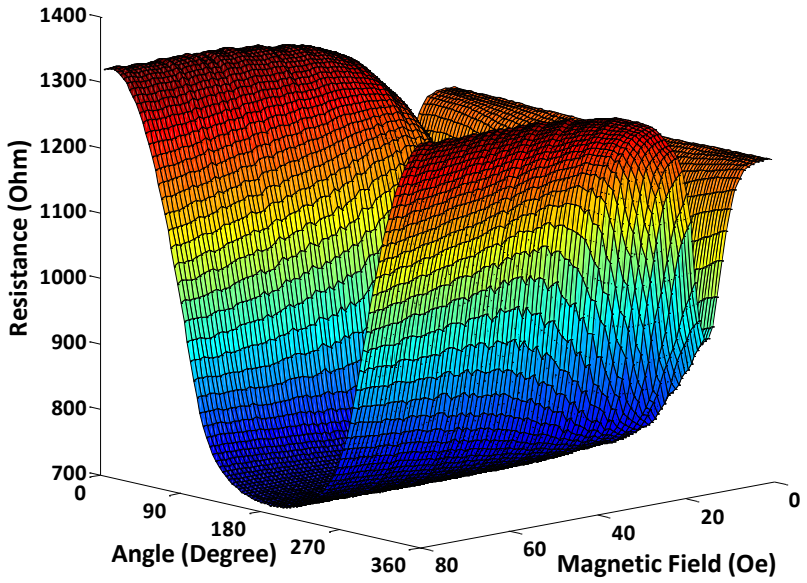

Fig. 9.7 3D magnetoresistive circular transfer curve contour of a sample in the "switch" configuration, with initial AP state

However, when the system is initially in the P state, no such R_{ap} resistance dip is observed (Fig. 9.8). While below 15 Oe, when the magnetic field comes to the lower critical field that can switch the domain from the AP to the P state, nothing happens as most of the domains are in the P state. After, when the magnetic field reaches the higher critical field value, which is able to switch domains from P state to AP state, more and more domains respond while the magnetic field keeps increasing. When the field is larger than 15 Oe, the curve behavior is the same, regardless of the initial states of the system.

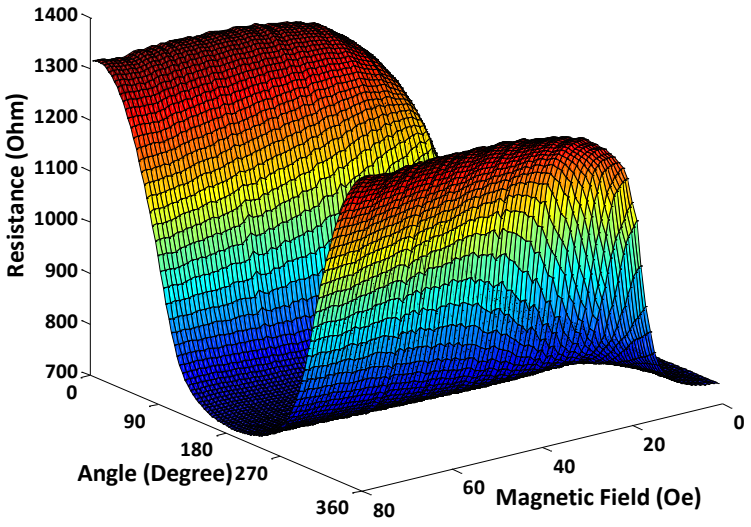

Fig. 9.8 3D magnetoresistive circular transfer curve contour of a sample in the "switch" configuration, with initial P state

By comparing the R_{ap} behaviors of the two different initial conditions (Fig. 9.9 (a), (d)), the only difference is observed below the critical field of 15 Oe. Different from AP state-initial system, there is a small peak around 15 Oe in the R_p curve in P state-initial system (Fig. 9.9 (b) (e)). Before the magnetic field reaches the critical field, R_p increases slightly due to a small number of domains switching from the P to the AP state. The subsequent decrease in R_p suggests an increasing number of domains that switch from the AP to the P state. In both situations, as shown in Fig. 9.9 (c) (f), the MR similarly changes from almost 0% up to over 80%. Overall, the different behaviors between different initial states only happen at low magnetic field. When the magnetic field is larger than 45 Oe, no significant change in these characteristics suggests that the free layer is saturated. This field is close to the measured saturation field in the asteroid curve method.

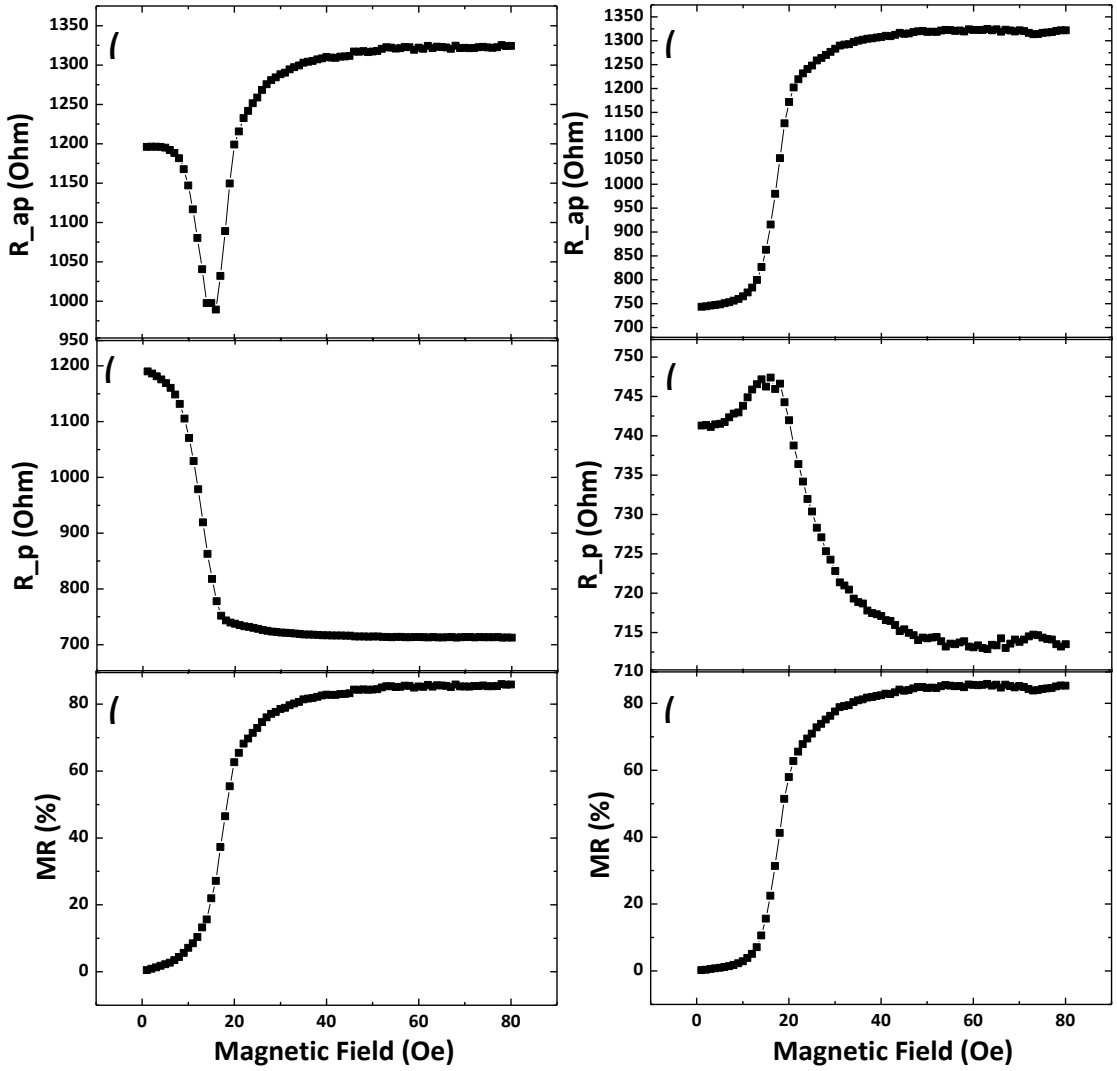

Fig. 9.9 (a)-(c) are the maximum resistance (R_{ap}), the minimum resistance (R_p), and the MR of each magneto magnetoresistive circular transfer curve dependent on the magnetic field with an initial AP state. (d)-(f) are the maximum resistance (R_{ap}), the minimum resistance (R_p), and the MR of each magnetoresistive circular transfer curve, dependent on the magnetic field with an initial P state.

Case (2): "Sensor" Configuration (pinning direction orthogonal to anisotropy direction)

The 3D magnetoresistive transfer curve contour of a "sensor" configuration is shown in Fig. 9.10. As rotating field magnitude increases, R_{ap} (R_p) increases (decreases) continuously at low fields (<20 Oe), leading to a significant increase in the MR ratio.

When greater than 50 Oe, the magnetic field saturates the sensor leading to no changes in these three characteristics (Fig. 9.11). In the region from 10 to 20 Oe (Fig. 9.11 (c)), the MR ratio change is almost linear, suggesting a potential method of precisely identifying the external rotating magnetic field magnitude.

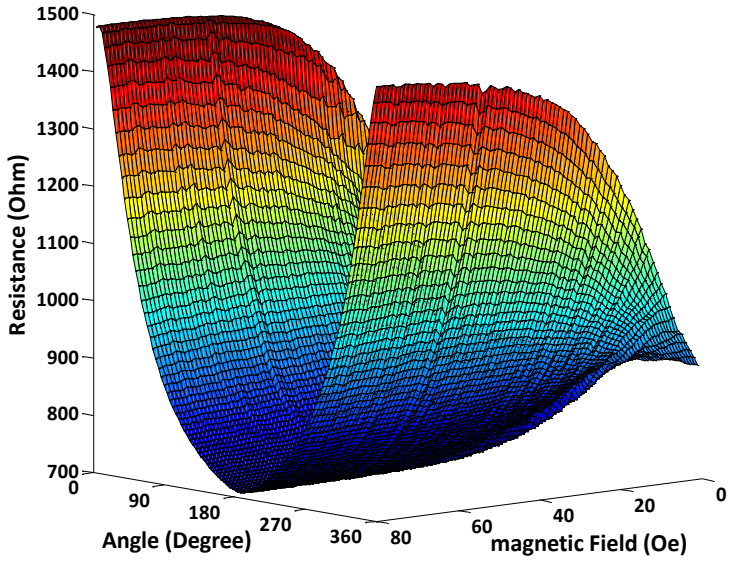

Fig. 9.10 3D magnetoresistive circular transfer curve contour of a sample in the "sensor" configuration, dependent on field amplitude

Despite the observed differences between the circular transfer curve behaviors of the "switch" and the "sensor" configurations under mid-range magnetic fields, they have the same trends at the extremes. At low field, both circular transfer curves appear to be perfect sinusoids because the free layer magnetization only swings within a small range around the easy axis. At large field, both curves approach a sinusoidal pattern, since the magnetization is almost aligned with the external magnetic field and rotates 360 degrees with it. The ranges of "very low" and "very large" can be defined by considering the

regions where the rotating magnetic field circle has no interceptions with the sample asteroid curve.

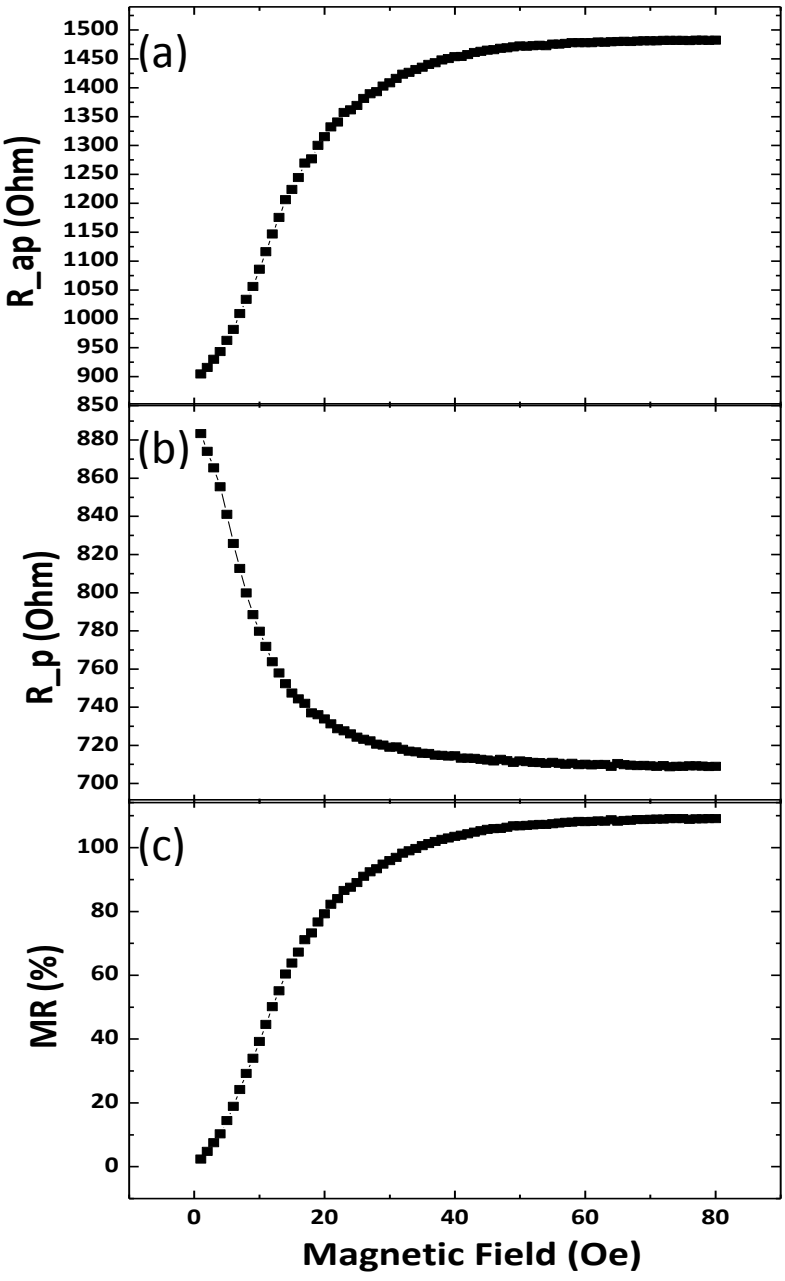

Fig 9.11 (a)-(c) are the maximum resistance (R_{ap}), the minimum resistance (R_p), and the MR of each magnetoresistive circular transfer curve dependent on the magnetic field (sensor).

9.2.2 Theoretical Simulations

A theoretical simulation of the circular transfer curve based on the S-W model is shown in Fig. 9.12 (in red). This result is obtained by minimizing the free energy equation (9.2) and calculating the conductance using the equation

$$g(\theta) = g_0[1 + P^2 \cos(\theta - \theta_P)], \tag{9.3}$$

where P is the spin polarization of tunneling electrons. Parameter P is calculated by measuring the MR ratio from the circular transfer curve and by using the equation

$$MR = \frac{2P^2}{1-P^2}. \tag{9.4}$$

g_0 is a constant extracted from the experimental circular curve by waveform curve fitting as we assume the resistance behaves sinusoidally at large magnetic fields (100 Oe). The pining direction θ_P, affected by the external magnetic field H, is subject to the equation

$$\theta_P = tan^{-1}\left(\frac{H_E sin\theta_E + H sin\theta_H}{H_E cos\theta_E + H cos\theta_H}\right), \tag{9.5}$$

where H_E is the pinning strength and θ_E is its original orientation. The parameters used in the simulation are as follows: $K_a = 42\ Oe, \theta_a = 6.2°, H_{0x} = 0.08\ Oe, H_{0y} = -4.04\ Oe,$ $\theta_E = 3°, H_E = 2500\ Oe, P = 0.597, g_0 = 0.001038\ S.$

When modeling the pinned layer magnetic properties, we need to include the influence of the external magnetic field on the pinned layer, which may rotate slightly due to the external magnetic field. Thus, the circular transfer curves at different rotating magnetic field magnitudes also differ due to the slight rotation of the pinning direction of the pinned layer. Although the variance is small, it has been detected from the phase shift on measured circular transfer curves, and has helped to determine both the pinning

strength and direction in Safron and Ben's earlier work [13]. In our case, the circular transfer curves taken from a "sensor" configuration at 40 Oe and 80 Oe have a 1 degree detectable phase shift.

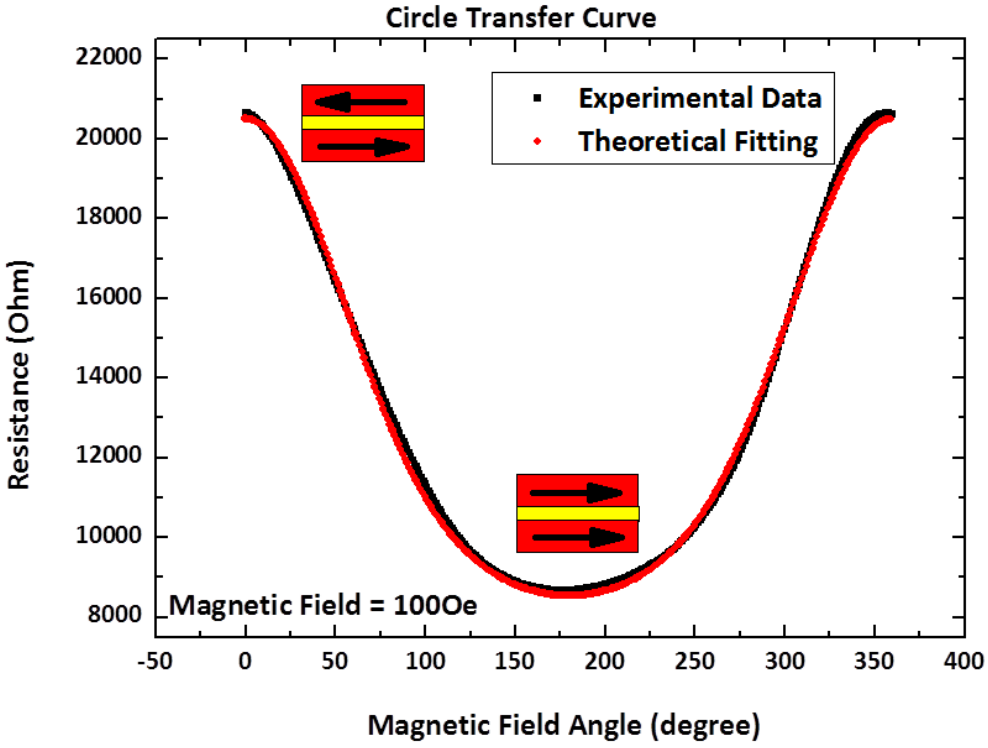

Fig. 9.12 Theoretical simulation (in red) based on parameters extracted from an experimental circular transfer curve measurement.

The theoretical simulation of the field magnitude dependence of the circular transfer curve illustrates similar behaviors (Fig. 9.13) when compared with experimental 3D circular curve contours. Although the pinning strength is 2500 Oe (compared to the external magnetic field of only 80 Oe), a detectable phase shift of the circular curves is observed, which is consistent with experiments. The theoretical simulations exhibit pure sinusoidal behavior at the extremes of the field (below 7 Oe and above 50 Oe). The

presence of this phenomenon in both the experimental and theoretical results suggests it is physically consistent and deserving of further study.

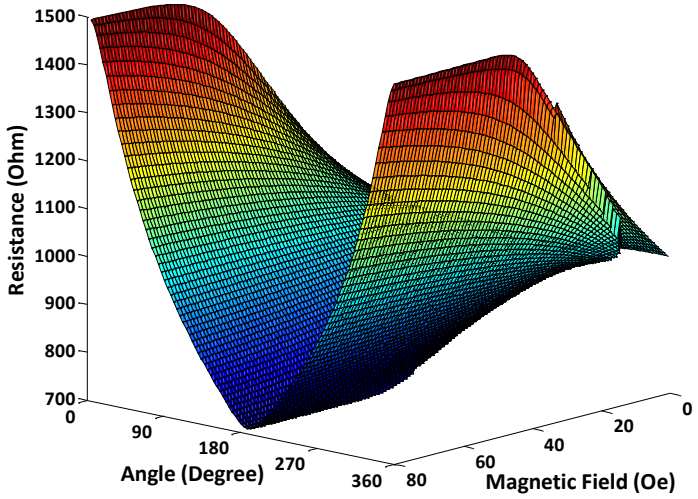

Fig. 9.13 3D simulated magnetoresistive circular transfer curve contour of a sample in the "sensor" configuration, dependent on field amplitude on the basis of the parameters extracted from the experiment.

9.3 Conclusion

In this chapter, a suite of different magnetoresistive transfer curve measurement techniques have been developed in order to meet different measurement requirements and to obtain a more exhaustive set of magnetic device parameters than that obtainable from conventional methods. These parameters include magnetoresistance, sensitivity, coercivityH_C, internal offset fields $H_{0x}$and H_{0y}, free layer anisotropy strength K_a, free layer anisotropy direction θ_a, pinning strength H_E and pinning direction θ_E.

Of all the methods developed, the magnetoresistive circular transfer curve technique is the most comprehensive means of determining the free layer anisotropy strength and direction and pinning direction and strength of the pinned layer based on prior knowledge of H_{0x} and H_{0y}, which can be extracted from standard asteroid measurements. Importantly, the circular transfer curve provides information about the pinned layer, which cannot be extracted from the asteroid curve measurement. Moreover, the field-magnitude-dependence of the circular transfer curves provides far more detailed information, such as the approximate exchange bias orientations and magnitudes, than linear transfer curves. These capabilities were particularly useful in revealing the different behaviors between the "switch" and the "sensor" configurations at the extreme of small magnetic fields. Used in conjunction with the circular transfer curve measurements, the remnant resistance curve provides a powerful method of obtaining free layer anisotropy information. The combination of these magnetoresistive transfer curve measurements provides a complete magnetic property characterization of a magnetic device.

Along with the experimental measurements, theoretical simulations based on the S-W model were conducted. Parameters extracted from the experimental data allowed the minimization of the least-chi square fit and successive improvements to the parametric curves. Through the minimization of the free layer energy equations (accounting for the slight effect of the external magnetic field on the pinned layer), the physical mechanism underlying the device behaviors exhibited at different magnetic fields in the circular transfer curves was revealed. This suite of measurements presents myriad possibilities for practical applications. Beyond calculating the basic magnetic parameters, the

magnetoresistive transfer curves can also demonstrate the two-dimensional sensitivity as well as the anisotropy orientation dispersion of a device consisting of junction arrays. As a result, this technique can serve as a detailed guide for further improvements to both single and multiple MTJ devices, ultimately leading to superior performance.

References

1. R. Coehoorn, J. C. S. Kools, T. G. S. M. Rijks, and K. M. H. Lenssen, Philips J. Res. 51, 93 (1998)
2. C. H. Tsang, R. E. Fontana, T. Lin, D. E. Heim, B. A. Gurney, and M. L. Williams, IBM Journal of Research and Development. 42, 103 (1998)
3. S. A. Wolf, D. D. Awschalom, R. A. Buhrman, J. M. Daughton, S. von Molnár, M. L. Roukes, A. Y. Chtchelkanova, D. M. Treger, Science, 294, 5546 (2001)
4. J. A. Katine, F. J. Albert, R. A. Buhrman, E. B. Myers, and D. C. Ralph, Phys. Rev. Lett., 84, 3149 (2000)
5. F. J. Albert, J. A. Katine, R. A. Buhrman, and D. C. Ralph, Appl. Phys. Lett., 77, 3809 (2000)
6. J. S. Moodera, L. R. Kinder, T. M. Wong, and R. Meservey, Phys. Rev. Lett. 74, 3273, (1995)
7. T. Miyazaki and N. Tezuka, Journal of Magnetism and Magnetic Materials, 139, L231 (1995)

8. E. Y. Tsymbal, O. N. Mryasov and P. R. LeClair, J. Phys. Con. Matt. 15, R109 (2003)

9. W. H. Butler, X.-G. Zhang, T. C. Schulthess, and J. M. MacLaren, Phys. Rev. B, 63, 054416 (2001)

10. S. Yuasa, T. Nagahama, A. Fukushima, Y. Suzuki, K. Ando, Nature Materials, 3, 868 (2004)

11. S. Yuasa, A. Fukushima, T. Nagahama, K. Ando and Y. Suzuki, Jpn. J. Appl. Phys. Part 2, 43, L588 (2004)

12. W. Zhang, Q. Hao, and G. Xiao, Phys. Rev. B 84, 094446 (2011)

13. N. S. Safron, B. D. Schrag, X. Liu, W. Shen, D. Mazumdar, M. J. Carter, and G. Xiao, J. Appl. Phys. 103, 033507 (2008)

14. J. Fujikata, T. Ishi, S. Mori, K. Matsuda, K. Mori, H. Yokota, K. Hayashi, M. Nakada, A. Kamijo, and K. Ohashi, J. Appl. Phys. 89, 7558 (2001)

15. C.-L. Lee, A. Devasahayam, M. Mao, J. Kools, P. Cox, K. Masaryk, D. Mahenthiran, and J. Munson , J. Appl. Phys. 93, 8406 (2003)

16. P.Wisniowski, T. Stobiecki, J. Kanak, G. Reiss, H. Brückl, Journal of Applied Physics, 100, 013906 (2006)

17. S. S. P. Parkin, C. Kaiser, A. Panchula, P. M. Rice, B. Hughes, M. Samant, and S. H. Yang, Nat. Mater. 3, 862 (2004)

18. W. F. Egelhoff, Jr., V. E. Höink, J. W. Lau, W. F. Shen, B. D. Schrag, and G. Xiao, J. Appl. Phys. 107, 09C705 (2010)

19. S. Shtrikman and D. Treves, J. Appl. Phys. 31, S58 (1960)

20. E. C. Stoner and E. P. Wohlfarth, IEEE Trans. Magn., 27, 3475 (1991)

Chapter 10

Summary

In search of the ideal candidates for spintronic applications such as non-volatile magnetic random access memory (MRAM) and high-performance magnetic sensor, this thesis work includes the study of Giant Spin Hall Effect (GSHE), Anomalous Hall Effect (AHE) and Magnetic Tunnel Junctions (MTJs). By studying the magnetic and transport properties in solids with GSHE, AHE and MgO-based MTJs, we are able to explore the characteristics of these devices at a fundamental level. We hope this work will help us better understand underlying physics, explore for potential applications of spintronic devices with performance such as non-volatile, low-power consumption, high-reliability, low noise and ultrafast response.

Taking advantage of the thin film solids with large spin-orbit coupling, we have successfully fabricated GSHE devices with perpendicular magnetic anisotropy (PMA). We achieved this by carefully controlling the material thicknesses as well as the post annealing conditions. The multilayer GSHE solids/CoFeB/MgO structure with PMA enables us to switch the magnetization vector through an applied charge current in the presence of a small magnetic field. The Spin Hall Angle in β-W is -0.4 (in the bulk limit) at room temperature, which is the largest among transition metals. The lowest critical current density to induce the magnetization switching is about $1.6*10^6 A/cm^2$ under 2 mT constant magnetic field in the W/$Co_{40}Fe_{40}B_{20}$/MgO structure. Also, we researched the formation of β-Ta and β-W using magnetron sputtering technique. It turns out that the

extremely low sputtering rate (<0.02nm/s) is critical to for this highly-resistive metastable state. Using the beta-Ta/CoFeB/MgO structure with PMA, we developed a methodology to calculate spin Hall angle of beta-Ta and conducted more experiments on this multilayer structure to understand annealing effects and temperature dependence. We found the existence of an optimal annealing condition (temperate range 220±20 °C) in order to achieve PMA in our structure. Temperature dependence study revealed the correlation between beta-Ta resistivity and spin Hall angle, which is useful for revealing the underlying mechanism of the GSHE. Also, we developed a systematic method to achieve beta phase W in a wide range from 3 nm to 26.7 nm which is confirmed by both resistivity and XRD measurement. It also shows a post annealing process under 280 ºC for 1 minute will transform the beta-W to alpha-W when the film is thicker than a critical thickness~ 22 nm. Previous study has revealed that the spin diffusion length of beta-W is 3.5 nm which is much lower than this critical thickness. Therefore, in the attempt of integrating beta-W into spintronic devices where post annealing process is required, the W thickness has to be within the range defined by these two values.

The Anomalous Hall Effect (AHE) sensor is further studied based on the Fe-Pt alloy. We developed a common rotation method in order to achieve high quality Fe-Pt alloy with variable composition. We studied Extraordinary Hall Effect in Fe-Pt alloy: its properties in various temperatures and noise performances in different thicknesses and Fe concentrations combinations. The Quantum Design Physical Property Measurement System (PPMS) enables us to conduct transport and magnetic measurements in the temperature range from 2 K to 300 K in ±2 Tesla. This temperature dependence study reveals the correlation between longitudinal resistivity and Hall resistivity, which is

helpful to understand the underlying mechanism that leads to the AHE in Fe-Pt system, which we found out to be the combination of Berry-phase mechanism and side-jump mechanism. We also found the hall slope is maximized when Fe concentration is 29%, which is consistent with previous study. The very large Hall slope (16.6 $\mu\Omega \cdot cm/T$ at room temperature) indicates its great potential in magnetic sensing applications.

The noise performance of the Fe/Pt alloy-based AHE sensor is equally important to the Hall slope. We demonstrated that our Fe/Pt alloy sensor is much better than some semiconductor Hall sensor because of metallic nature of the Fe-Pt in terms of low-frequency noise performance. In spite of relative low sensitivity, the minimum detectable field of our thin-film hall sensor can be as low as 1uT at 1Hz and 0.07 uT at 1k Hz. It even outperforms the semiconductor Hall sensor by one order of magnitude in a certain frequency range (3Hz to 1500Hz).

Finally, we studied the Magnetic Tunnel Junction in fast magneto-transport measurements. First of all, we develop the transfer curves and circle transfer curves methods to efficiently extract all essential parameters of the MTJs. Compared to the traditional transport measurements, we are able to characterize the junctions fast and automatically through Labview programs and NI-DAQ techniques. Besides, the Circle Transfer Curve measurement enables us to accurately find TMR and Easy Axis of the MTJ junction within one signal run. Most importantly, we improved the capability of characterizing the MTJ through asteroid curve on the basis of Stoner-Wohlfarth theory and extract the curve within only a couple of seconds, which used to take at least 10 hours by the old technique. Meanwhile, a 3D magneto-transfer curve measurement is invented, and the fast measurement also takes only a couple of seconds. We believe these

transport measurement study is useful for characterizing the properties of MTJ systems and guiding for the design or applications of MTJ-based devices. Especially, the integration of MTJ (with PMA) and GSHE structure has the great potential for future applications in spintronic devices.